Monte Carlo Simulation, Analytical Investigation and Dosimetric Verification of Intraoperative Electron Beams

A Dissertation

to Acquire the Doctoral Degree Submitted to the Mathematics-Natural Sciences Faculty of Heinrich-Heine University of Dusseldorf

by

Majid Ghorbanpour Besheli

from Savadkoh

Dusseldorf, 01/2016

From Department of Radiotherapy and Radiation Oncology of Heinrich-Heine University of Dusseldorf

Printed with the permission of Mathematics and Natural Sciences Faculty of Heinrich-Heine University of Dusseldorf

Referee: Univ.-Prof. Dr. med. Wilfried Budach
Second examiner: Prof. Dr. Thomas Heinzel

Date of Examination: 12.04.2016

To my love, Carolin, who unselfishly put up with my endeavor

Abstract

During the last few years more and more clinics worldwide have been drawing attention to mobile intra-operative electron linear accelerators as an advanced therapeutic option against cancer. The specific design of such Intraoperative Radiation Therapy (IORT) accelerators, particularly the polymethylmethacrylat (PMMA) electron applicators along with their dose-per-pulse range, can considerably influence the characteristics of the electron beam compared to conventional electron beams. Therefore, in the first part of this thesis, the ion recombination correction factor (k_s) is determined at medium dose-per-pulse values. Different methods are evaluated, three of which are known as Boag's modified expressions. In the fourth method, the IAEA TRS-398 protocol is applied. In conclusion, in the medium dose-per-pulse range all Boag's modified expressions could be used for k_s determination. Above a dose-per-pulse value of 35 mGy/pulse, the TRS-398 approach should be avoided.

In the second part of this investigation a Monte Carlo based model of a mobile IORT linear accelerator is achieved using EGSnrc system. The electron beam simulations were verified by comparing the calculated dose distributions with the corresponding measured data. In addition, the unknown parameters of electrons energy spectra were determined by fitting to measurements. The differences between calculated and experimental percentage depth dose and profiles were lower than 2%. The simulated accelerator model could be applied to CT images or other phantoms in order to study dose distributions located near PTV (Planning Target Volume) during IORT applications e.g. determination of patient skin dose during an IORT treatment or calculation of backscattered dose. Furthermore, output factors were calculated and compared with measured data obtained by means of an ionization chamber in water. Moreover, the Spencer-Attix stopping power ratios were calculated and compared with data determined from TRS-398 dosimetry protocol. The results of above mentioned simulations were verified by a close agreement achieved between calculated and measured values of output factors mostly within $\pm 2\%$.

As a further aim of this study, an investigation regarding characteristics of electrons produced by NOVAC7 IORT accelerator is presented. Important findings regarding the dosimetric characteristics of electrons were observed depending on the applied field size. It is expected that the results achieved in this study help for accurate patient dose calculation in an IORT treatment planning system and also for chamber simulation particularly the determination of chambers perturbation correction factors.

Zusammenfassung

Während der letzten Jahre hat die Anzahl der Kliniken, welche mobile intraoperative Elektronenlinearbeschleuniger als eine fortschrittliche Behandlungsoption gegen Krebs einführen, weltweit deutlich zugenommen. Das spezielle Design derartiger Linearbeschleuniger für die intraoperative Strahlentherapie (IORT), insbesondere die eingesetzten Elektronen-Applikatoren aus Polymethylmethacrylat (PMMA) und dem verwendeten Dosis-pro-Puls Leistung haben einen wesentlichen Einfluss auf die Merkmale dieser dedizierten Beschleuniger im Vergleich zu den konventionellen Therapiegeräten. Aus diesem Grund wird im ersten Teil der vorliegenden Dissertation der Ionenrekombinationsfaktor (k_s) für mittlere Dosis-pro-Puls Bereiche analysiert. Hierbei wurden verschiedene Methoden bewertet. Hierzu zählten drei Möglichkeiten, welche in der Literatur als Boag´sche modifizierte Ansätze bekannt sind. Der vierten Methodik liegt das IAEA TRS-398 Protokoll zugrunde. Zusammenfassend kann festgehalten werden, dass alle drei Boag´schen Ansätze für die k_s Bestimmung herangezogen werden können. Bei Werten der Dosis-pro-Puls von über 35 mGy/Puls sollte der TRS-398 Ansatz allerdings nicht angewandt werden.

Den zweiten Teil der Arbeit nimmt die Untersuchung des Monte Carlo Modells des mobilen IORT Elektronenlinearbeschleunigers unter Verwendung des EGSnrc Simulationscodes. Die simulierten Elektronenstrahlen wurden verifiziert durch den Vergleich der berechneten Dosisverteilung mit den entsprechenden Messdaten. Darüber hinaus wurden die unbekannten Parameter des Energiespektrums durch das Fitten der Messkurven ermittelt. Der Unterschied zwischen gemessenen und simulierten Tiefendosiskurven und Querprofilen lag bei unter 2%. Das Simulationsmodell des Beschleunigers kann zusammen mit CT-Datensätzen oder Phantommaterialien angewandt werden um die Dosisverteilung im Bereich des Planungszielvolumens (PTV) zu bestimmen und somit beispielweise die Hautdosis oder die Rückstreudosis während der IORT Behandlung zu ermitteln. Weiterhin wurden die Outputfaktoren berechnet und mit Messungen in Wasser mittels einer Ionisationskammer verglichen. Außerdem wurde das gesamte Bremsvermögen nach Spencer-Attix berechnet und mit den Messdaten anhand des IAEA TRS-398 Dosimetrie-Protokolls verglichen. Berechnete und gemessene Werte der Outputfaktoren haben gut übereingestimmt ($\leq$2%).

Ein weiteres Ziel dieser Arbeit ist die Bestimmung von Elektronenstrahlmerkmalen des dedizierten Linearbeschleunigers. In diesem Zusammenhang konnten wichtige Erkenntnisse bezüglich der dosimetrischen Eigenschaften von Elektronenstrahlen in Abhängigkeit von der applizierten-Feldgröße ermittelt werden. Es ist davon auszugehen, dass diese Ergebnisse sowohl in die genaue Berechnung der Dosis von klinischen IORT Bestrahlungsplanungssystemen als auch in die Simulation und Entwicklung von neuartigen Ionisationskammern zur Bestimmung der Korrektionen von Störungsfaktoren einfließen werden.

Contents

1. Introduction

1.1. Ion recombination correction factor

External beam radiation therapy (EBRT) refers to the projection of radiation from outside the body. This therapy option is carried out with external beam sources such as a linear accelerator (linac). In this method the radiation oncologist must mainly determine the appropriate radiation dose, the correct number of fractions of radiation per day, the correct dose per fraction, and the proposed total dose of irradiation. The goal of radiotherapy is to eradicate a tumor using ionizing radiation whereas the dose to the surrounding healthy tissue is maintained as low as reasonably achievable (ALARA) [1]. In intraoperative radiation therapy (IORT) a high single dose is applied to the tumor bed directly after resection of the malignancy. This therapy option allows achieving a selective radiation boost on the tumor volume. A boost administers higher radiation doses to the entire clinically apparent tumor cells or tumor residual [1]. In some cases, IORT can also be used as a single-fraction/stand-alone treatment in initial cancers of small volume, or in unresectable malignancies for palliative purposes [2, 3]. IORT treatments can be realized using dedicated electron linear accelerators that produce high dose-per-pulse electron beams, which in particular significantly shorten the treatment time compared to other methods [4].

Producing high dose-per-pulse beams however introduces new challenges of measuring the absorbed dose using ionization chambers. This is mainly because the effect of the ion recombination correction factor k_s will be more profound. This factor corrects the response of the ionization chamber for the ion loss due to the recombination of ions inside the chamber (see subsections 2.7.6 and 2.7.7) [5]. Based on current dosimetric protocols the k_s factor is mostly determined by Two Voltage Analysis (TVA) method or the Jaffé diagram [6, 7, 8, 9].

Recent publications have shown that at high dose-per-pulse values these methods do not predict the k_s factor accurately [10, 11]. Piermattei et al. have reported that these protocols are

not suitable for dosimetry of high dose-per-pulse electron beams [10]. They observed that the k_s values resulting from these protocols deviate up to 20% from the values obtained by means of dose-rate-independent dosimeters. Discrepancies are caused by an effect known as free-electron fraction p, which is ignored in the current protocols but is significant for k_s determination in high dose-per-pulse beams.

Free electrons are electrons generated by a radiation pulse that do not attach to oxygen molecules and reach the collecting electrode of the chamber [12]. Therefore, due to the collection of free electrons a reduction in recombination and an increase in chamber efficiency occurs. This effect is neglected in current dosimetry protocols. Consequently the k_s factor will be overestimated. In order to solve this problem, three improved theoretical models for the charge collection process incorporating the free-electron component have been introduced by Boag et al., called Boag's modified expressions [13]. Di Martino et al. have used one of these models and proposed a method to determine the p value for specific ionization chambers (i.e. Markus and PTW-Roos) [14]. In their method k_s values were determined using a dose-per-pulse-independent dosimeter. Another experimental approach, which used Boag's three expressions, was proposed by Laitano et al. [11]. Here k_s values were determined for different ion chambers without using any dose-per-pulse-independent dosimeter. In their method the value of p was calculated as a function of chamber characteristics and experimental conditions. These two approaches were compared by Cella et al. for the Markus chamber and the Advanced Markus chamber [15]. They concluded that, for the Markus ion chamber, the first model of Boag's modified expressions could predict the k_s value more accurately than other models for dose rates above 30 mGy/pulse.

However, although the effect of free electrons on the k_s factor was demonstrated more than ten years ago, not much attention has been paid to determine whether the standard methods (IAEA TRS-398 and Jaffé diagram) deliver acceptable results using an Advanced Markus ionization chamber. Moreover, the determination of the ion recombination correction factor for dose rates varying from 4 mGy/pulse to about 42 mGy/pulse has not been extensively examined yet.

The intention of this article is to determine this k_s factor using different approaches and compare them with a dose-per-pulse-independent dosimeter [16].

1.2. Monte Carlo simulation and commissioning of an IORT linac

Intraoperative Electron Radiation Therapy (IOERT) refers to the delivery of single high dose of radiation directly to the tumour bed or residual tumour soon after surgery excision [2]. This technique is effective because it allows direct visualization of the region to be irradiated after the removal of the lesion and it allows surrounding healthy tissues to be adequately protected [3]. The application of dedicated accelerators generating only electron beams of a maximum energy of 9-12 MeV solves logistic and clinical problems, such as the need for transporting the anesthetized patient outside the operating theatre or the necessity of special fixed shielding barriers, thereby shortening the overall time of the procedure.

Based on the effort of the department of radiation therapy at the university hospital of Dusseldorf (UKD), a dedicated mobile IOERT accelerator, the NOVAC7 (SIT, Aprillia/Italy), has been installed in the clinic of gynaecology and is currently used clinically. This system is equipped with special collimation systems consisting of long PMMA cylindrical applicators which are considerably different from those currently used for IOERT [17]. Moreover, in contrary to conventional medical linear accelerators, the NOVAC7 does not use scattering foils or bending magnets to shape the electron beams. The IOERT beams will therefore have different characteristics compared to beams obtained from standard accelerators. Such a possible difference could make the results obtained by Björk et al. that performed their investigation on a conventional linac, not directly applicable to the electron beams of the NOVAC7 [18].

It is difficult to experimentally obtain detailed information because of various limitations in the clinical environment and detectors. Moreover, the considerable number of combinations of applicators and electron energies requires an extensive and comprehensive amount of dosimetric measurement which should be carried out by the operator. The Monte Carlo method is a powerful tool for the simulation of realistic clinical radiation beams and obtaining detailed knowledge of the characteristics of therapy beams from linear accelerators [19].

In this study, the Monte Carlo code EGSnrc was employed for simulating the head and the beams produced by the NOVAC7 [20]. This model makes it possible to evaluate and calculate all dosimetric relevant necessities such as energy fluence distributions, stopping power ratios, scattered electrons contributions, photon contamination and electrons angular distributions with high accuracy.

1.3. Stopping power ratios and output factors

As mentioned in previous section (see 1.2), on the one hand, the clinical IOERT beams have specific characteristics compared to beams produced by conventional accelerators. Particularly, energy spectra, fluence and angular distributions of electrons are different. These parameters, on the other hand, affect output factors and mass collision stopping-power ratios which are necessary for absorbed dose determination.

The methodology to determine the stopping power ratios recommended in current dosimetry protocols DIN6800-2 [9], IAEA TRS-398 [7] and AAPM TG 51 [6, 8] is based on the measured and Monte Carlo calculated data published by Ding et al. which used the realistic electron beams produced by conventional medical accelerators [19]. Using these protocols for the degraded beams including those obtained with IOERT could introduce uncertainties in the absorbed dose determination due to the difference in the energy spectrum which causes difference in the stopping power ratio and output factor values.

Björk et al. have calculated output factors and stopping power ratios using different detectors for some IOERT beams produced by a conventional linac [21]. They have reported that ignoring the effect of scattered electrons could lead to 1.3% underestimation of output factor at 6 MeV IOERT beams. Pimpinella et al. have recently carried out a Monte Carlo study of the NOVAC7 to investigate some of the dosimetric characteristics of this linac [22]. They recommended that an understanding of stopping power ratios of IOERT beams is necessary to decide whether the current dosimetry protocols could be applied. Even though some Monte Carlo calculations have been carried out in degraded electron beams, an extensive study of output factors and stopping power ratios regarding the NOVAC7 accelerator is necessary for absorbed dose determination and deciding whether the current dosimetry protocols could be used for this specific system.

The aim of this study was to calculate the $s_{w,air}$ (Spencer–Attix stopping power ratios of water-to-air) and output factors for electron beams produced by the NOVAC7 and to compare them with the values reported in the IAEA TRS-398 dosimetry protocol [7]. A subsequent purpose of the current investigation was the evaluation of the Monte Carlo model described in previous chapter using the output factor results.

1.4. Scatter and contamination analysis

The dosimetric characteristics of electrons have to be known in order to estimate the absorbed dose in the patient accurately. Additionally, understanding of such dosimetric features can help us to comprehend and explain the complexity of measuring absorbed dose in water, ion recombination correction factor determination and chamber perturbation correction factors as described later in section 2.7. Moreover, using the results of these investigations, the deviations of stopping power ratios and output factors from the values resulted for conventional linacs could be better understood.

Cylindrical shape of the collimation system of the NOVAC7 causes different electron components to be created underneath the applicator. According to that, as described by Pimpinella et al., Miheilescu et al. and Björk et al., if N_{tot} is the total number of particles that cross the phantom surface, it could be stated that:

$$N_{tot} = N_{dir} + N_{sct}, \tag{1.1}$$

where N_{dir} is the number of direct electrons which are defined as the electrons that interact only in the monitor chambers and the air in the cylindrical applicator (see the NOVAC7 schematic in section 3.1) [22, 23]. N_{sct} is the total number of electrons scattered from different components of the head of the NOVAC7 accelerator; for example accelerator head, adaptor, applicator, etc. The bremsstrahlung photons are also included in this group of particles. Using clinical detectors, it is complicated to achieve detailed information about the NOVAC7 IOERT machine and distinguish the above mentioned electrons reaching the dosimeter sensitive volume. Some efforts have been done regarding this issue in recent years. On one hand, Björk at al. have investigated the electrons characteristics of IOERT fields produced by conventional accelerators [24]. On the other hand, Pimpinella et al. and Miheilescu et al. have also studied some aspects of the NOVAC7.

However, it is important to note that the electrons characteristics of every accelerator differ in each model and should be investigated individually. In addition, to the author's knowledge, it is not known how the contribution of direct and scattered electrons influences the energy spectrum, fluence or mean energy distribution at large and small IOERT fields. Such information is necessary for dose calculation, absorbed dose determination and understanding of isodose

distribution in an IOERT treatment planning system. Following eq. 1.1, the absorbed dose to water at a specific depth is the sum of the contributions from different components and could be written as:

$$D_{tot} = D_{dir} + D_{sct}, \tag{1.2}$$

where the subscripts have the same meaning as in equation (1.1) . There are limited data about the contribution of the direct and scattered electrons on the depth dose and off-axis profile distributions, especially for small applicators which are mostly used in clinical applications. It is hardly known, how the depth dose and off-axis distributions of direct and scattered electrons vary when moving from water surface to the larger depths in water phantom.

The main objective of the present work was to study the contribution of direct and scattered electrons to energy fluence, fluence, mean energy and angular distributions of electrons. Furthermore, a subsequent purpose of this study was to analyze depth dose and off-axis dose distributions resulted from direct and scattered components at different depths for variety of energies and applicators. Such investigation has never been conducted extensively yet. Moreover, the intention of this study is to evaluate the present limited results published by Pimpinella et al. and Miheilescu et al. regarding the NOVAC7 in order to expand this area of research.

The Monte Carlo model of the NOVAC7 presented in chapters 3 and 4 will be utilized for calculation of its electron characteristics. According to that, BEAMDP, BEAMnrc and DOSXYZnrc user codes were used to obtain the specific parameters mentioned above [25, 26, 27]. In this chapter, for simplification, 3 and 5 MeV electrons are referred to as ″low energies″ and the 7 and 9 MeV electrons are summarized as ″high energies″. Furthermore, the 100 mm applicator is named ″reference″ and 40 and 50 mm applicators are denoted as ″clinical fields″.

1.5. Thesis overview

The purpose of this thesis is to investigate the electron beams generated by the NOVAC7. It is hoped that the results would improve the accuracy of absorbed dose determination and comprehension of the electron characteristics like energy fluence, depth dose and angular distributions of scattered electrons. The stopping power ratios and output factors are also investigated. For this purpose, a Monte Carlo model has been developed using the measured data as benchmark which includes depth dose and off-axis profiles. In addition, characteristics of electrons are also examined with focus on the electron energy fluence distribution, fluence, mean energy, angular distribution, etc. The focus on such parameters is due to the fact that they are important for developing a treatment planning system and understanding of the scatter behaviour. Chapter 2 will focus on introducing concepts and effects allowing the comprehensive interpretation and understanding of the results presented in later chapters. Chapter 3 introduces the materials and methods regarding the measurement of the ion recombination correction factor and Monte Carlo simulation system.

Chapter 4 will cover the results of the present thesis including (a) an investigation carried out to determine ion recombination correction factor using different methods currently applied in literature, (b) the development of a Monte Carlo model to simulate the electron beams of the NOVAC7, (c) the determination of the stopping power ratios and output factors required for absorbed dose determination and (d) the calculation of dosimetric parameters including energy fluence distribution, mean energy, depth dose and profiles of different electron components. Chapter 5 outlines the discussion regarding particular parts of results mentioned previously. Chapter 6 will summarize and draw conclusions from the entire work and give future directions.

2. Theory

2.1. Intraoperative Radiation Therapy (IORT)

As previously implied, IORT refers to the delivery of a single high dose of radiation to the tumor bed or residual tumor directly after surgery excision. This application began with low-energy x-ray beams in 1907, when Comas et al. and later on Carl Beck treated patients with gastric and colon cancer [28, 29]. The low penetrating capability, however, caused damage to underlying healthy tissues passed through by the radiation. This led to disregarding of this technique until photons were replaced by electron beams in 1965 in Japan.

Intraoperative electron radiotherapy (IOERT) was conducted using megavoltage electrons produced by a Betatron installed in an operation theater within the department of radiotherapy [30]. In 1981, Abe and Takahashi published the combined Japanese results in 727 patients and demonstrated successful results [31, 32]. On the one hand, a dedicated accelerator in an operating room was not an economical alternative for any hospital, taking into account the costs of the machine and radiation protection issues. On the other hand, in several hospitals the intraoperative radiotherapy technique was also carried out using electron beams of a linear accelerator (linac) generally used for external beam radiotherapy. This means, transporting the patients, in the course of the surgical intervention, to the shielded radiotherapy facility and re-transporting them to the operating theatre after the irradiation [3]. In spite of the problems existed due to logistic issues as well as radiation shielding requirements, the results obtained with electrons reported by Abe and Takahashi attracted worldwide interest to IORT and led to the development of dedicated mobile accelerators to be integrated in operating theatres.

Currently there are two manufactures producing dedicated mobile IOERT accelerators. Intraop Medical Incorporated of Santa Clara, California which manufactures the Mobetron and Sordina IORT Technologies; SIT, Vicenza, Italy, which manufactures the NOVAC and the LIAC machines [2, 33]. IOERT technique is effective since it allows direct visualization of the region

to be irradiated after the removal of the tumor while allowing surrounding healthy tissues to be adequately protected.

2.2. Interaction of electrons in matter

Electrons lose their energy in matter through continuous energy loss, in contrast with photons which undergo few interactions. In contrary to heavy particles, electrons can lose a large fraction of their energy due to their small mass. As a result they may be sharply deflected and/or scattered with large angles. Generally, electrons interact with the Coulomb field of nuclei and orbital electrons in matter. Coulomb interactions could be either elastic or inelastic. If electrons undergo elastic event, they would only change the direction, without having any influence on the energy. Through inelastic collision (energy transfer) two separate events are possible. They are referred to as "collisional interactions" (soft and hard interactions) and "radiative interactions" (bremsstrahlung photons). The type of interaction of electron in matter depends on the impact parameter, b, and the atomic radius, a. As demonstrated in figure 2.1, the inelastic interactions are categorized into three parts, soft collisions, hard collisions and radiative collisions [34].

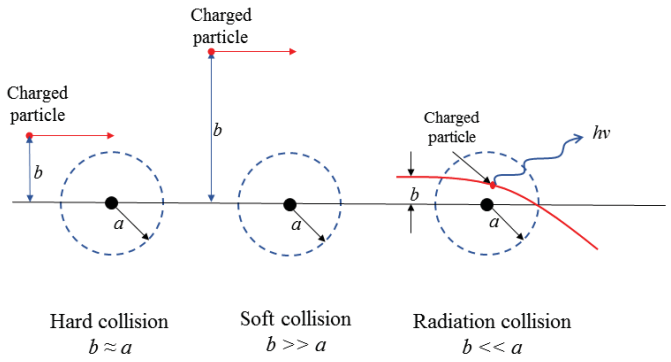

Figure 2.1.: The three possibilities of electron collisions with atomic material which depend on the relative size of the impact parameter, b, as well as the atomic radius, a. Hard collisions happen when $b \approx a$, soft collisions occur when $b >> a$ and radiative collisions take place when $b << a$. Reproduced from [34].

2.2.1. Soft collisions

In this collision, b is much larger than a ($b >> a$) and the electron interacts with the Coulomb field of the atom. The atom can be excited to a higher energy level or lose an orbital electron through ionization. Through this interaction, a small amount of energy will be transferred to the atom which goes back to its ground state by releasing characteristic x-rays or Auger-electrons. This is the most probable interaction which electron undergoes and through this approximately

50% of its energy is transferred to the medium.

2.2.2. Hard collisions

In this case b is equivalent to a ($b \approx a$), and electron interacts most likely with an orbital electron of the atom, hence a so-called delta (δ) or knock-on electron will be ejected. The released electron has sufficient energy to undergo interactions similar to those of the initial electron. In the course of hard collision analogous to soft collision, the exited atom returns to its ground state and thereby emits x-ray and/or Auger electrons. The energy loss of electrons in this case is similar to soft interaction, although this interaction occurs with lower probability compared to soft collision.

2.2.3. Radiative interactions

This type of interaction takes place when b is much less than a ($b << a$) and the electrons are mainly subjected to an inelastic Coulomb interaction with the Coulomb field of the nucleus. Due to sharp deflection and acceleration of electron caused by the coulomb filed of the nucleus, bremsstrahlung photons are emitted. The probability of this interaction is predominantly proportional to Z^2 (atomic number) and electron energy. A limited amount of electrons ($2-3\%$) undergo this collision. As previously mentioned, elastic scattering occurs due to interaction of electrons with the Coulomb field of the nucleus. This phenomenon plays an important role (98%) when electrons interacting with the nucleus of the atom and is proportional to Z^2. This explains why electrons produce a totally twisted and curved track [34, 35].

2.2.4. Mass stopping power and range

As mentioned above, electrons deposit their energy continuously in matter due to inelastic (collisional and radiative) interactions. The mass stopping power $s/\rho(\text{MeV cm}^2/\text{g})$ is defined as the amount of energy delivered to the surrounding medium per density thickness and is given as:

$$\frac{s}{\rho} = \frac{1}{\rho}\frac{dE}{dx}. \tag{2.1}$$

The total mass stopping power $(s/\rho)_{tot}$ consists of the contribution of collisional stopping power, s_{coll}, and radiative stopping power, s_{rad}, and it is given as:

$$(s/\rho)_{tot} = (s/\rho)_{coll} + (s/\rho)_{rad}\,. \tag{2.2}$$

It is worth mentioning that due to the soft interactions, the electron energy is transferred to the surrounding medium along the ionization track; whereas in other cases this energy is carried away by δ-rays and bremsstrahlung photons without having a significant contribution to the local dose. The mass stopping power of electrons associated with the elastic and inelastic collision is specified by an improvement to the Bethe-Bloch expression [36], as follows:

$$\left(\frac{s}{\rho}\right)_{coll} = \frac{2\pi r_e^2 m_0 c^2}{\beta^2}\left(\frac{N_A Z}{A}\right)\left[ln\frac{\tau^2\,(\tau+2)}{2\,(I\,m_0 c^{-2})} + F^{\pm}\,(\tau) - \delta - 2\frac{C}{Z}\right] \tag{2.3}$$

with

$$F^{\pm}\,(\tau) = 1 - \beta^2 + \frac{\tau^2}{(8 - (\,2\tau - l\,)\,ln2)\,(\tau+1)^2}, \tag{2.4}$$

where r_e represents electron radius, m_0 is the electron mass, $\beta = v/c$ is the proportion of the velocity of electron v to the light velocity $c, \tau = T_0/(m_0c^2)$ represent the relationship between the electron kinetic energy and its energy of rest mass, N_AZ/A is the quantity of electrons per mass of matter and I the mean energy of atom excitation. The expression was also modified for two factors that turn out to be remarkable at very high and intermediate to low energies. One is the shielding of distant electrons because of the polarization of orbital electrons by the electric field of the moving electron. This is called density effect and is denoted by the term δ in eq. (2.3). The second correction is mainly applied at lower energies and is a function of electron orbital velocity. This is commonly referred to as ″shell correction″ and it is demonstrated by the term C/Z in eq. (2.3). The stopping power changes gradually depending on the particle energy and is related directly to the atomic number Z of the material. Also, it can be observed that the collision stopping power decreases with increasing the electron energy $(1/v^2)$. Furtheremore, the radiative stopping power for electron energies up to 100 MeV was suggested by Heitler [37].

This is given by:

$$s_{rad} = \left(\frac{dE}{dx}\right)_{rad} \propto \rho \left(\frac{e}{m_e}\right)^2 Z^2 E_{tot}, \tag{2.5}$$

which demonstrates that radiative stopping power is directly related to the electron's total energy E_{tot}, the density ρ and the atomic number Z. More detailed discussion about this topic can be found in [34]. In order to estimate the range of electron in the medium, a so-called continuous slowing down approximation (CSDA) was proposed [34]. This technique is based on the fact that the majority of the collision and radiative events deliver only a small amount of the incident energy to the medium and accordingly, electrons lose their energy slowly and continuously. Additionally, electrons with equal energies do not have equal ranges due to differences in the amount of their energy loss. It means that the range of electrons fluctuates around a mean value. This effect is known as range straggling. The mean value of electron range can be determined by the CSDA approximation, in which the inverse of total stopping power ratio is integrated over the electron energy as:

$$R_{CSDA} = \int \left(\frac{s_{tot}}{\rho}\right)^{-1} dE. \tag{2.6}$$

In general, the electron range obtained by CSDA method is an appropriate assessment. Further details are given in section 2.5.

2.2.5. Restricted stopping power

In several radiation dosimetry applications, it is crucial to estimate the amount of energy delivered to a specific region. Using the previous formula (eq.(2.3)) in order to determine the absorbed energy may induce overestimation because δ electrons may not necessarily transfer their energy to the very close vicinity of the location where they are created. Therefore, the term restricted collision stopping power (L_Δ) has been defined. In this concept, only the linear rate of energy loss less than a threshold value of Δ is considered and is given as:

$$L_\Delta = \left(\frac{dE}{dx}\right)_\Delta. \tag{2.7}$$

This parameter has the same dimension as stopping power and is commonly reported in units of keV/μm. The employment of the restricted stopping power is significantly important in dosimetry of ionization chambers, where the main challenge is to determine the energy absorbed locally within the air-filled chamber volume (see section 2.6 concerning the cavity theory). Moreover this concept is helpful in Monte Carlo simulations in order to calculate the absorbed dose in small volumes.

2.3. Interaction of photons in matter

A photon undergoes multiple types of interactions in matter. However, since the absorbed dose due to photons are not significant in this study, only a short description of the most relevant interaction types is provided. Compton scattering, photoelectric effect and pair production are the most applicable interactions regarding the energy range used in this study. These interactions can be divided into two categories, interactions of photons with the nuclei of the atoms and interactions of photons with the orbital electrons of the atoms. Pair production is associated with the nuclei of the atom. Photons that interact with orbital electrons have two alternatives; either to interact with electrons that are bounded loosely to the atom or with electrons that are bounded tightly. The atomic binding energy of a loosly bounded electron is the same as or less than the incident photon, whereas the binding energy of a tightly bounded electron is significantly larger than the energy of incident photon [38]. The Compton effect is due to interaction with loosely bounded electrons, while the photoelectric effect is caused by the interaction with tightly bounded electrons. Compton effect, photoelectric absorption and pair production transfer the photon energy to electrons which consequently deliver their energy to the medium. One of these interactions will occur based on the material composition and the incident photon's energy.

2.3.1. Photoelectric Effect

Photoelectric effect corresponds to the interaction of a photon with a tightly bound orbital electron (i.e. with an atom as a whole). As a result, the incident photon is absorbed entirly and the electron is set in motion, as can be seen from fig.2.2. The kinetic energy of the electron is the subtraction between the energy of incident photon and the binding energy of the electron. The mass attenuation coefficient in this interaction is proportional to $(Z/h\nu)^3$, where Z is the atomic

number of the attenuator and $h\nu$ is the photon energy. Photons can only undergo photoelectric interaction if $h\nu$ is equal or greater than the binding energy of electrons in that particular shell. In water, this interaction is dominant at photon energies less than 20 keV [39].

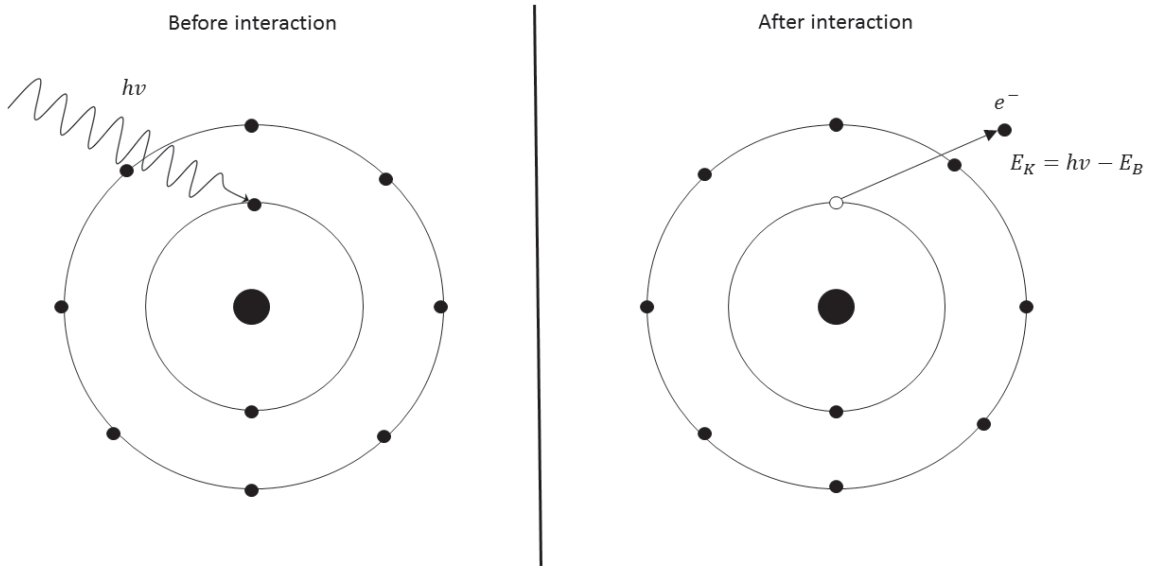

Figure 2.2.: Schematic illustration of the photoelectric effect where a photon with energy $h\nu$ interacts with a K-shell electron. The photon is absorbed completely and the K-shell electron or so-called photoelectron is ejected from the atom with a kinetic energy $E_K = h\nu - E_B(K)$, where $E_B(K)$ is the binding energy of the K-shell electron. Reproduced from [35].

2.3.2. Compton Scattering (incoherent scattering)

According to fig. 2.3, the Compton effect is known as the interaction of a photon with an orbital electron which has a low binding energy (i.e. free orbital electron). As a result, the so-called Compton electron (or recoil electron) is released and the incident photon is scattered. The kinetic energy of the rejected electron is then the subtraction of the photon energy and the binding energy of the electron. The scattered photon energy $h\nu^{'}$, the Compton electron kinetic energy E_K and the relation between the scattering angle of photon θ and Compton electron angle ϕ are calculated from equations corresponding to conservation of energy and momentum in the Compton process and can be written as:

$$h\nu^{'} = h\nu \frac{1}{1 + \epsilon\,(1 - cos\,\theta)}, \tag{2.8}$$

$$E_K = h\nu \frac{\epsilon\,(1 - \cos\theta)}{1 + \epsilon\,(1 - \cos\theta)} \tag{2.9}$$

and

$$\cot\phi = (1 + \epsilon)\tan\theta/2, \tag{2.10}$$

respectively, where $h\nu$ is the energy of incident photon and ϵ is the normalized incident photon energy $\left(\epsilon = \frac{h\nu}{m_e c^2}\right)$. In this interaction the mass Compton attenuation coefficient is independent of Z. On average, a 1 MeV photon undergoing Compton scattering will produce a 440 keV recoil electron and a 560 keV scattered photon. A 10 MeV photon will generate a 6.9 MeV recoil electron and a 3.1 MeV scattered photon [39]. The range of angle ϕ varies from 0 for $\theta = \pi$ (photon backscattering) to $\pi/2$ for $\theta = 0$ (forward scattering of photon) independent of photon energy. For a given θ, the Compton electron angle ϕ decreases when the energy of incident photon increases. The significat energy region for this interaction in water is 20 keV-10 MeV [39].

2.3.3. Pair Production

Pair production corresponds to an interaction of a photon with the Coulomb force field of a nucleus which leads to complete absorption of incident photon and emission of a positron-electron pair. For the effect to occure, energy, charge and momentum must be conserved (see fig. 2.4). The minimum energy (threshold energy) of the photon to undertake pair production interactions is the sum of the rest energy (0.511 MeV) of electron and positron and equals to 1.02 MeV. The probability for pair production increases at photon energies larger than the threshold energy. The mass attenuation coefficient for pair production is proportional to Z. In water, this interaction is important at photon energies above 10 MeV [39].

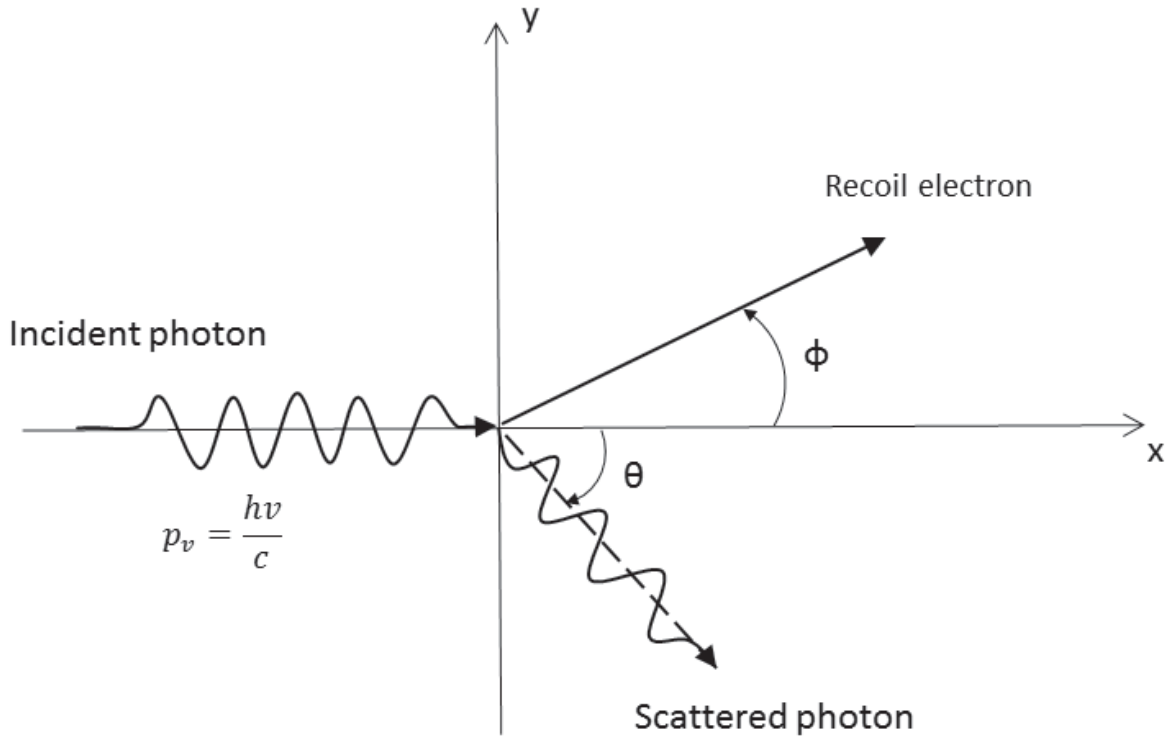

Figure 2.3.: Schematic illustration of the Compton effect where the incident photon with energy $h\nu$ interacts with a motionless and free electron. A photon with energy $h\nu'$ is generated and scattered. The difference between the energy of the incident photon $h\nu$ and that of the scattered one $h\nu'$ is transferred to the recoil electron. Reproduced from [35].

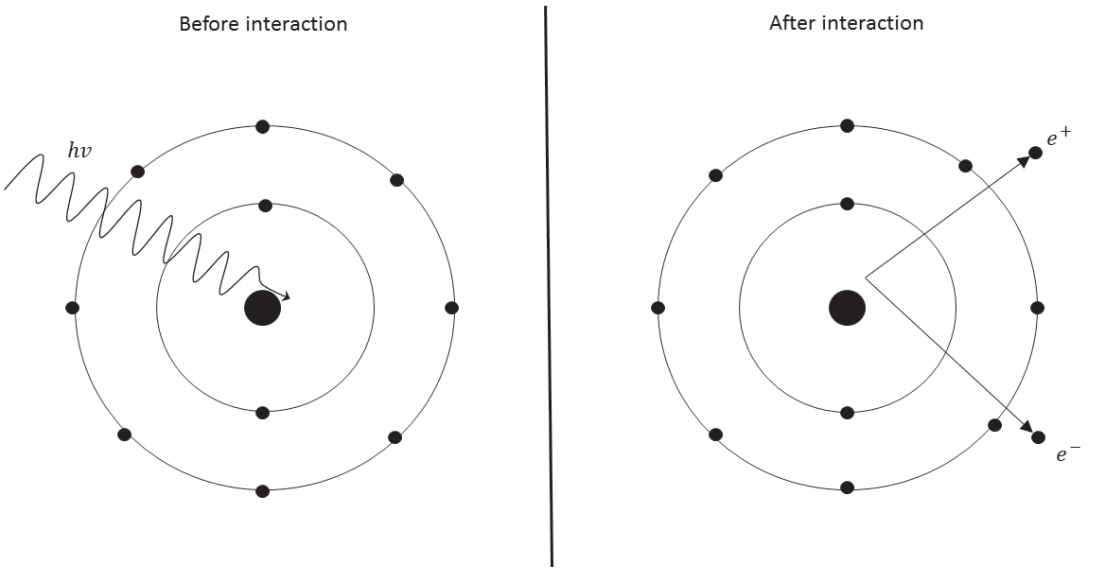

Figure 2.4.: Schematic diagram of pair production where an incident photon with energy $E_\nu = h\nu > 2m_e c^2$ and momentum $p_\nu = h\nu/c$ interacts with the Coulomb field of a nucleus and an electron-positron pair is produced. Reproduced from [35].

2.4. Monte Carlo simulations in Medical Physics

2.4.1. Introduction

Monte Carlo (MC) is a numerical method to solve statistical problems implementing random number generators (RNGs). The MC method is one of the most precise techniques available to simulate radiation transport in materials. Regarding radiation transport modeling, the MC technique is a stochastic approach which simulates individual particles (e.g. photons and electrons) applying random numbers distributed according to cumulative probability function. The transport of a primary particle and all belonging secondary particles is referred to as "particle history". Mean values of objective functions (energy fluenc, angular distribution, absorbed dose, etc) are obtained based on the simulation of N histories with a corresponding statistical uncertainty given by standard deviation (σ). In fact, the σ value of a simulation depends on the number of particle histories N and decreases as $N^{-1/2}$, which means that σ is halved if N (and the simulation time) is increased by a factor of 4 [40].

2.4.2. History of Monte Carlo simulation

Stochastic sampling approaches were known considerably earlier than computers to solve statistical problems [41]. The first study using stochastic sampling techniques applied to radiation transport simulations was conducted by von Neumann and Richtmyer in 1947 [40, 42, 43]. The first unclassified publication on the Monte Carlo related to stochastic sampling was reported in 1949 by Metropolis and Ulam [44]. Particularly, the technique was applied to investigate neutron scattering and absorption. Following that, a lot of research projects have been carried out investigating the application of the methods not only in particle physics but also in economics, computer science, statistical mechanics and medical physics [45]. Therefore, the number of publications regarding the use of the MC method for radiation transport analysis along with the developing of different code systems increased substantially [46]. One of the outstanding contributions to the field of MC electron and photon transport was the publication of Berger; He introduced the condensed history technique of electron transport which will be discussed later in this chapter (see section 2.5) [47]. Berger's collaboration with Steve Seltzer resulted in the development of the ETRAN $e-\gamma$ code [48] which has become the fundamental algorithm of the electron transport in many general purpose codes such as the MCNP [49] and EGS4 systems [50].

Meanwhile, other scientists attempted to develop EGS code systems analyzing electron-photon transport preliminary for high-energy physics shielding and detector simulation [51]. The pioneer scientist was Ralph Nelson who developed the EGS3, followed by the EGS4, EGS4/PRESTA in correspondence with Rogers. These efforts led to the development of EGSnrc code systems [50, 52, 53, 54, 55]. Recently, an MC code produced for particle physics application, known as GEANT4, has been developed. It can model the transport of different particles (protons, neutrons, etc.) and has been applied for variety of applications in medical physics [56]. The PENELOPE Monte Carlo system deals with cross sections expansively for low-energy transport and has a powerful geometry package, allowing clinical beam modeling [57]. The MC simulation of Cobalt-60 beams was first described in the ICRU Report number 18 [58]. The simulation of linac beams was first performed by Petti et al. [59]. In addition, simulating of electron beams from medical linacs was first achieved by Teng et al. [60]. The original idea to use Monte Carlo method to calculate patient dose was suggested by Mackie et al. [61]. It was later on known as OMEGA (Ottawa Madison Electron Gamma Algorithm) project in which the linac output files or so-called phase-space-files were exploited as inputs in order to calculate the dose distribution in patients. Using the MC method for treatment planning has been dramatically developing and can be followed in literature [62].

2.4.3. Comparison between Monte Carlo simulation and numerical quadrature

As described in detail by Seco and Verhaegen, the MC method is the most efficient way of assessing results in multiple dimensions when compared to deterministic (analytic) methods [40]. Deterministic (analytical) methods are limited with approximation in treatment of heterogeneities and boundaries. Furthermore, apart from systematic errors related to dealing with heterogeneities, deterministic methods use approximations in treating multiple-scattering of particles. Another problem is to solve the dimensionality of the equation. The overall convergence rate for deterministic methods is $N^{-2/D}$. The more dimensions (D) considered in the problem, the slower the convergence for these methods. The MC method differs from analytical and numerical (deterministic) approaches mainly due to using a random number generator and probability distribution functions to model parameter values in order to solve a problem related to a history [63]. The MC technique is associated with a standard deviation which reduces while increasing the number of simulated histories. This type of uncertainty does not exist when analytical methods are applied.

2.4.4. Random number sampling

MC methods implement a computational algorithm called Random Number Generator (RNG) in order to produce a long sequence of numbers that appeared to be random. In fact, the sequence of numbers produced by such algorithms is determined by a shorter primary absolute value, called seed value. In other words, if the seed value is known, the entire apparently random sequence can be regenerated. This kind of random numbers are called pseudorandom numbers. A large sequence of these pseudorandom numbers is required in order to find a solution for a complicated problem. A RNG applicable in medical physics must fulfil two criteria. Firstly, the sequence length shall be long enough in order to avoid correlation among results and secondly, the uniformity of distribution should be guaranteed to assure that the results are equally probable [64].

2.4.5. Numerical integration

Coupled (electron-photon) Boltzmann radiation transport expressions are considered to solve problems in radiation therapy. Such equations should be analysed by multidimensional numerical integrations because analytical methods have difficulities dealing with higher dimensional space. Fundamentally, numerical integration in the MC technique is done by sampling N random points, x_i, in multidimensional volume, V, with D dimensions ($D \times N$ random numbers) and the MC numerical integration, I, is given by

$$\int dV\, V \approx V\langle I\rangle \pm \sqrt{\frac{\langle I^2\rangle - \langle I\rangle^2}{N}} \tag{2.11}$$

with

$$\langle I\rangle \equiv \frac{1}{N}\Sigma_{i=1}^{N} I_{x_i} \tag{2.12}$$

and

$$\langle I^2\rangle \equiv \frac{1}{N}\Sigma_{i=1}^{N} I_{x_i}^2. \tag{2.13}$$

Each of these N points represents a particle history which includes secondary particles produced by an initial particle. From the above equations it can be seen that as the number of

simulations, N, tends to infinity, Monte Carlo integral $\left(\int I\,dV\right)$ converges to a real integral (V) and that the rate of convergence is related to the square root of the quantity of samples $\left(\frac{1}{\sqrt{N}}\right)$. In other words, if the number of simulated histories (N, random points) is increased by a factor of four, the statistical uncertainty is halved. This is a unique feature of MC technique compared to numerical and analytical methods [65].

2.4.6. Photon transport

The interaction of photon with material is already described in section 2.3 and is mainly dominated by the photoelectric absorption (pho), Compton scattering (C) and pair production (p). In MC method, random number sampling and probability weight functions are crucial to demonstrate the coupled electron-photon transport mechanism. Particle type, its energy and scattering angle along with characteristics of secondary particles are chosen making use of these two features. Due to relative long mean free path of photons passing through the human tissue, not many photons should be simulated. Therefore, every photon trajectory will be precisely modeled, considering different mass density of materials. This kind of particle trajectory modelling is referred to as "analog transport". In the primary step, the distance l to the first interaction point is obtained for each photon being simulated, using the probability function as given by:

$$p \approx exp\left(\frac{-1}{\lambda}\right), \tag{2.14}$$

where λ is the mean free path length to the first interaction and is characterized by

$$\lambda = \frac{A}{N_A \rho \sigma_{tot}}, \tag{2.15}$$

where A is the atomic mass number, N_A, ρ and σ_{tot} are the Avogadro's number, mass density and the total cross section which is associated with different microscopic interaction probabilities ($\sigma_i = \sigma_{ph} + \sigma_R + \sigma_C + \sigma_p$). According to the cumulative distribution function of equation (2.11), the l value can be obtained by

$$l = -\lambda \times ln\left(\varepsilon\right), \tag{2.16}$$

where ϵ is a sampled random number limited to interval [0 , 1]. Afterwards, the photon is transported to the first interaction location (distance l) and according to the total cross section (σ_{tot}), at this point, for an specific material, an interaction type is chosen. Particularly, the second random number ($\epsilon 2$) is sampled according to the each interaction cross section $\left(\frac{\sigma_i}{\sigma_{tot}}\right)$as part of the total cross section (σ_{tot}) which is given by

$$\sigma_{tot} = \sum \sigma_i = \sigma_{ph} + \sigma_R + \sigma_C + \sigma_p. \tag{2.17}$$

The interaction type (photoelectric, Compton or pair production) is then selected and the particle is simulated. If a secondary particle is produced, it is put on the pile to be simulated later, independent from the initial particle. Even electrons could be simulated in this alnalog manner. The entire particle history is simulated including all secondary particles and its daughter particles. This whole process is repeated until the photon or electron leave the geometry of interest or their energy becomes lower than a predefined value. These cut-off energies are usually referred to as "E_{cut}" for charged particles and "P_{cut}" for photons. [34, 40, 66, 67].

2.4.7. Electron transport

As previously mentioned, due to the large mean free path lengths of photons with energy range typically used in radiation therapy, very few interactions of photons are required to be simulated. This makes the simulation of photons easier and with considerably less computational complication it is possible to simulate each history interaction by interaction in different materials. With regards to charged particles like electrons, this process is entirely different. Electrons undertake much larger number of interactions before falling below a specific energy level or absorption compared to photons. For example, electrons with energies more than 1 MeV require only a transport distance between 10^{-5} and 10^{-4} g/cm^2 to the next interaction. Furthermore, a 6 MeV electron beam undergoes between 3×10^4 and 3×10^5 interactions before absorption. As an inevitable consequence, simulation of electrons based on interaction by interaction scenario similar to photons leads to a substantially large computation time. As an alternative solution for electron transport, a so-called Condensed History (CH) technique was suggested by Berger in 1963 which is described in details in section 2.5 [40, 47, 65].

2.5. Condensed history

Due to the fact that nearly all of electron collisions are elastic or semielastic, charged particles energy and direction do not change significantly. Therefore, it is possible to consider all these interactions in a single CH step. The CH approach involves dividing all interactions of one charged particle history into hard and soft type of collisions as well as hard and soft type of bremsstrahlung production interactions. These two interaction types (hard and soft) are distinguished by a predefined kinetic energy loss threshold of E_c and k_c for collisional and radiative (bremsstrahlung) interactions, respectively. Collision or bremsstrahlung interaction, in which energy less than E_c or k_c is transferred to the secondary particle, is defined as soft interaction, otherweise it will be considerd as hard interaction.

In particular, the most important soft collisions are Coulomb elastic scattering, atomic excitation, Møller scattering (delta electrons) and bremsstrahlung photons with an energy below k_c. These soft collisions are condenced and simulated in one step, whereas hard collisions are modelled explicitly similar to photons. Using multiple scattering methods, small changes in the direction of the particle during soft collitions will be considered in a large multiple scattering angle. It is important to note that all secondary electrons undergoing hard collision have a minimum energy of E_c (k_c when photons), whereas this energy is the maximum energy transferd to electrons (and their maximum range) undertaking soft interactions. To keep the CH technique accurate, a maximum value for the step size (s_{max}) is defined automatically by the algorithm according to the stopping power and the mass density of the current material. Hence, the CH step is terminated when either the s_{max} is achievd or a hard collision is ocurred. Figure 2.5 demonstartes different possible interactions for an electron history [47, 67]. Electrons move generally on stright lines during the CH step. As a consequence of multiple scattering, they alter the direction either at the end of the step (see fig. 2.6) or (as illustrated in figs. 2.5 and 2.7) between step ends.

In the second case (as presented in fig. 2.7), a so-called random hinge method can be employed to determine the multiple scattering. As it is shown in figure 2.5, a hard Møller scattering can constrain the CH step size and results in secondary charged particles, referred to as "delta electrons". It should be noted that, δ electrons are modelled by CH approach until they leave the simulation geometry or their energy becomes less than E_{cut}. Analog-transport method is applied to simulate all secondary bremsstrahlung photons (see section 2.4.6).

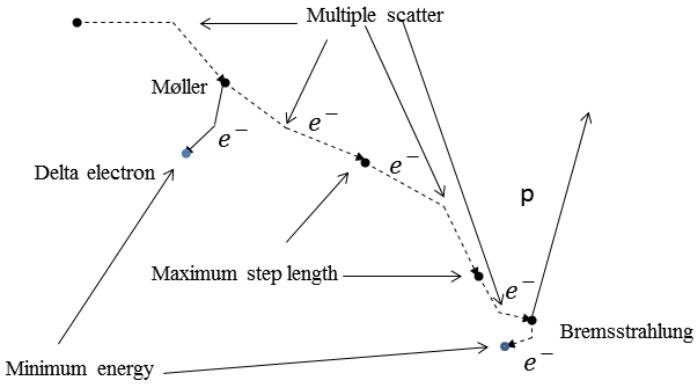

Figure 2.5.: The simulated electron trajectory demonstrates the CH approach. It is terminated when either the maximum step size (s_{max}) is achievd or a hard collision is ocurred. At the end of each step the electron modifies its direction and energy, this is sampled using the multiple scattering approach. Reproduced from [40].

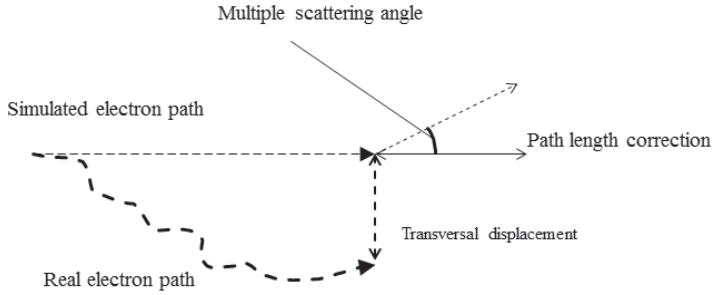

Figure 2.6.: A comparison between the CH technique with a multiple scattering angle and a probable real electron path. In this method, the path length and the transversal displacement should be considered. Reproduced from [40].

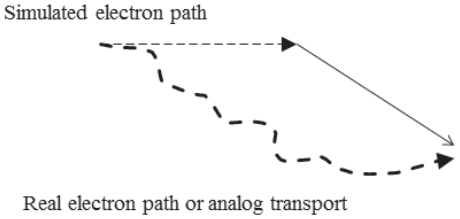

Figure 2.7.: The electron is simulated using the random hinge method. Using this method, path length corrections (PLC) and transversal displacements (TD) are considered. Reproduced from [40].

2.5.1. Continuous energy loss

The mean loss of energy dE related to a charged particle during a CH step length ds at point $\vec{r}$ is given by the restricted collision stopping power and restricted radiative stopping power as

$$L\left(\vec{r}, E, E_c, k_c\right) = L_{col}\left(\vec{r}, E, E_c\right) + L_{rad}\left(\vec{r}, E, k_c\right) \tag{2.18}$$

with

$$L_{col}\left(\vec{r}, E, E_c\right) = N\left(\vec{r}\right) \int_0^{E_c} dE' E' \sigma_{col}\left(\vec{r}, E, E'\right) \tag{2.19}$$

and

$$L_{rad}\left(\vec{r}, E, k_c\right) = N\left(\vec{r}\right) \int_0^{k_c} dk' k' \sigma_{col}\left(\vec{r}, E, k'\right). \tag{2.20}$$

$N\left(\vec{r}\right)$ is the quantity of atoms per unit volume at point $\vec{r}$.

In other words, the collision and radiation stopping power integrations (eqs. (2.3) and (2.5)) are, in this case, limited to energies below E_c and k_c. It means that the amount of energy transferred to secondary electrons is constrained to be less than E_c and the corresponding value of secondary bremsstrahlung photons is limited to be less than k_c. Furthermore, collisions with energy transfer larger than E_c or k_c to secondary particles are simulated explicitly within the CH scenario. Assuming E_0 as the initial charged particle energy at the beginning of the CH step, the electron energy at the end of the step s is

$$E_1 = E_0 - \Delta E, \tag{2.21}$$

where ΔE is the energy loss during the transport. Moreover, eq. (2.18) shows that crossing a material interface, the $L(\vec{r}, E, E_c, k_c)$ function takes account of the change in the stopping power values [40, 65, 67].

2.5.2. Multiple scattering and transport mechanics

As it is shown in fig. 2.6, in a CH technique, electrons are transferred on straight paths along one CH step length. This approach is an approximation due to the fact that electrons move in curved paths. To consider this in a CH step, an angular deflection is sampled based on a multiple scattering method. According to this method, a combined effect of all elastic and semielastic (soft) interactions on the charged particle's energy, direction and position during one step is calculated and employed at the end of the step, which is illustrated in fig. 2.6. Multiple scattering theory of Goudsmit and Saunderson is implemented in EGSnrc system [20]. The accurate multiple scattering angle even in case of large scattering angles of electrons can be estimated by help of these algorithms .

There are still some complications regarding the above-mentioned multiple scattering algorithms. As it is demonstrated in figure 2.6, the multiple scattering angle is employed at the end of a CH step. This approximation has still some contradictions with reality. The comparison of the trajectory of a real electron and a CH electron in fig. 2.6 shows that the CH step size is overestimated. Furthermore, the real electron range is smaller than the sampled one because it has a curvature path. Moreover, the electron range-straggling is ignored in previous CH step scenario.

Therefore, some modifications are required to be applied on a CH step. Recently, some corrections have been employed to CH algorithms. For example, Penelope and XVMC Monte Carlo systems use random hinge technique (figure 2.7). Based on this technique, path length correction (PLC) and transverse displacement (TD) algorithms are integrated. The PLC algorithm amends range overestimation and straggling and TD algorithm considers the lateral displacement of a real electron path compared to the straight path way of a CH electron. Based on random hinge technique, the multiple scattering method is employed between two random number subsets instead of being sampled at the end of a CH step. This results in a more accurate simulation of PLC and TD displacements. Another precise correction technique referred to as "parameter-reduced electron-step transport algorithm" (or so-called PRESTA-II) is implemented in EGSnrc. For more details, readers are encouraged to read [54].

2.6. Cavity theory

The absorbed dose in water, D_w, from electrons with an initial fluence function differential in energy, $\Phi_w^e(E)$ (see subsection 2.7.1), is given by

$$D_w = \int_0^{E_{max}} \Phi_w^e(E) \left(\frac{s(E)}{\rho} \right), \tag{2.22}$$

where $\frac{s(E)}{\rho}$ is the electron unrestricted mass collision stopping power of the water. This equation requires the so-called δ-equilibrium or charged particle equilibrium (CPE) to be assured. This condition generally implies to balance of energy at the region of measurement. As an example, CPE is not met in buildup region or in penumbra region of a beam. As it is shown in fig. 2.8, in case of CPE, the energy that is transported by electrons out of the region is equal to the energy transferred by incoming electrons and absorbed in the region. In other words, δ-equilibrium or the CPE exists for a region V, if every electron of a known type, energy and direction of movement leaving this region is replaced by an identical electron with the same type and energy coming into the region V.

The fundemental problem with respect to the measurement of absorbed dose by ion chambers is that, they can measure the ionization and ultimately absorbed dose in their air cavity (D_{air}) while the absorbed dose in water (D_w) is required.
Therefore, a correction factor (f) should be added to the dose measured with the ion chamber and this factor is determined using the cavity theory and is predominantly given by

$$f = \frac{D_w}{D_{air}}. \tag{2.23}$$

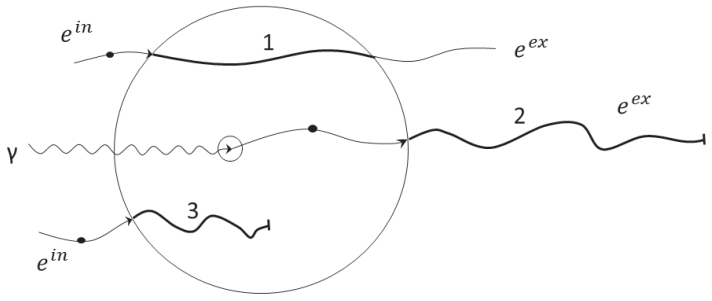

Figure 2.8.: Schematic illustration of charged particle equilibrium. The thick lines represent either the energy absorbed in the chamber volume or removed out of it. In case of charged particle equilibrium, the sum of the absorbed energy along the lines 1+3 is equal to the removed energy along the line 2. Reproduced from [68].

2.6.1. Bragg - Gray cavity theory

The first suggestion for f determination is known as Bragg - Gray theory. Based on this theory, the f factor is given by

$$f = \frac{D_w}{D_{air}} = \frac{\int_0^{E_{max}} \Phi_w^e(E) \left(s(E)/\rho\right)_w dE}{\int_0^{E_{max}} \Phi_w^e(E) \left(s(E)/\rho\right)_{air} dE} = \left(\frac{\bar{s}}{\rho}\right)_{air}^{w}, \tag{2.24}$$

where $\left(\frac{\bar{s}}{\rho}\right)_{air}^{w}$ is the mean unrestricted mass collision water-to-air stopping power ratio. It is important to point out that in equation (2.24), the charged particle fluence spectrum $\Phi_w^e(E)$ (see subsection 2.7.1) is that of water in the numerator as well as denominator and is differential in energy. In this equation not only the CPE (δ-equilibrium) condition must be met but also two prerequisites of Bragg-Gray cavity must be fulfilled. Firstly, the cavity is small enough (compared to electron range) to avoid disturbing the fluence, energy fluence spectrum and angular distribution of electrons. In other words, no change in these parameters occurs when electrons pass through the air cavity. Secondly, delivered dose to the cavity is only caused by the electrons entering (from surrounding water) into the cavity, that is, deposited dose due to photon interactions in the cavity region is ignored. In other words, the energy transported to the cavity by secondary electrons produced by photons in the cavity is negligible compared to total energy transported to the cavity. Thirdly, the fluence distribution of electrons from all generations is spatially independent. Second condition also implies that all electrons delivering the dose inside the cavity are generated outside the cavity and entirely cross the cavity. Therefore, no secondary electrons are generated inside the cavity and no electrons stop whithin the cavity [39, 68].

2.6.2. Spencer - Attix cavity theory

As previously noted, the above-mentioned equation associated with Brag-Gary theory demands the CPE (δ-equilibrium) condition. It assumes that δ electrons inside the cavity region are neither created nor absorbed. This is unrealistic due to finite size of the cavity and the lower density of air compared to water. Spencer and Attix published a modification to the Bragg-Gray theory. According to them, the previous theory (Bragg-Gray) is considered in the range $[\Delta, E_{max}]$, below which the generated particles are absorbed locally and do not cross the cavity [69]. The Δ parameter is so-called cut-off energy depending on the size of the cavity region and the range of electrons and is commonly set equal to the electron energy having a range large enough to cross the cavity. In other words, δ-electron equilibrium is created, in which stopping

the electrons with energies below Δ in the cavity is compensated by transporting the electrons with energies larger than Δ out of the cavity. Based on this modification, the f factor following the Spencet-Attix theory is given by the expression:

$$f = \frac{D_w}{D_{air}} = \frac{\int_{\Delta}^{E_{max}} \Phi_w^e(E) \left(L(E)_{\Delta}/\rho\right)_w dE + \Phi_w^e(E) \left(s(E)_{\Delta}/\rho\right)_w \Delta}{\int_{\Delta}^{E_{max}} \Phi_w^e(E) \left(L(E)_{\Delta}/\rho\right)_w dE + \Phi_w^e(E) \left(s(E)_{\Delta}/\rho\right)_{air} \Delta} = \left(\overline{\frac{L_{\Delta}}{\rho}}\right)_{air}^{w}, \tag{2.25}$$

where $\left(\overline{\frac{L_{\Delta}}{\rho}}\right)_{air}^{w}$ is the mean restricted collision water-to-air stopping power ratio. Furthermore, the term $\int_{\Delta}^{E_{max}} \Phi_w^e(E) \left(L(E)_{\Delta}/\rho\right)_w dE$ demonstrates the energy deposition due to charged particles with energy larger than Δ; whereas $\Phi_w^e(E) \left(L(E)_{\Delta}/\rho\right)_w \Delta$ is the so-called 'track-end' term, taking into account the energy deposited by charged particles with energies smaller than Δ [70]. It should be noted that the Spencer-Attix theory still follows the Brag-Gray theory prerequisites which implies a small cavity that does not perturb the electron fluence. However, a real ion chamber has walls, stem and central electrode which leads to including a so-called perturbation factor (P_i) to the previous expressions resulting to the following equation:

$$D_w = D_{air} \times \left(\overline{\frac{L_{\Delta}}{\rho}}\right)_{air}^{w} \times \prod P_i, \tag{2.26}$$

which finally corrects the existence of a real ion chamber in a water phantom. More details can be found in literature [20].

2.7. Dosimetry of electron beams

2.7.1. Fluence

The particle fluence Φ gives the number of particles dN that cross a sphere of cross-sectional area, dA:

$$\Phi = \frac{dN}{dA}, \tag{2.27}$$

which has commonly the unit particles/cm^2. The advantage of a sphere of cross-sectional area dA is that it is always perpendicular to the direction of incoming particle and therefore the fluence does not depend on the angle of the radiation. *planar* particle fluence is defined as the number of particles passing through a plane per unit area. As a result, it is dependent on the

incidence angle of the particle beam [34].

2.7.2. Energy fluence

The energy fluence Ψ is defined as the total amount of energy (dE) incident on a sphere of cross-sectional area dA and can be given as:

$$\Psi = \frac{dE}{dA}. \tag{2.28}$$

The energy fluence has the unit of J/m^2. Energy fluence can also be obtained from particle fluence by employing a relationship given as :

$$\Psi = \frac{dN}{dA}E = \Phi E, \tag{2.29}$$

where dN corresponds to the number of particles with energy E.

In most cases as well as in this study, the particles have a spectrum therefore the previous concept should be adapted to them. In other words, particle fluence spectrum and energy fluence spectrum present the realistic characteristics of photons and electrons and can be given by

$$\Phi_E(E) = \frac{d\Phi}{dE}(E) \tag{2.30}$$

and

$$\Psi_E(E) \equiv \frac{d\Psi}{dE}(E) = \frac{d\Phi}{dE}(E) \times E, \tag{2.31}$$

where $\Phi_E(E)$ and $\Psi_E(E)$ corresponds to particle fluence spectrum and energy fluence spectrum, differential in energy E , respectively [35].

2.7.3. Beam quality determination

Regarding electron beams, the beam quality index is the half-value depth in water R_{50}. This is the depth in water (in gcm^{-2}), at which the absorbed dose is 50% of its value at the absorbed-dose maximum. The reference conditions for the determination of R_{50} require measuring in water or solid phantom with parallel-plate or cylindrical ionization chambers at SSD of 1000 mm and $100\times100\,\mathrm{mm}^2$ field size, taking the effective point of measurement into account [7]. When apply-

ing an ionization chamber, the measured quantity is half of the depth-ionization distribution in water, $R_{50,ion}$. This is the depth in water, at which the ionization current is 50% of its maximum value [7]. The quality index (R_{50}) is then obtained from the $R_{50,ion}$ value using

$$R_{50} = 1.029\, R_{50,ion} - 0.06 g\, cm^{-2}. \tag{2.32}$$

2.7.4. Absorbed dose to water under reference conditions

The reference conditions to obtain absorbed dose to water in electron beams relevant to this study demand to use a water phantom with a parallel-plate ionization chamber positioned at z_{ref} at SSD of 1000 mm and filed size of 100×100 mm^2. The reference depth z_{ref} is given by [7]:

$$z_{ref} = 0.6 R_{50} - 0.1 g\, cm^{-2} \left(R_{50}\, in\, g\, cm^{-2}\right). \tag{2.33}$$

This depth is near to the depth of dose-maximum z_{max} at beam qualities $R_{50} < 4 gcm^{-2}$ ($E <$ 10 MeV), which is applicable to this study. This depth has been demonstrated to remarkably decrease the deviations due to using different machines in calibration factor of chamber and the ultimate accuracy validates its application, especially for parallel-plate ionization chambers [7].

2.7.4.1. IAEA TRS-398 dosimetry protocol

The IAEA TRS-398 code of practice was used as the reference for determination of absorbed dose to water in this study and is described briefly [7]. This code of practice suggests an internationally unified method in order to determine the absorbed dose to water, based on calibrated ionization chambers applied in radiation therapy. The suggested method can be employed for photon, electron, proton and heavy-ion beams which are used for external radiotherapy. Calibration of ionization chamber in terms of air kerma involves large number of performing steps and high uncertainty associated with several physical quantities applied (up to 4%) [71]. The quantity kerma (kinetic energy released per unit mass) is defined as the ratio of dE_{tr} to dm, where dE_{tr} is the sum of the initial kinetic energy transferred to all the charged ionizing particles (electrons and positrons) that liberated by uncharged particles (photons) in a material of mass dm. Its unit is the same as for dose, that is, the Gray (Gy) with 1 Gy = 1 J/kg [72].

Utilizing air kerma can increase the final uncertainty in patient dose delivery. Therefore, efforts have been undertaken in primary standard dosimetry laboratories (PSDL) in order to develop standards for absorbed dose to water. For this purpose, procedures such as ionization method, chemical dosimetry, and water and graphite calorimetry have been developed [7]. These improvements led to a change in the current quantity of calibrating ionization chambers and provided calibration factors based on absorbed dose to water, $N_{D,w}$, to be used for radiotherapy beams. Up to this time, many PSDLs have supplied $N_{D,w}$ calibration factors at Co-60 gamma beams obtained in so-called standard conditions of pressure 101.3 kPa and temperature 20°C.

At secondary standard dosimetry laboratories (SSDL), these calibration factors are utilized to calibrate ionization chambers for absolute dosimetry using Co-60 beams under reference conditions. Furthermore, numerical calculations (e.g. Monte Carlo methods) are applied to determine the beam quality correction factors for chambers used in high-energy photons and electron beams. Making use of ionization chambers in clinical dosimetry, in which the measuring conditions differ from that of SSDLs, some correction factors are mandatory. The TRS-398 dosimetry protocol is based on a calibration factor N_{D,w,Q_0} related to absorbed dose to water for a reference beam of quality Q_0 (usually a ^{60}Co beam). This code of practice applies to electron beams with energies in the range between 3 and 50 MeV.
Based on this protocol, the absorbed dose to water at the reference depth z_{ref}, in an electron beam of quality Q and in the absence of the chamber, is given by

$$D_w = M.k_{elec}.k_{TP}.k_{pol}.k_s.N_{D,w,Q_0}.k_{Q,Q_0}. \tag{2.34}$$

M refers to the reading of a dosimeter used as external monitor (unit C), k_{elec} is the calibration factor for the electrometer. The k_{TP} correction factor is a term that takes into account the probable effect of different temperatures and pressures. The k_{pol} correction factor implies to a term that amends the ionization chamber response for the influence of a variation in polarity of the polarizing voltage used for chamber dosimetry. k_s corresponds to the ion recombination correction factor which adjusts the chamber response for the lack of complete charge collection caused by ion recombination which is discussed in detail later (see section 4.1).

In addition, the N_{D,w,Q_0} parameter is the calibration factor based on absorbed dose to water for an ionization chamber at ^{60}Co gamma rays. Finally, the k_{Q,Q_0} factor corrects for the deviation between the response of an ionization chamber in the ^{60}Co gamma rays (beam quality Q_0)

applied for chamber calibration and in the actual beam quality of the user, Q. More details are provided below regarding the k_{Q,Q_0} factor [7]. The k_{Q,Q_0} could be written as

$$k_{Q,Q_0} \approx \frac{(s_{w,air})_Q}{(s_{w,air})_{Q_0}} \frac{p_Q}{p_{Q_0}}, \tag{2.35}$$

which depends merely on proportions of unrestricted stopping-power ratios and perturbation correction factors associated with the beam qualities Q and Q_o. For a given electron beam at reference depth (z_{ref}), the $\frac{(s_{w,air})_Q}{(s_{w,air})_{Q_0}}$ term could be determined by

$$\frac{(s_{w,air})_Q}{(s_{w,air})_{Q_0}} = 1.106 - 0.1312\,(R_{50})^{0.214} \tag{2.36}$$

with R_{50} in cm. The only factors related to chamber specifications are the perturbation correction factors p_Q and p_{Q_0}. The $\frac{p_Q}{p_{Q_0}}$ is in general defined as

$$\frac{p_Q}{p_{Q_0}} = \frac{(p_{cav} p_{dis} p_{wall} p_{cel})_Q}{(p_{cav} p_{dis} p_{wall} p_{cel})_{Q_0}}. \tag{2.37}$$

p_{cav} accounts for the difference in the in-scattering of electrons (and consequently electron fluence) in the presence of air instead of water in chamber cavity [7, 9]. The p_{dis} amends the influence of replacing a volume of water with the chamber cavity on the real attenuation or build-up effect which is considerably smaller in the air compared to water and causes the upward shift of the effective point of measurement. This factor is employed when the reference point of the chamber is taken to be at the chamber centre and depends on the type of employed beam and chamber. The p_{wall} factor corrects the deviation of wall material from water and p_{cel} accounts the influence of central electrode. For paralleled plate ionization chambers, p_{cav} and p_{cel} are close to unity and omitted (for beam quality of Q). Therefore, the final equation can be stated as:

$$\frac{p_Q}{p_{Q_0}} = \frac{(p_{wall} p_{dis})_Q}{(p_{cav} p_{dis} p_{wall})_{Q_0}}. \tag{2.38}$$

Nevertheless, the experimental and theoretical methods are not yet entirly validated to deliver reliable results of each specific factor in equation (2.38). However, $\frac{p_Q}{p_{Q_0}} = 0.985$ has been suggested in literature which was determined based on an experimental method [9]. In this method, the absorbed dose in water at filed size of $200 \times 200\,\mathrm{mm^2}$ for a calibrated cylindrical chamber and the parallel-plate chamber positioned at depth of z_{max} and irradiated with high energy electron beam is measured. As a result, the $\frac{p_Q}{p_{Q_0}}$ is obtained based on equations (2.34), (2.35) and (2.36). The accurate determination of this factor is still under progress and more details can be found in the literature [73, 74, 75, 76].

2.7.5. Considerations for dosimetry under non-reference conditions

Under nonreference conditions, an extra factor k_{NR} should be added to the equation (2.34) in order to include possible effects. k_{NR} can be given by

$$k_{NR} = \frac{s^{\Delta}_{w,air}(z)}{s^{\Delta}_{w,air}(z_{ref})} \frac{p_{cav}(z)}{p_{cav}(z_{ref})} \frac{p_{wall}(z)}{p_{wall}(z_{ref})} \tag{2.39}$$

in which, the $s^{\Delta}_{w,air}(z)$ is the Spencer-Attix restricted mass collision stopping power ratio (see subsection 2.6.2) as a function of depth z and is given by [19]

$$s^{\Delta}_{w,air}(z) = \frac{a + bx + cx^2 + dy}{1 + ex + fx^2 + gx^3 + hy}, \tag{2.40}$$

where $x = ln(R_{50})$ and $y = \frac{z}{R_{50}}$, (R_{50} in cm) [9]. The values for the constants are $a = 1.752$, $b = -0.50867$, $c = 0.08867$, $d = -0.08402$, $e = -0.42806$, $f = 0.06463$, $g = 0.003085$ and $h = -0.1246$. Δ is a cut-off energy below which the particle's energy is assumed to be deposited locally. The standard deviation of $s^{\Delta}_{w,air}(z)$ is 0.4%. Based on TRS-398 protocol and according to equation (2.36) and the known value of $(s_{w,air})_{Q_0} = 1.133$ for ^{60}Co an expression for $s^{\Delta}_{w,air}(z_{ref})$ can be stated by

$$s_{w,air}(z_{ref}) = 1.253 - 0.1487\,(R_{50})^{0.214}. \tag{2.41}$$

Because of the fact that there is still neither validated experimental nor theoretical data regarding the dependency of p_{cav} and p_{wall} to depth, z, as required in equation (2.39) for parallel-plate chambers, these perturbation factors are assumed to be close to unity and therefore omitted from this equation. Thus, the equation (2.39) for advanced Markus chamber can be expressed

as:

$$k_{NR} \approx \frac{s^{\Delta}_{w,air}(z)}{s^{\Delta}_{w,air}(z_{ref})} \tag{2.42}$$

in which $s^{\Delta}_{w,air}(z)$ and $s^{\Delta}_{w,air}(z_{ref})$ parameters are given by equations (2.40) and (2.41). Recent publications exhibit a relation between p_{wall} and p_{cav} with depth which are explained in more details for cylindrical and Markus chamber in current protocols. However, there is no data available regarding the Advanced Markus chamber [9, 7, 77, 78].

2.7.6. Ion recombination

The ionization Q produced in any gas is related to the absorbed dose D (J/kg) in the gas by

$$D = \frac{Q}{\rho V} \cdot \frac{\overline{W}}{e}, \tag{2.43}$$

where Q is the charge (in coulombs) produced in the chamber, ρ is the density (kg/cm^3) of air, V is the chamber volume (m^3), and $\frac{\overline{W}}{e}$ is the mean energy spent per unit charge (J/C) produced in air. In practical dosimetry however, the charge that is collected by the biased electrode in the chamber and measured by the electrometer circuit, $Q^{'}$, is less than the charge produced, Q, because of recombination of some positive and negative ions within the chamber.

Recombination refers to the charge transfer which results to neutral atoms or molecules. The particles participate in this transfer process are charged ions with opposed signs, the electron will only change its partner. The result of the interaction is then two heavy uncharged particles, as it is illustrated in fig. 2.9 (upper). If a free electron is captured by a positive charged ion, the result will be a single heavy uncharged particle, as it is depicted in fig. 2.9 (lower). Therefore, through recombination process, some of the primary charge produced in the chamber will be vanished and the amount of charge collected by the biased electrode will be reduced.

The probability for each charge-transfer process is dependent on the density (spatial distribution) of ions and electrons, the $\frac{\overline{W}}{e}$ value of ions, the filling-gas pressure and the chamber's operating voltage. Recombination of ions with each other is more frequent than that of electrons with ions because, due to higher mobility of electrons, they will either be sucked off by the electric field of chamber or be attached to the neutral atoms or molecules (provided, enough

$\frac{\overline{W}}{e}$ is available) forming negative ions. Part of free electrons will therefore be replaced by the negative ions which will be less accelerated by the electric field because of their greater weight.

Recombination may occur in either of two ways, which are designated initial recombination and general recombination, respectively. On the one hand, if the ions which recombine were produced by a single ionizing particle track and unite before they have had time to move far from their initial configuration, this process is referred to as initial recombination. This process is independent of dose rate because, only the recombination along the track of a single ionizing particle is considered and the passage of further particles will not be taken into account. It occurs particularly in the wake of densely ionizing particles such as protons, alpha particles and other nuclear fragments. For beams other than heavy ions, initial recombination is generally less than 0.2%.

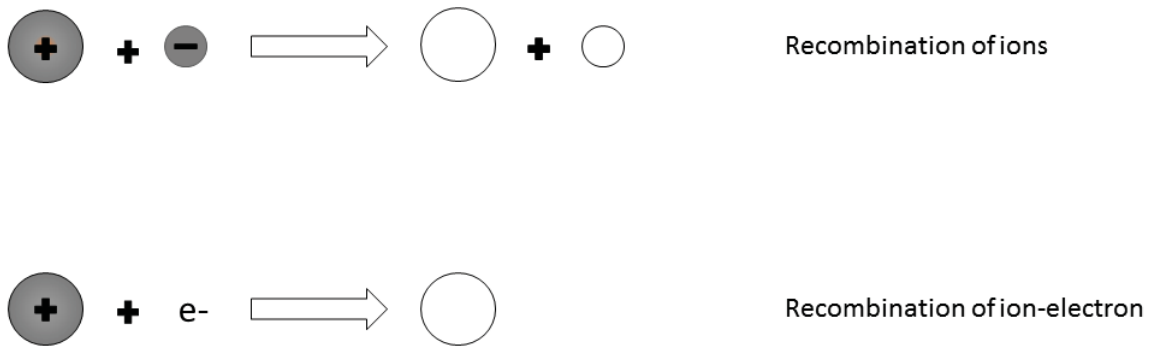

Figure 2.9.: Charge transfer processes by interaction among positively and negatively charged ions and free electrons in the gas volume of an ionization chamber. Upper: charge transfer between positive and negative ions. Lower: recombination of a free electron with a positive ion. In both situations loss of charge occurs. Reproduced from [68].

General recombination, on the other hand, occurs between those ions which escape initial recombination as soon as diffusion has brought about the overlapping of the initially discrete groups of ions (see fig. 2.10 in subsection 2.7.7). The volume recombination is dependent on the dose rate because, the higher the dose rate becomes, the larger the density of charged particles will be. Both effects depend on the chamber geometry and on the applied polarizing voltage. In pulsed radiation, the dose rate during a pulse is relatively high and general recombination is often significant [7, 34, 79].

2.7.7. Ion recombination correction factor for parallel-plate chambers exposed to pulsed irradiation

As it shown in fig. 2.10 on the top, by irradiating the gas volume through a single short pulse, a uniform distribution of ions also a spatially constant charge density in the chamber volume will be generated. Applying external voltage to chamber electrodes, the generated ions will be spatially separated and shifted toward the opposite polarized electrodes (fig. 2.10, middle). Through this, a time-dependent charge separation occurs which is a function of chamber characteristics. Recombination is possible as long as partial charge volumes overlap each other. The overlapping time is dependent on the electric field power and mobility of ions. The opposite charge voluems will finally seperate and the recombination is not possible anymore (see fig. 2.10, down).

In an attempt to assess the recombination correction factor, Boag suggested a model for determination of chamber collection efficiency for parallel-plate ionization chambers and pulsed beams in 1950 [79]. The formula for collection efficiency, f, of a parallel-plate ionization chamber exposed to a sudden pulse of uniform ionization may be written as

$$f = \frac{1}{u} ln(1+u), \tag{2.44}$$

where

$$u = \frac{(\alpha/e)}{(k_1+k_2)}(\frac{\rho d^2}{V}) \tag{2.45}$$

or

$$u = \mu(\frac{\rho d^2}{V}) \tag{2.46}$$

and $\alpha =$ ionic recombination coefficient, e = electric charge, k_1, $k_2 =$ mobilities of positive and negative ions respectively, $\rho =$ initial charge density of positive or negative ions created by the pulse, d = electrode spacing, V = collecting voltage and $\mu =$ a single constant embodying α, e, k_1 and k_2 which is therefore dependent on the chamber filling gas and ambient conditions (gas pressure, temperature and humidity).

The ion recombination correction factor is then defined as the reciprocal of the chamber efficiency ($k_s = 1/f$). The principal assumptions made were that the electrons liberated in the

gas immediately attach themselves to oxygen molecules to form negative ions and therefore no free electron is collected and those ions of both signs move with constant mobilities k_1 and k_2 and exhibit a fixed recombination coefficient, independent of filed strength. This means that negative oxygen ions and not electrons are the negative charge carrier in air. It was also assumed that the pulse repetition frequency was low enough to allow the ions from one pulse to be swept away before the next occurred.

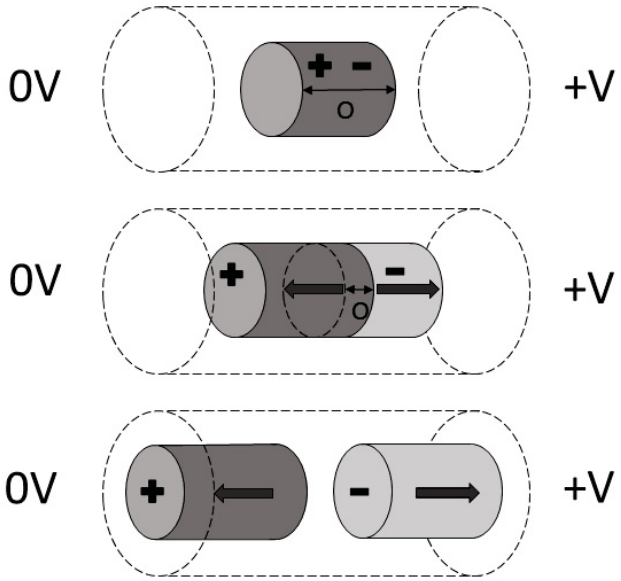

Figure 2.10.: Temporal development of charge distribution in an irradiated gas volume of an ionization chamber after a single pulse. Top: positive and negative ions are distributed homogeneously and the overlapping (O) is maximal. Middle: due to applied voltage, the ions of opposite signs separate, the overlapping region decreases and the probability of recombination reduces. Down: partially-charged-volumes are completely separated and the recombination is no longer possible. Reproduced from [68].

3. Materials and Methods

3.1. NOVAC7 IOERT linac

The NOVAC7 IOERT linac is moved by a six axis robotic arm ($\pm x, \pm y, \pm z$). It produces high dose rate electron beams of 4-11 Gy/min with a pulse repetition rate of 5-50 Hz. It has been used in several European IORT facilities since 1998 and has notable advantages compared to other non-dedicated IORT treatment systems, such as small in size and light weight with different electron energies (3, 5, 7 and 9 MeV) and different cylindrical applicator sizes (30, 40, 50, 60, 70, 80 and 100 mm), each having three different bevel angles (0, 22.5° and 45°) [4]. By combining different energies and applicators, different dose-per-pulse, in the range of 4-42 mGy/pulse, are produced. This is a very high value of dose-per-pulse compared to conventional linear accelerators used in external beam radiation therapy ($\sim$0.1 mGy/pulse).

The radiation head of the NOVAC7 consists of the vacuum exit window (titanium), the monitor chambers (aluminum), and the collimation part (PMMA). The exit window of the accelerating waveguide is a 60 µm thick titanium foil. Two monitor ionization chambers have a volume of $\sim$630 mm^3, each made of two 50 µm thick aluminium foils. The system does not use scattering filters which are the main source of stray radiationin in conventional linacs. Consequently, it is complicated to modulate the high dose rate of the NOVAC7 linac. The SSD is approximately 800 mm.

As it is shown in fig. 3.1 , the beam collimation is performed through PMMA consisting of two separated sections. The upper part which is docked to the accelerator's head is called adapter and the lower part which is in contact with the patient is called applicator. The NOVAC7 has a hard-docking system, in which the applicator would be hold on the patient. Then the linac moves toward the applicator and the adapter would be aligned and docked to the applicator. The set of applicators consist of cylindrical tubes with a wall thickness of 5 mm. Its length is constant (500 mm). In table 3.1 several important characteristics of this linac are presented.

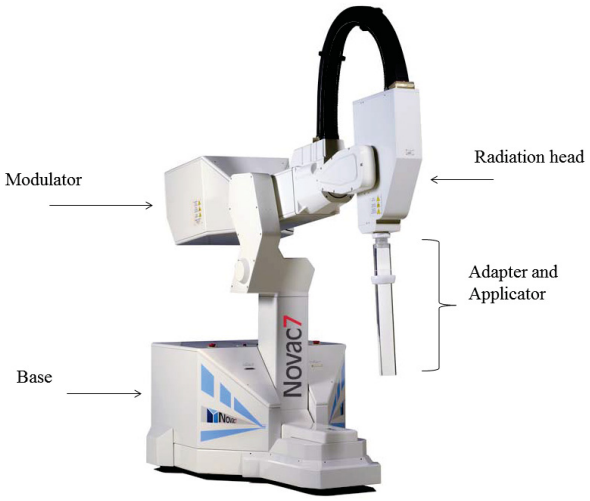

Figure 3.1.: NOVAC7, dedicated mobile electron linear accelerators for IOERT, mainly consisting of base, modulator, radiation head, adapter and applicator. Modulator accumulates electrical power for Magnetron which generates electromagnetic wave pulse. The radiation head including the wave guide is responsible for electron acceleration. Adapter and applicator are used for beam collimation [80] .

Table 3.1.: NOVAC7 technical data and parameters based on the manufacturer technical user guide. Only the most important characteristics are listed below.

Dimensions ($L \times M \times H; m$)	$2.3 \times 1 \times 1.9$
Max. energy (MeV)	9
Beam current (mA)	1.5
Number of cavities	11
Pulse duration (µs)	4.2
Pulse repetition frequency (Hz)	5

3.2. Radiation detectors

There are several types of radiation detectors with different features which are used in radiation dosimetry. Some common characteristics relevant to this study are expected from all these detectors and are briefly described below.

Stability: the output of a detector should be reproducible over a long period of time as well as over the range of applied dose being studied.

Dose linearity: over the dose range of interest, the detector response should be linear.

Dose rate independence: the detector response should be independent of the applied dose rate.

Energy response: the response of the detector should be proportional to the absorbed dose

regardless of the beam quality (energy) used.

S**patial resolution:** the sensitive volume of the detector should be small enough to provide acceptable resolution where high dose gradients occur. However, the smaller the sensitive volume is, the larger the signal-to-noise becomes (i.e. increased uncertainty).

Perturbation: the detector should be designed in a way that the fluence perturbation of the beam is minimized. In this study, ionization chambers and radiochromic films were utilized as radiation detectors. Their characteristics are briefly discussed below [81].

3.2.1. Ionization chambers

Ionization chambers are established as the standard dosimeters due to their stability, simple design, high sensitivity, dose linearity, high accuracy, real-time readout and ease of use. A typical design of an ionization chamber incorporates a protected cavity filled with air and collecting electrode(s) which are connected to an electrometer by a coaxial/triaxial cable. A polarization voltage is applied to the electrodes, positive ions and free electrons which are produced by passage of radiation through the air cavity are collected. The ionization current is then measured by an electrometer and is proportional to the absorbed dose deposited in the chamber volume. . One of the main disadvantages of the ionization chambers is the lack of high spatial resolution which is caused by their large volume. Furthermore, the response is energy dependent because of filling air and therefore perturbation correction factors are applied to obtain a precise result. An uncertainty of about 1.5% is expected, using an ionization chamber for radiation dosimetry under reference conditions [7, 81, 82]. Two types of ionization chambers are typically utilized for radiation dosimetry, cylindrical and parallel-plate chambers. A brief description of these two chamber types is given next.

3.2.1.1. Cylindrical chambers

Cylindrical ionization chambers (also known as Farmer-type, thimble or compact chambers) consist of a cylindrical air volume with a central electrode surrounded by a wall. Particularly, pin-point chamber (model 31014 PTW, Freiburg/Germany) was used in this study, as shown in figure 3.2. The pin-point chamber consists of a 2 mm diameter and 5 mm long cylindrical air chamber with a central steel electrode with a PMMA (covered with graphite) wall and a sensitive volume of 15 mm^3. Its effective point of measurementat is $0.5r_{cyl}$ deeper than the

point of interest with r_{cyl} implying to the radius of the cavity of a cylindrical ionization chamber. The pin-point chambers have been particularly designed for cases where higher special resolution is required.

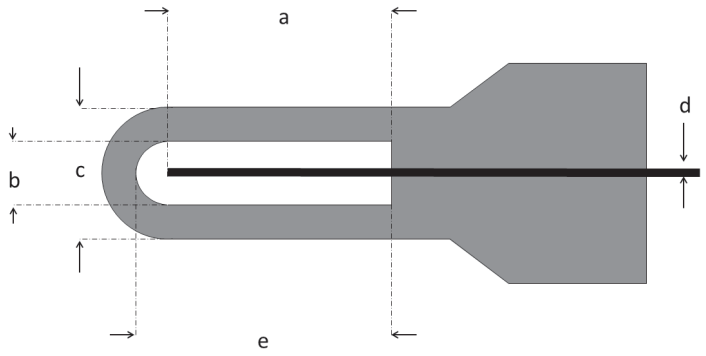

Figure 3.2.: PTW pin-point chamber model 31014 with a sensetive volume of 15 mm^3. a: the lenght of the central electrode in the sensitive volume (4.15 mm). b: the diameter of the sensitive volume (3.7 mm). c: the diameter of the graphite (9.7 mm). d: the diameter of the central electrode (0.3 mm). e: the length of the sensitive volume (5 mm). Reproduced from [83].

3.2.1.2. Parallel-plate chambers

A parallel-plate chamber is mainly made of two electrodes, a guard ring and a stem. The electrodes are parallel to each other producing a sensitive air volume and are positioned perpendicular to the incident beam direction. In this study, Advanced Markus parallel-plate chamber (model PTW 34045) was utilized which has a small sensitive volume of 20 mm^3 (2.5 mm radius and 1 mm depth). Since this chamber is well-guarded, the fluence perturbation through in-scattering of electrons is minimized which makes it ideal for high energy electron dosimetry. Using a protective cap, it is possible to employ this chamber for dosimetry in water. The effective point of measurement of this chamber is the inner surface of the entrance window. Figure 3.3 presents a schematic of an Advanced Markus chamber.

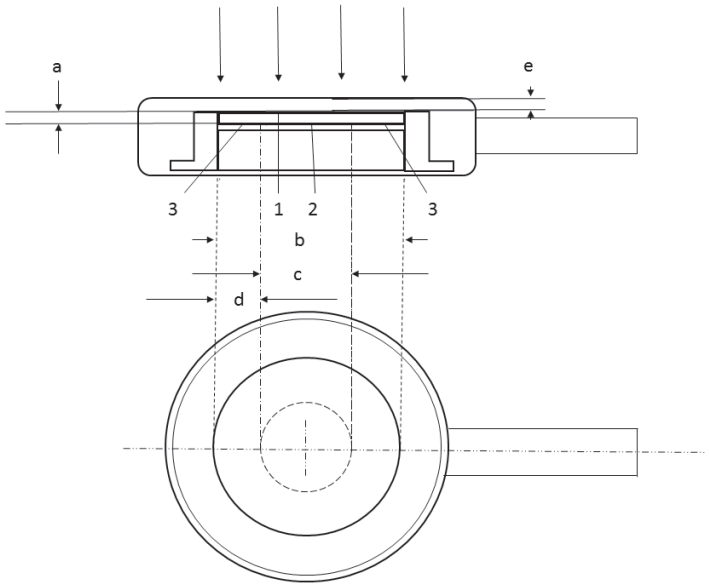

Figure 3.3.: PTW Advanced Markus chamber model 34045 with a sensitive volume of 20 mm^3. 1: the polarizing electrode. 2: the collecting electrode 3: the guard ring. a: the electrode seperation of the air cavity (1 mm). b: the diameter of polarizing electrode. c: the diameter of the collecting electrode (5 mm). d: the width of the guard ring. e: the hight of the protective cap (4.97 mm). Reproduced from [84].

3.2.2. Radiochromic film

The radiochromic film has been developed in recent years for radiation dosimetry [85]. In general, as the films are exposed to radiation, a polymerization occurs in the radiosensitive layer and this leads to a change in the optical density. The larger the delivered dose is, the higher the change in the optical density becomes. This change in the optical density is self-developing and is established after a few hours post irradiation. The high spatial resolution (≈0.35 mm at 75 dpi), low energy dependency and approximately tissue-equivalent material of radiochromic films provide an ideal field of application in radiotherapy, particularly where radiation fields with high gradient of dose are delivered. The color of the films do not change when being exposed to artificial light, but UV-light can lead to the polymerization of the active layer and cause the color change of the film. Furthermore, to evaluate the films accurately, they should be handled carefully (e.g. with cotton gloves) and kept in dark, constant ambient conditions (i.e. constant temperature) [86].

Gafchromic external beam therapy (EBT) is one of the most frequently used radiochromic film types in radiation therapy. This type of film (particularly EBT2) was utilized for determination of ion recombination correction factor (k_s) in this study and therefore a brief discussion is given below. As reported by the manufacturer Aschland (Wayne/USA), the Gafchromic EBT2 film is made by combining one yellow-dyed active layer, that is 30 μm thick over which a

5 µm topcoat is used [85]. A 25 µm adhesive layer is laminated above the topcoat. These three layers are covered with two clear polyester surfaces with a thickness of 50 µm (above the adhesive layer) and 175 µm (beneath the active layer), as it is presented in figure 3.4. These features allow reduction in coating anomalies, lower UV sensitivity, suitable water absorption and less damageable when being cut. EBT film has been demonstrated to allow very good response uniformity, low energy dependency, and is not dose rate dependent significantly [87]. The absorbence spectra of the active layer of EBT2 film peaks at 636 nm and the maximized sensitivity response is measured from the red color channel [85]. The EBT2 film is approximately tissue equivalent (atomic number $Z_{EBT} = 6.98$, which is comparable to that of water with $Z_{water} = 7.3$). The EBT2 films are commonly read out employing flatbed scanners with "red" or "red:blue" methods which are described extensively in literature [87]. More details about the properties of EBT2 Gafchromic film can be found in the literature [88, 89]. The uncertainty of radiochromic film has been published to be within 2–3% [90]. The protocol has been used to scan and analyze the data was based on the previous published investigations and reports [86, 87, 85, 91]. Furthermore, OmniPro I'mRT software (iba, Schwarzenbruck/Germany) was utilized to perform the subsequent analysis of the data [92].

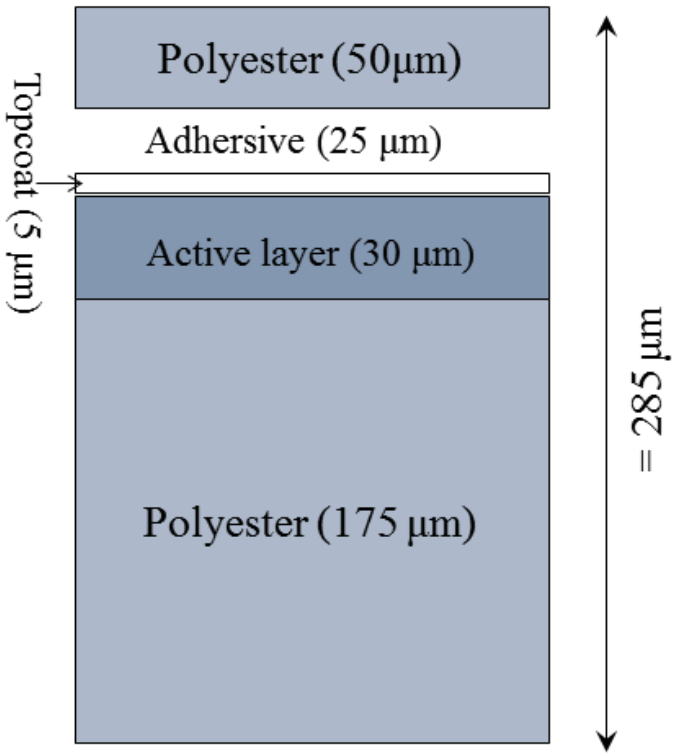

Figure 3.4.: Composition of a Gafchromic EBT2 film.

Through the so-called filmpanel included in this software the scanned films are uploaded in TIFF format. Then, the films are exported to the evaluation section of the software. Following this, using the calibration curve corresponding to each film slot, the absorbed dose is obtained or different analysis such as depth dose distribution and off-axis profiles are performed.

3.3. Ion recombination correction factor

3.3.1. Measurement

An absolute dose measurement in water $D_{w,Gaf}$ was performed using dose-per-pulse-independent Gafchromic EBT2 films [93]. The films were calibrated using a vented cylindrical ionization chamber type 30016 (PTW-Freiburg, Freiburg/Germany) with a sensitive volume of 300 mm^3. The ionization chamber was positioned centrally in a 100×100 mm^2 square field at a depth of 50 mm in a small water phantom ($300 \times 300 \times 300$ mm^3) type T41023 (PTW-Freiburg) at a SSD of 950 mm and was irradiated with 200 monitor units (MU). The polarizing voltage was set to +400 V. The reference dose irradiation system was a clinical linac of 6 MV photon beam (Precise, Elekta AB, Stockholm/Sweden). Corrections were made for polarity, temperature and air pressure. Humidity was measured as 47% but not corrected for, because of its insignificant effect on the results [94].

For dose calibration the films were cut into 50×50 mm^2 square sheets and were irradiated with 50, 100, 150, 200, 250, 300, 400, 500, 600, 700 and 800 monitor units. In addition, an unexposed film was used to obtain the background optical density (OD). The films were stored in a dark place at room temperature and evaluated 24 h after irradiation. The film digitalization was done using a commercial flat panel scanner (Perfection V750 PRO, Epson, Nagano/Japan). The films were positioned in the middle of the scanner area and processed with a scanning resolution of 72 dpi. The red channel was used in order to determine the net optical densities ($netOD$). The Omnipro I'mRT software was applied to obtain the relationship of OD values versus dose. The plot of dose as a function of optical density is shown in figure 3.5.

3.3.2. The reference recombination factor, $(k_s)_w^{ref}$

The absolute dose measurement was also carried out using an Advanced Markus chamber (PTW-Freiburg type 34045). An UNIDOS webline electrometer (PTW-Freiburg) was used for chamber read-out.

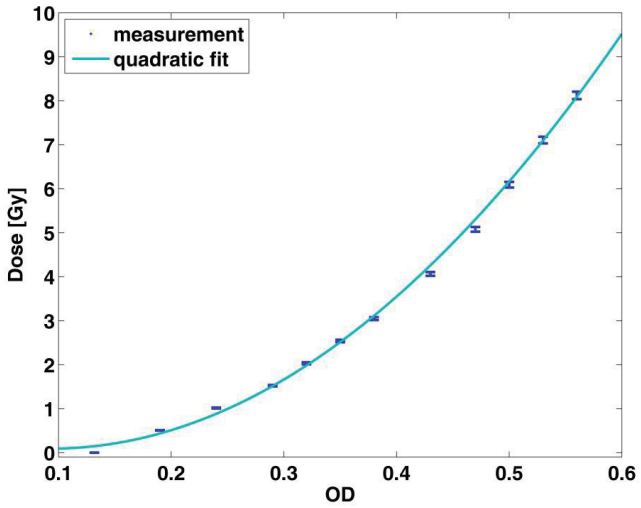

Figure 3.5.: Gafchromic EBT2 film calibration curve in terms of optical density (OD) versus absorbed dose to water, by using a photon beam of 6MV supplied by an Elekta Precise linear accelerator. The fit was obtained by using a quadratic function. The error bars show the combined uncertainty of the measured doses and ODs.

This chamber was used to determine the recombination correction factors $\left((k_s)_w^{ref}\,,\,(k_s)_{exp}^{jaff}\,,\,(k_s)_{th}^{TVA}\,,\,(k_s)_{th}^{B'}\,,(k_s)_{th}^{B''}\;and\;(k_s)_{th}^{B'''}\right)$ (see subsections 3.3.3, 3.3.4 and 3.3.5). Additionally, on the one hand, according to the IAEA TRS-398 dosimetry protocol [7], equation (2.34), absorbed dose to water at the reference depth z_{ref} for a reference beam of quality Q could be written as :

$$D_w = D'_w \cdot k_s \tag{3.1}$$

with

$$D'_w = M \cdot k_{elec} \cdot k_{T,P} \cdot k_{pol} \cdot k_{Q,Q_0} \cdot N_{D,w,Q_0}. \tag{3.2}$$

Here D'_w is the absorbed dose in water not corrected for ion recombination. On the other hand, it is supposed that

$$D_w = D_{w,Gaf}. \tag{3.3}$$

$D_{w,Gaf}$ is the absorbed dose measured by a Gafchromic EBT2 film. Following equations (3.1), (3.2) and (3.3) the reference value for the recombination correction factor ($(k_s)_w^{ref}$) is:

$$(k_s)_w^{ref} = \frac{D_{w,Gaf}}{D'_w} = \frac{D_{w,Gaf}}{M \cdot k_{elec} \cdot k_{T,P} \cdot k_{pol} \cdot k_{Q,Q_0} \cdot N_{D,w,Q_0}}. \tag{3.4}$$

3.3.3. Jaffé diagram, $(k_s)_{exp}^{jaff}$

The Jaffé diagram refers to a reciprocal plot of the chamber's reading $(1/M)$ against the reciprocal of the polarizing voltage $(1/V)$ [68]. Thus k_s can be obtained by linear extrapolation to an infinite chamber voltage $(1/V = 0)$, as illustrated in fig. 3.6. The dosimeter readings M were corrected for the polarity effect, temperature and pressure. In the case of pulsed beams, as recommended in the TRS-398 protocol, the range of linearity of a chamber must be established over a range of polarizing voltage up to the manufacturer's recommended maximum. According to the TG-51 dosimetry protocol, using voltages above normal operating voltages simply to reduce k_s should be avoided to prohibit gas multiplication [8]. In this study, the applied voltages were 50 V, 100 V,160 V, 200 V, 240 V and 300 V to obtain the Jaffé diagram which is shown in the next chapter. 10 min was paused between each measurement to allow the conditions in the chamber to stabilize. Each measurement was repeated three times with negative and positive polarity to proof the polarization effect.

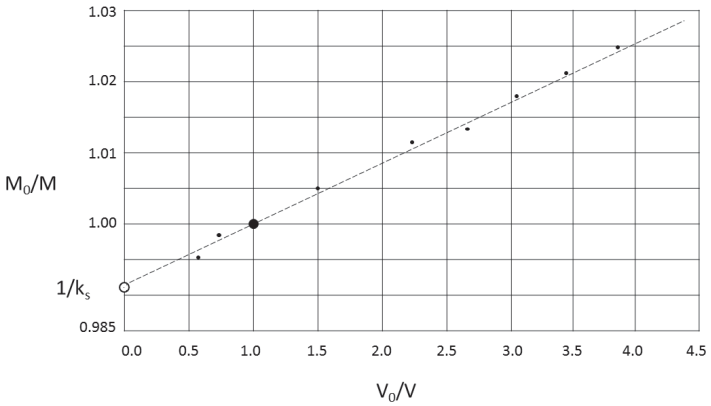

Figure 3.6.: Illustration of a Jaffé diagram for pulsed irradiation. The normalized measured signal M_0/M is depicted as a function of normalized chamber voltage V_0/V . V_0 is the operating voltage recommended by manufacturer. Applying this voltage produces M_0 signal. The intersection of the best-fit-straight-line with the axis of the reciprocal measured signal (open circle) delivers the ion recombination correction factor k_s. Reproduced from [68].

3.3.4. Two Voltage Analysis (TVA)

The Boag model presented in subsection 2.7.7 does not account for chamber to chamber variation within a given chamber type. In IAEA TRS-398 the following equation for obtaining the recombination correction factor is used [7]:

$$k_s = \frac{1}{f} = \frac{Q_s}{Q} = \frac{M_s}{M_V}, \tag{3.5}$$

where Q_s is the saturation charge and M_s is the saturation signal of the ion chamber. Saturation charge and signal refer to the charge and signal when all negative and positive ions are collected. Q and M_V are the actual readings of the chamber. Using the recombination model proposed by Boag (eq. 2.44) and also eq. 3.5, the ratio between the chamber's responses M_1 and M_2 at two different voltages V_1 and V_2 is written as

$$\frac{M_1}{M_2} = \frac{M_1 M_s^{-1}}{M_2 M_s^{-1}} = \frac{u_1^{-1} ln(1+u_1)}{u_2^{-1} ln(1+u_2)}, \tag{3.6}$$

where u has the same meaning as eq. 2.46. Using the relation $u_2 = \frac{V_1}{V_2} u_1$, the eq. 3.6 is written as

$$\frac{M_1}{M_2} = \frac{V_1}{V_2} \frac{ln(1+u_1)}{ln(1+V_1 V_2^{-1} u_1)}. \tag{3.7}$$

Weinhaus and Meli have solved eq. 3.7 numerically and have computed k_s (eq. 3.5) for different voltage ratios and chamber reading ratios [95]. Their results in the form of the coefficients of eq. 3.8 are used in IAEA TRS-398 protocol which is known as two voltage analysis (TVA) [7]. The prerequisite of the TVA method is that, the applied voltages must be selected from the linear region of Jaffé diagram. In this method collected charges M_1 and M_2 are obtained at the polarizing voltage V_1 and V_2, respectively. V_1 is the normal operating voltage and V_2 is a lower voltage and the ratio $\frac{V_1}{V_2}$ should ideally be ≥ 3. In this condition, the recombination correction factor based on the TVA method, $(k_s)_{th}^{TVA}$, at the normal operating voltage V_1 could be written

as:

$$(k_s)_{th}^{TVA} = a_0 + a_1 \left(\frac{M_1}{M_2}\right) + a_2 \left(\frac{M_1}{M_2}\right)^2, \tag{3.8}$$

where a_0 = 1.198, a_1 = -0.875 and a_2 = 0.677, corresponding to measurement condition of this study (pulsed radiation and $\frac{V_1}{V_2} = 3$), are given in TRS-398 dosimetry protocol [7]. Strictly, the polarity effect will change with the voltage, therefore M_1 and M_2 were both corrected for this effect.

3.3.5. Modified recombination models of Boag et al.

The Boag formula developed in 1950, eq. 2.44, for the recombination correction to ionization measurements of pulsed radiation which has been applied by dosimetry protocols is on the basis of a model that assumes conduction only by positive and negative ions and does not consider those electrons that escape attachment to oxygen molecules and so reach the electrode as free electrons [79]. The resulting deficit in the negative ion concentration causes a reduction in ionic recombination, which means, an increase in collection efficiency. 40 years later a theoretical model which takes account of the free-electron component has been proposed by Hochhäuser and Balk [96]. By oscillographic studies of the current from a fast-response ionization chamber, the rapid pulse due to electron collection was separated from the slow component due to ions [12]. In 1996, Boag, Hochhäuser and Balk suggested three modified expressions regarding the recombination process which deal with, in different ways, the free-electron component. Based on their model, in a plane-parallel chamber we can derive the initial spatial distribution of the negative ions between the plates, following the clearance of those electrons that escaped attachment. The fraction of all the electrons ejected by the pulse that will cross the electrode gap d without attachment (free electron fraction) is then

$$p = \frac{1}{ad}\left(1 - e^{ad}\right), \tag{3.9}$$

where a is the probability of attachment to oxygen molecules per unit length of the drift path. For a given ionization chamber with a uniform collecting field a will be constant throughout the chamber. Additionally, the negative ion, O^-, concentration which is made by the attachment

of electrons to the oxygen molecules (see fig. 2.9) is shown as n_z and is defined as following:

$$n_z = n(1 - e^{-az}), \tag{3.10}$$

where n refers to the initial concentration of the positive ions following the pulse of radiation. Regarding these, to calculate the recombination factor, different approximations of the n_z distribution in the chamber volume between two electrodes are made by Boag, Hochhäuser and Balk as it is shown in fig. 3.7 [96]. The first approximation (see model 1 (a) in fig. 3.7) is as follows:

$$(k_s)_{th}^{B'} = \frac{u}{ln\left(1 + \frac{e^{pu}-1}{p}\right)}, \tag{3.11}$$

where $u = \mu r \frac{d^2}{V}$ is a dimensionless parameter, r is the initial uniform charge density of the positive ions following a brief pulse of radiation, other parameters have the same meaning as previously described in eq. 2.46. This approximation assumes that the positive ion density is constant in the chamber's volume, but the negative ion density follows an exponential function across the chamber's volume and its density is constant at the level $(1-p)r$ between the plates.

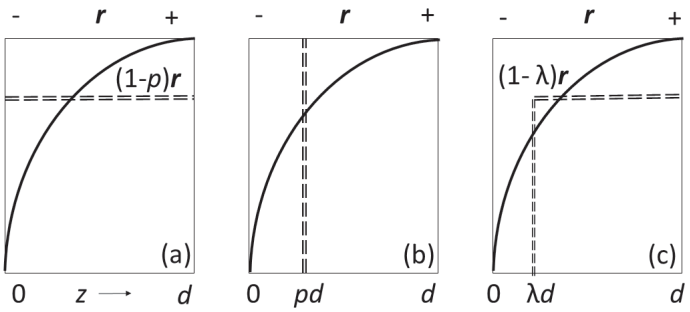

Figure 3.7.: Distribution of positive and negative ions following clearance of the free electrons in a parallel-plate ionization chamber. In all three models the positive ion charge density, r, is assumed to be constant between the electrodes. The true negative ion charge density however, is taken to follow a curve of the form of equation 3.10. The curves shown are for a 30% free-electron fraction, i.e. $p = 0.3$.
In model 1 (a) the negative ion charge density is assumed to be constant at the level $(1-p)r$ between the plates. In model 2 (b) the space $z < pd$ is assumed to be empty of negative charge and the residue of the space to be occupied by negative charge density r. In model 3 (c) the space λd is devoid of negative charge and the remainder of space is occupied by negative charge density $(1-\lambda)r$ where $\lambda = 1 - \sqrt{(1-p)}$ in order to make the free-electron fraction equivalent to p. Reproduced from [13].

The second approximation (see model 2 (b) in fig. 3.7) assumes that there is a layer, having width of pd near the negative electrode, which is depleted of negative ions and in the remaining space, $(1-p)d$, the negative ion density is equal to the density of positive ions. The formula for recombination correction factor derived from this approximation is:

$$(k_s)_{th}^{B''} = \frac{u}{pu + ln\left[1 + (1-p)\,u\right]}. \tag{3.12}$$

The third approximation (see model 3 (c) in fig. 3.7) considers both previous approximations in one, in which it assumes that there is a layer, λd, depleted of negative ions and in the rest area between the plates the density of negative ions is taken to be constant at the level $(1-\lambda)r$. This model fits the initial negative ion distribution given by the eq. 3.10 more closely and the recombination correction formula derived is as follows:

$$(k_s)_{th}^{B'''} = \frac{u}{\lambda u + ln\left[1 + \frac{e^{\lambda(1-\lambda)u}-1}{\lambda}\right]}, \tag{3.13}$$

where $\lambda = 1 - \sqrt{(1-p)}$. As the first model, the last two models assume that the positive charge density is constant between the both electrodes. The differences between the three models are different thickness of the layer free of negative charge and the different negative charge density in the reminder of the cavity space. In low dose per pulse, hence, small value of u, the difference among the three models will be negligible and they are approximately equal to eq. 2.44. For high dose per pulse, hence, larger values of u, the results of k_s obtained from different models will be different from each other and from eq. 2.44.

3.3.6. Laitano's approach

Laitano et al. performed the TVA method on the basis of the Boag's modified recombination models which described in section 3.3.5 previously. This method requires the determination of the appropriate values of u. For this purpose, at different dose-per-pulse values, a set of repeated measurements of charge values Q_1 and Q_2, corresponding to the pair of chamber voltages $V_1 = +300$ V and $V_2 = +100$ V were performed. Then three equations corresponding to the expressions 3.11, 3.12 and 3.13 regarding the charge ratio Q_1/Q_2 according to the TVA

technique were solved for the factor u by iterative methods (see appendix B). This approach also requires the calculation of the free-electron fraction p based on the experimental data as

$$p = \frac{\omega\tau}{d}\left(1 - e - \frac{d}{\omega\tau}\right), \tag{3.14}$$

where τ(s) is the life time (mean time until attachment to the collecting electrode), ω (m/s) is the drift velocity of the free electrons in the chamber gas, and d is the chamber's electrode separation [11]. The quantity p does not depend on dose-per-pulse but on the chamber's operational conditions through d, τ and ω. τ and ω are both dependent on the electric field strength and the type of gas of the ion chamber. The coefficients τ and ω were determined as described by Laitano et al. [11]. The formalism to calculate these two coefficients was obtained by fitting to experimental data published by Hochhäuser et al. and is presented in appendix A [12]. The values of ω, τ and p, which were used in this work, are reported in table 3.2.

Table 3.2.: Chamber characteristics for the Advanced Markus parallel-plate ionization chamber and estimate of free-electron fraction p, according to eq. (50). V refers to the chamber's operating voltage.

V_1 (V)	V_2 (V)	λ_1	λ_2	p_1	p_2	$\tau_1\left(\times 10^{-8}\right)$ (s)	$\tau_2\left(\times 10^{-8}\right)$ (s)	$w_1\left(\times 10^{4}\right)$ $\left(ms^{-1}\right)$	$w_2\left(\times 10^{4}\right)$ $\left(ms^{-1}\right)$
300	100	0.443	0.147	0.690	0.273	5.34	2.11	2.40	1.33
400	100	0.519	0.147	0.769	0.273	6.57	2.11	2.80	1.33

3.3.7. Comparison of different methods

To compare the different methods described above, the ratios $(k_s)'_{th}/(k_s)^{ref}_{w}$) were determined, where the $(k_s)'_{th}$ factor represents the ion recombination correction factors obtained from the different methods $\left((k_s)^{B'}_{th}, (k_s)^{B''}_{th}, (k_s)^{B'''}_{th}\ and\ (k_s)^{TVA}_{th}\right)$. Additionally, the average deviation between $(k_s)'_{th}$ and $(k_s)^{ref}_{w}$ was calculated as the mean value of the quantities $\left((k_s)'_{th} / (k_s)^{ref}_{w} - 1\right)$.

3.4. Monte Carlo simulation and commissioning of the NOVAC7

3.4.1. EGSnrc Monte Carlo system

The EGSnrc is a Monte Carlo based system for simulation of electrons and photons with energies ranging from a few keV up to hundreds of GeV. This package which has been developed at National Research Council of Canada (NRCC) is the latest version of EGS (Electron-Gamma Shower) series of Monte Carlo codes and has significant advantages compared to its predecessor code, EGS4. Some relevant improvements compared to EGS4 are listed below:

(a) A new multiple scattering theory is employed which switches from single scattering approach for short steps (near material boundaries) to multiple scattering method for long CH steps.

(b) Spin effects are taken into account in the sampling of cross sections.

(c) Bremsstrahlung angular sampling has been modified to be more accurate.

(d) Atomic relaxations after Compton and photoelectric events are simulated.

(e) Cross section database has been optimized to produce radiative stopping powers more precisely.

As previously mentioned, EGSnrc uses PRESTA-II (Parameter Reduced Electron-Step Transport Algorithm) electron-transport algorithm which adjusts the optimum step-size automatically. By employing this technique, the PLC and TD (see section 2.5) for both low and high energies are sampled accurately and meanwhile the simulation time becomes shorter. The cross section database for electron and photon interactions used in EGSnrc user codes is provided by PEGS4 algorithm. Specifically, this program produces data tables (considering material composition, mass density and energy range), in which electron collision and radiative stopping powers and photon attenuation coefficient are obtained using experimental and calculated data [20].

EGSnrc employs Møller scattering theory to model hard electron-electron collisions and employs the screened Rutherford elastic model based on Mott scattering theory to simulate electron-nucleus collisions. More details are available in [20]. Elastic scattering is not fully simulated but the cumulative effect is modeled during an electron's condensed history step, as explained in section 2.5. The simulation of photoelectric effect in EGSnrc is sampled using PEGS program

which is a preprocessor of EGS system (see section 2.4.6 for details). More details can also be found in the EGSnrc user manual [20]. The system employs the total Klein-Nishina cross section to model Compton effect. The Klein-Nishina cross section does not take into account the binding energy of the electron and simulate it as being at rest. The equation for the Klein-Nishina cross section is given as:

$$\frac{d\sigma}{dcos\theta} = \pi r_0^2 Z X_{KN}, \tag{3.15}$$

where θ is the polar angle between the scattered and incoming photon, Z is the atomic number, and X_{KN} is a term associated with the energy of photon. More details are explained in the user manual of the EGSnrc [20]. EGSnrc applies a total pair + triplet cross section data to sample distances to subsequent pair production collisions instead of modelling each interaction explicitly. This cross section data is extracted from a scattering theory which is based on the extreme relativistic first Born approximation which is described in detail in literature [20]. The EGSnrc system consists of several useful user codes including BEAMnrc, DOSXYZnrc, SPRRZnrc and BEAMdp which are demonstrated briefly in following sections [20, 65, 67, 82].

3.4.1.1. BEAMnrc

The BEAMnrc user code is built on the EGSnrc Monte Carlo system and is developed to simulate radiotherapy sources including linacs [26].

The modeling of linear accelerators within BEAMnrc is achieved using so-called Component Modules (CMs). In other words, each part of the accelerator or source (e.g. target, collimator, monitor chambers, etc) is considered to be a single independent CM. Each CM can be used several times and is connected to the remaining system in certain ways. Detailed explanation about the various types of CMs is available in the BEAMnrc user manual [26]. The characterization of each CM is implemented, based on the detailed radiation head data provided by the manufacturer. Subsequently, an accelerator is built by adding previously generated CMs.

The user has the possibility to influence the physics modelling of the accelerator through changing so-called transport parameters. For example, the user may turn on/off specific interactions (e.g. atomic relaxation, coherent scattering, etc.), set the values of input parameters (cut-off energies, threshold energies, etc.) and/or select the transport algorithm (e.g. PRESTA,

PRESTA-II, etc.). Such parameters may considerably affect a simulation result. For example, when a particle's energy falls below the cut-off energy (E_{cut} or P_{cut}), it is no longer followed and its energy is deposited locally. This means that, increasing the value of this parameter makes the simulation time shorter but decreases the accuracy of the results and vice versa.

Another important feature of BEAMnrc is the likelihood of generating so-called phase space files (PSFs) in arbitrary planes within the simulated geometry, referred to as "scoring planes". These files (PSFs) consist of all essential parameters (position, direction, charge, energy, etc.) of particles transported through the desired scoring plane. A certain PSF file can then be employed as the source to obtain different dosimetric parameters within other user codes such as DOSXYZnrc, SPRRZnrc and BEAMdp.

A subsequent remarkable advantage of BEAMnrc is that it allows, through LATCH variable, to specify the locations where the particles have been created or have interacted. LATCH is a 32-bit variable to track the history of particles and its output is employed to different user codes (e.g. BEAMnrc, DOSXYZnrc, BEAMdp, etc) in order to separate the contribution of various components (e.g. adapters, collimators, etc) and different types of particles (e.g. scattered electrons, contaminant photons, etc) to the several dosimetric parameters (e.g. PDD, profile, energy fluence, etc). In this study, mapping from geometric regions of the simulated accelerator to bits was performed. In this option, bits 1 to 23 of LATCH record where a charged particle has been or where a photon has interacted and bits 24 - 28 are used to record the region of origin of a secondary particle. LATCH bits are associated with regions/components of an accelerator using the IREGION to BIT input parameter. The procedure of modeling a linac in BEAMnrc has been comprehensively explained in the literature and the BEAMnrc user manual [26].

3.4.1.2. DOSXYZnrc

DOSXYZnrc is one of the EGSnrc user codes developed in order to calculate three dimensional absorbed dose distributions in phantoms [27]. This system models the transport of electrons and photons and scores the dose in voxels consisting of specific physical density and materials. The dimensions of voxels are variable in all three (x, y and z) directions and the density and material composition in every voxel may change. The user can choose among variety of source types such as monoenergetic, parallel beam or phase-space file generated during BEAMnrc simulation. The output of this code is normalized per incident history and is a three dimensional dose distribution including the uncertainties.

With full phase space file as an input source, the user is able to employ an optional parameter referred to as "NRCYCL" to recycle the particles of the PSF and use them multiple times for the simulation. Recycling incident particles NRCYCL times means to employ a total of NRCYCL + 1 times the particles and consequently to increase the number of particles simulated in a run. Therefore, this option reduces the calculation time. However, applying this parameter requires caution because recycling may cause correlations between particles in the PSF and as a result it may increase the statistical uncertainty of the dose [27].

3.4.2. Measurements

Relative absorbed dose measurements, i.e. percentage depth doses (PDDs) and off-axis profiles (OAPs), were carried out using radiochromic films (Gafchromic (EBT2), in a small water phantom as described in section 3.3.1. Film calibration was performed following the previously mentioned procedure (see subsection 3.3.1). The result from film dosimetry is stated to be directly related to the absorbed dose to water. The uncertainty in the film positioning was less than 0.1 mm and PDDs and OAPs were acquired with a spatial resolution of 72 dpi corresponding to a pixel size of $0.35 \times 0.35\,\mathrm{mm}^2$, and saved in TIFF format. For all energies, the PDDs were acquired along the clinical axis, i.e. the axis perpendicular to the water surface going through the centre of the area (circular for a flat applicator, elliptic for bevelled ones) intercepted by the projection of the applicator. The OAPs were measured at the depth of 80% and 90% dose value of the relative depth dose curve. In all measurements, there was a 7 mm air gap between the end of the applicator and the water surface. Measurements were carried out at SSD of 800 mm.

3.4.3. Monte Carlo simulation

The radiation head simulation of the NOVAC7 was performed with the EGSnrc user code BEAMnrc [26]. The simulation geometry includes: exit window, monitor unit chambers, adaptor and applicator. A sectional drawing of the components and their arrangement is provided in fig. 3.8. The EGSnrc transport parameters were taken as BCA = EXACT (Boundary Crossing Algorithm), electron step algorithm = PRESTA - II with electron step size (ESTEPE) = 0.01. It should be noted that no variance reduction technique was used. The water phantom component module of the BEAMnrc user code was used to calculate the percentage depth dose directly without using the phase space data [26]. The dimensions of the bins along the z-axis in the phantom were circles with a 5 mm radius and a thickness of 1 mm. For the simulation transport

and particle production, threshold energy of $E_{cut} = 0.521\,\text{MeV}$ for electrons and $P_{cut} = 0.01\,\text{MeV}$ for photons was used to obtain good straggling [26]. The terms AE and AP are used in EGSnrc instead of E_c and k_c introduced in section 2.5. E_{cut} and P_{cut} were introduced in subsection 2.4.6.

For each calculation a PSF file (see subsection 3.4.1.1) was generated and was used as particle source in the user code DOSXYZnrc to calculate OAPs within the water phantom [27]. The water phantom dimensions were $300 \times 300 \times 150\,\text{mm}^3$ and the voxel size was $5 \times 5 \times 1\,\text{mm}^3$. In this user code, the transport and particle production threshold energy was set to $E_{cut} = 0.521\,\text{MeV}$ for electrons and $P_{cut} = 0.01\,\text{MeV}$ for photons to achieve more accurate dose in small voxels [27]. The simulation of $10^7$to 10^8 particles was necessary in order to get a statistical uncertainty of calculated dose values of about $0.5-1\%$ in the region between the surface and the depth corresponding to 10% of the maximum dose. The CPU time to calculate a depth dose curve was in the range of 24 h.

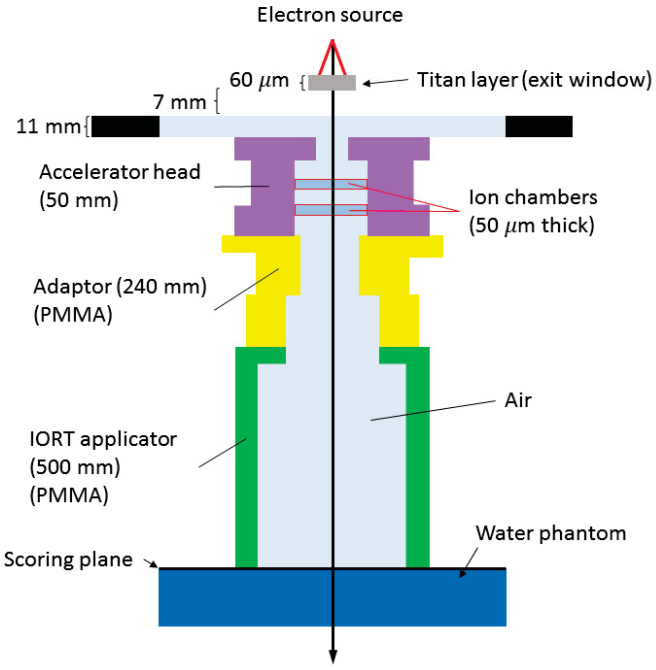

Figure 3.8.: Radiation head components of the NOVAC7: Exit window, ion chambers and collimation part are three main components of this accelerator. The simulated water phantom is for calculation of PDD. An accurate modelling of such components is necessary for achievement of a reliable dosimetric calculations [22].

3.4.4. Linac commissioning

An accurate method to find the spectrum of the electron beam impinging on the scattering foil is to vary iteratively some parameters that characterize the spectrum shape. These parameters have been determined by fitting the Monte Carlo results to measurements. Specifically measured PDDs and OAPs were used to obtain electron energy characteristics. Accordingly, the initial energy spectrum was supposed to be Gaussian-shaped. For reaching the measured R_{50}, the most probable energy of Gaussian distribution was varied iteratively in small steps (0.05 MeV) around the appropriate nominal energies of the NOVAC7 until the calculated and measured values of R_{50} had been matched. Similarly, to obtain the proper dose gradient of PDD, the width (FWHM) of Gaussian spectrum was changed iteratively until an acceptable agreement between calculated and measured data was achieved.

Furthermore, source geometry and beam divergence were optimized to meet the agreement criteria between simulation and experimental data of off-axis profiles. The agreement criteria were fulfilled following two independent methods. First, the iteration was performed as long as an agreement of ±3 mm/3% (according to data provided by the manufacturer) was established. Second, the root mean square (RMS) and mean deviation between calculation and measured data were evaluated after each simulation in order to obtain conformity better than 2%. The Monte Carlo model evaluation was made via the two above mentioned methods in order to assure an accurate benchmarking.

3.5. Stopping power ratios and output factors

3.5.1. SPRRZnrc

The SPRRZ code is used to determine the Spencer–Attix mass restricted collision stopping-power ratios (see subsection 2.7.5). The calculation is performed by cylindrical geometries, where each region is defined by a thickness, an internal and an external radius. Each calculation region is assigned a density and a medium. A full phase space file was utilized as the particle source in this user code. The $s^{\Delta}_{w,air}(z)$ values were calculated by obtaining the absorbed dose in the medium and the cavity, but for a modeling in which the cavity is filled with the transport medium instead of the detector medium. The deposited energy in the detector medium is then calculated by its multiplication in the transport medium, at the location of the cavity, with stopping power ratios. Depending on the type of energy deposition modes (α, γ, δ or β, described below) and

the particles energy, restricted or unrestricted stopping power rations are taken into account. Energy deposition in SPRRZnrc technique is considered to include four discrete modes referred to as "α, γ, δ and β" which are explained in table 3.3 and fig. 3.9 [81, 97]. For α events, restricted stopping powers at the mid-point energy of the particle step are used. The β particles are ignored in the $s^{\Delta}_{w,air}(z)$ calculation because their energy is absorbed on the spot independent of the medium. For δ events, the unrestricted stopping powers ($s_{w,air}(z)$) are used. Energy deposition for electrons in γ mode is treated in two separate components.

Table 3.3.: The energy deposition categories considered in SPRRZnrc user code of EGSnrc Monte Carlo system. They are distinguished based on their initial and final enegy along a step.

Category	Description
α	Deposition mode for electrons in a step with a total energy larger than Δ (E_{cut}, see section 2.5).
γ	Deposition mode for electrons initiate a step with an energy larger than Δ and end the step with an energy less than Δ.
δ	Deposition mode for electrons and photons which are terminated since their energy is less than cutoffs AE or AP.
β	A mode for electrons and photons which their kinetic energy is initially lower than cutoffs AE or AP.

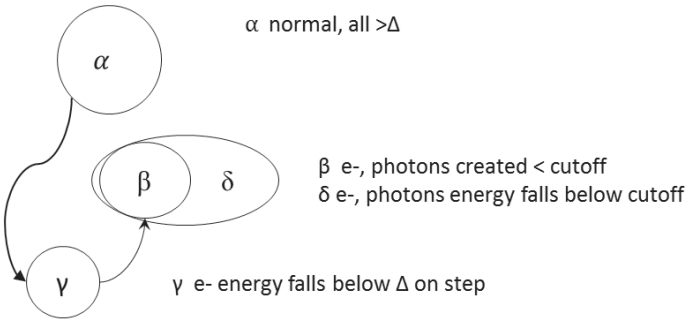

Figure 3.9.: Modes of energy deposition ragarded in SPRRZnrc. In α events energy is deposited by electrons in a step with the energy absolutely higer than Δ. The γ events are those in which the electron begins a step with its energy above Δ and ends with an energy lower than Δ. The δ events imply to all those events in which an electron or photon are being terminated because their energy is below the cutoffs AE or AP. This embodies a subset of β events formed by electrons and photons which are produced with their energy initially lower than AE or AP. Reproduced from [81, 97].

The component with energy greater than Δ is simulated as a α mode, whereas the component with the energy less than Δ is transported as an δ event. The stopping power ratios are then calculated as the ratio of summed dose to the cavity volume filled with the transport medium and the calculated dose to the detector medium.

3.5.2. Calculation of output factors

Output factors (OFs) were simulated and compared with measurement. The PDDs were calculated according to the procedure described in subsection 3.4.3. The OFs for the nominal energy E are given by $\frac{D_w(E,D,z_{max})}{D_w(E,100,z_{max})}$, where $D_w(E, D, z_{max})$ is the absorbed dose in water at depth of dose maximum (z_{max}) for the applicator with diameter D along the clinical axis of the applicator and $D_w(E, 100, z_{max})$ is the dose for the reference applicator with 100 mm diameter. The 9 MeV energy beam with the 100 mm applicator will be addressed as the reference beam throughout this manuscript. For the OF calculation, the absorbed dose values were normalized to the number of electrons incident on the exit window of the accelerator.

3.5.3. Measurement of output factors

Electron beams with 3, 5, 7 and 9 MeV nominal energies generated by the NOVAC7 linac were investigated. The OFs measurement was performed in a 3D water phantom (iba, Blue Phantom) which was connected to OmniPro-Accept 6.4 software for data acquisition and evaluation. The chamber was positioned within the phantom at isocenter. The isocenter was defined as the centre of the applicator cross section on the surface of water. The chamber was connected to a Unidose webline (type 10021-003, PTW/Freiburg) digital electrometer and was irradiated with 500 MU for each beam set-up. The operating voltage was set at +300 V. All measurements were performed at SSD 800 mm. The effective point of measurement of the pin-point chamber was regarded in all measurement set-ups. The percentage depth ionization (PDI) curves were converted in PDD plots using the water-to-air stopping power ratios $s_{w,air}$ according to the IAEA TRS-398 protocol [7]. These $s_{w,air}$ values were experimentally fitted by Burns et al. to a data set calculated by Ding et al. using Monte Carlo simulations of realistic clinical electron beams [19, 98] . Using ionization chambers requires considering different correction factors applied to the measured signal. With regards to this, the correction factors for ion recombination and the polarity effect may change between the field of interest and the reference field. The influence of these correction factors was taken into account for the OF determination.

3.5.4. Calculation of stopping power ratios

The phase-space files at the phantom surface obtained for the IOERT were also used as source inputs for the EGSnrc/SPRRZnrc code in order to calculate mass restricted Spencer–Attix stopping power ratios of water-to-air, $s^{\Delta}_{w,air}(z)$ [97]. This code exploits an on-the-fly technique for scoring, which has been proved to deliver the identical results as the more traditional methods of first calculating the fluence spectrum (the code has been benchmarked by Kosunen and Rogers [99] and used extensively by other authors [19]). A detailed description of this user code is given in section 3.5.1.

The $s^{\Delta}_{w,air}(z)$ values were calculated along the central axis of the beam in cylindrical regions with 1 mm thickness and 10 mm radius. They were obtained for 3, 5, 7 and 9 MeV on the water surface, at the reference depth z_{ref} and as a function of depth in a water phantom. In all simulations, the energy cut-offs for particle transport were set to $E_{cut} = \mathrm{AE} = 0.521\,\mathrm{MeV}$ (kinetic energy plus rest mass) and $P_{cut} = \mathrm{AP} = 0.010\,\mathrm{MeV}$. The total number of source particles in phase space file was $5\,.\,10^6$, $4\,.\,10^6$, $7\,.\,10^6$ and $9\,.\,10^6$ for 3, 5, 7 and 9 MeV, respectively. The statistical uncertainty of the results was less than 1%. The results were compared with those obtained according to the TRS-398 dosimetry protocol [7].

3.6. Scatter and contamination analysis

3.6.1. BEAMDPnrc

BEAMDPnrc is a data processing code in order to analyze phase space files generated from BEAMnrc [25]. In this study, phase space files created by LATCH option were used to calculate the contribution of total, direct and scattered electrons together with contaminant photons to energy fluence, electron fleuece, PDD, profile, mean energy and angular distributions. Using a code-specific graphical user interface (GUI), it is determined which parameter should be calculated. In the case of planar energy fluence for instance, the user can choose to calculate the desired parameter between circular, square or rectangular fields with arbitrary dimension. Subsequently, the corresponding LATCH option together with the certain phase space file is selected. Finally, a name for the output file, type of the graph (point or histogram) and type of the fluence (estimated real fluence or planar fluence) are chosen and the calculation can be started [25].

3.6.2. Calculation

The phase-space file (see subsection 3.4.1.1) generated by BEAMnrc including the LATCH variable, for specific energy and applicator, was used by the BEAMDP user code described in previous subsection (see subsection 3.6.1). To calculate above mentioned parameters, some input data are required, for example particle type, the diameter of calculation region, LATCH options and energy range should be selected for each specific calculation. The calculations were performed for different applicator diameters. For the analysis of the energy fluence and angular distribution, the number of energy bins was set to 100 and the value of 0.1 MeV bin width for energy distribution was employed.

For determination of planar fluence and mean energy vs position, a 100 mm circular field with 100 equal circular ring bins was chosen which means the planar fluence scoring field was larger than the treatment field. It is worth noticing that the equal bin area ensures less statistical fluctuation of planar fluence from bin to bin. Furthermore, circular fields are appropriate for beams confined by the NOVAC7 circular components such as monitoring chambers and applicators. The selection of input parameters was made according to EGSnrc user manual recommendations [50]. Moreover, BEAMnrc user code was used in this chapter to calculate the depth dose distribution of different components [26].

A significant advantage of the BEAMnrc code (as described in detail in section 3.4.1.1) is that it allows to track individual particle's history using LATCH option which is also explained in that section. Using the LATCH technique, it was therefore possible to separate the contribution of different components (e.g. adapter, applicator, etc.) to obtain the dosimetric characteristics of the NOVAC7 electron beams (e.g. PDDs). As the subsequent tool, DOSXYZnrc (see section 3.4.1.2) was employed to calculate the OAPs at water surface (z_0), depth at dose maximum (z_{max}) and depth of 50% isodose (R_{50}) in water phantom. For this purpose, the phase-space files at the phantom surface were used as an input source to the DOSXYZnrc user code in order to simulate the off-axis dose distributions.

4. Results

4.1. Ion recombination correction factor

4.1.1. Dose rate versus applicator diameter

Figure 4.1 shows the measured dose-rate values as a function of the applicator diameter for the four different electron energies of the NOVAC7 system. As can be seen, for 7 and 9 MeV electrons the dose-per-pulse value measured at z_{ref} increased almost linearly (with a gradient of about 0.2 mGy/pulse mm) as the applicator diameter decreased, which is consistent with results obtained in previous studies [15, 22]. However, for 3 and 5 MeV electron beams the dose-per-pulse values measured at z_{ref} were almost independent of the applicator diameter (5.1 and 12 mGy/pulse for 3 and 5 MeV, respectively). This is also in good agreement with results given in the literature [17].

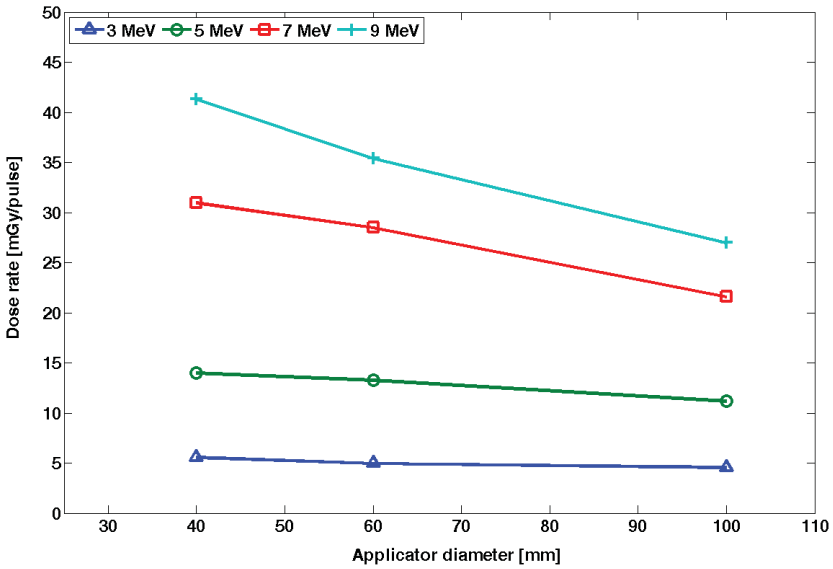

Figure 4.1.: Dose-rate values as a function of applicator diameter for different energies.

4.1.2. Comparison of ion recombination correction factors

Data obtained in previous studies [11, 15] using different chambers within a specific dose-per-pulse range indicated that the acceptability of k_s values resulting from Boag's expressions and based on Laitano's approach are model-dependent. Furthermore, according to Laitano et al., k_s values resulting from the TRS-398 method deviate about 8% from reference values for the Markus chamber at 40 mGy/pulse [11]. In the present study, ion recombination correction factors obtained from equations (3.11), (3.12), (3.13) and from the TRS-398 method were compared against the recombination correction factor determined by a reference dosimeter ($(k_s)_w^{ref}$). Figures 4.2(a)-4.2(d) illustrate the $(k_s)'_{th}/(k_s)_w^{ref}$ values for different dose-per-pulse values.

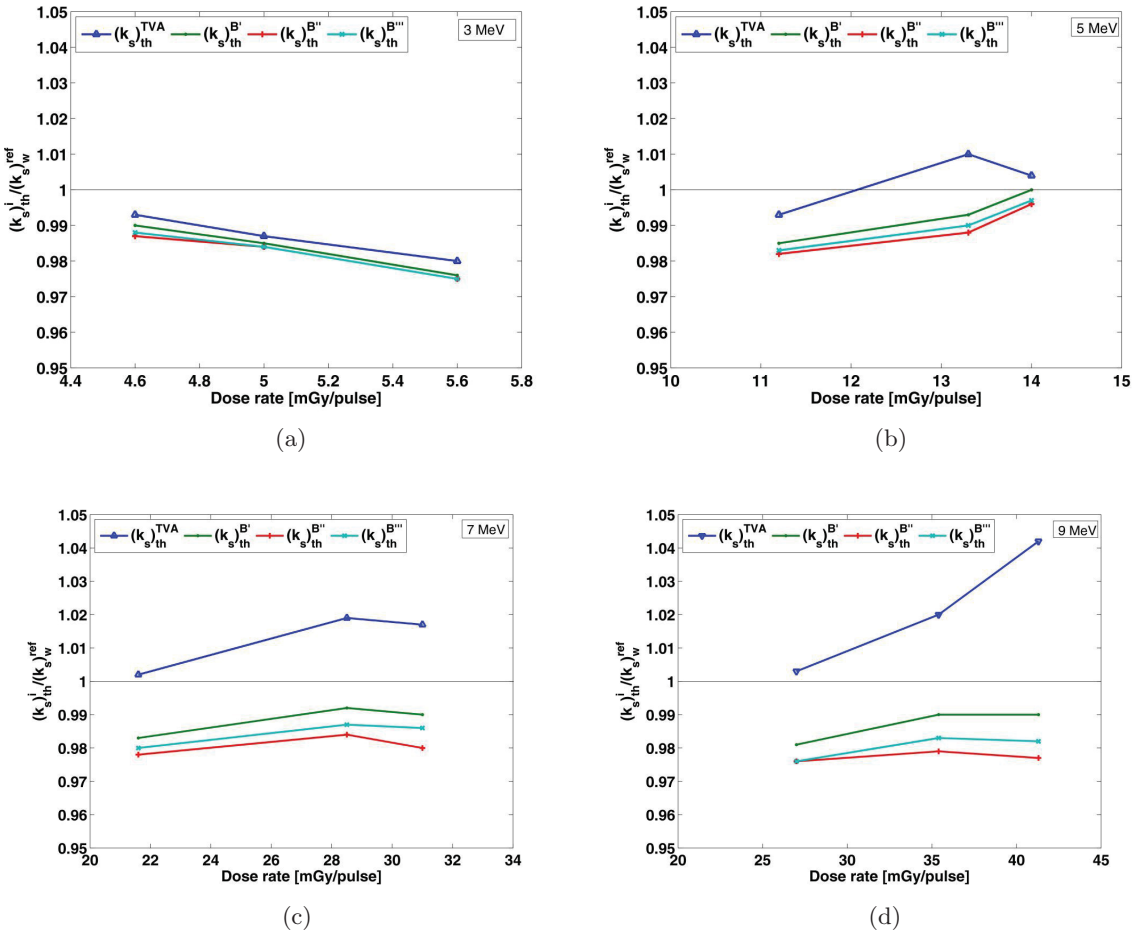

Figure 4.2.: The $(k_s)'_{th}\,/\,(k_s)_w^{ref}$ ratios as a function of dose rate (mGy/pulse) for the Advanced Markus chamber for 3, 5, 7 and 9 MeV electron beams, respectively. $(k_s)'_{th}$ values refer to the ion recombination correction factors related to Boag's theoretical models. The data denoted by triangles are the $(k_s)_{th}^{TVA}\,/\,(k_s)_w^{ref}$ ratios relevant to the conventional two-voltage-analysis method not including the impact of free electrons. The operating voltage was $V_1 = 300$ V, the uncertainty on the $(k_s)'_{th}\,/\,(k_s)_w^{ref}$ values is 3%.

Table 4.1.: The values of ion recombination correction factors obtained applying different methods at different dose-per-pulse values using Gafchromic films and Advanced Markus parallel-plate ionization chamber.

Applicator (mm)	Energy (MeV)	Dose rate (mGy/pulse)	$(k_s)_w^{ref}$	$(k_s)_{th}^{TVA}$	$(k_s)_{th}^{B'}$	$(k_s)_{th}^{B''}$	$(k_s)_{th}^{B'''}$
40	3	4.6	1.014	1.007	1.003	1.001	1.002
100	3	5	1.017	1.004	1.002	1.001	1.001
60	3	5.6	1.027	1.007	1.002	1.001	1.001
100	5	11.2	1.020	1.013	1.005	1.002	1.003
40	5	13.3	1.015	1.025	1.008	1.003	1.005
60	5	14	1.006	1.010	1.006	1.002	1.003
100	7	21.6	1.027	1.029	1.010	1.004	1.006
100	9	27	1.032	1.035	1.012	1.007	1.007
60	7	28.5	1.021	1.040	1.013	1.005	1.008
40	7	31	1.023	1.040	1.014	1.005	1.009
60	9	35.4	1.027	1.048	1.015	1.006	1.010
40	9	41.3	1.034	1.078	1.024	1.010	1.015

The absolute values of k_s obtained applying the above-mentioned approaches at different dose-per-pulse values are summarized in table 4.1. According to figures 4.2(a)-4.2(d), the average deviation between k_s values calculated from different methods and the reference k_s values is within the tolerance level (3%). However, at a higher dose-rate value of about 42 mGy/pulse $(k_s)_{th}^{TVA}$ deviates from $(k_s)_w^{ref}$ by 4.2%, which is higher than the tolerance level. Although the deviation of k_s values obtained from Laitano's approach from $(k_s)_w^{ref}$ becomes larger with increasing dose-per-pulse values, it does not exceed the tolerance limit as shown in table 4.1 and figures 4.2(a)-4.2(d).

4.1.3. k_s comparison for different chamber voltages

Table 4.2 shows the ratio $(k_s)_{th}^{'}/(k_s)_w^{ref}$ obtained for different voltages (300 V and 400 V) at the lowest dose rate of 4.6 mGy/pulse and the highest dose rate of 41.3 mGy/pulse. The data denoted by $(k_s)_{th}^{TVA}\,/\,(k_s)_w^{ref}$ are relevant for the conventional two-voltage-analysis method not including the impact of free electrons. The results showed that both at a low dose rate (4.6 mGy/pulse) and at a high dose rate (41.3 mGy/pulse), for a chamber with a small spacing such as the Advanced Markus chamber ($d = 1$ mm) the different expressions for $k_s((k_s)_{th}^{TVA}, (k_s)_{th'}^{B'}, (k_s)_{th}^{B''}\, and\, (k_s)_{th}^{B'''})$ tended to give similar results as the chamber voltage is increased. A similar trend was reported

in literature for the Exradin A11 chamber [11].

Table 4.2.: The ratios $(k_s)'_{th} / (k_s)^{ref}_w$ as a function of applied chamber voltage (300 V and 400 V) at the lowest dose rate (4.6 mGy/pulse) and the highest dose rate (41.3 mGy/pulse) for the Advanced Markus chamber. $(k_s)'_{th}$ values refer to the ion recombination correction factor related to Boag's theoretical models $(k_s)^{B'}_{th}$,$(k_s)^{B''}_{th}$ and $(k_s)^{B'''}_{th}$. The uncertainty on the $(k_s)'_{th} / (k_s)^{ref}_w$ values is 3%.

	4.6 mGy/pulse		41.3 mGy/pulse	
$(k_s)'_{th} / (k_s)^{ref}_w$	300V	400V	300V	400V
$(k_s)^{TVA}_{th} / (k_s)^{ref}_w$	0.993	0.994	1.042	1.024
$(k_s)^{B'}_{th} / (k_s)^{ref}_w$	0.989	0.993	0.990	1.011
$(k_s)^{B''}_{th} / (k_s)^{ref}_w$	0.987	0.991	0.980	0.988
$(k_s)^{B'''}_{th} / (k_s)^{ref}_w$	0.988	0.992	0.982	0.960

4.1.4. Jaffé diagram

Finally, the applicability of the Jaffé diagram for k_s determination at the 27 mGy/pulse was investigated. This dose-per-pulse value was produced by 9 MeV electrons and the 100 mm applicator which was considered as the reference condition. Figure 4.3 illustrates the relation between normalized measured values, M_s/M_V and normalized chamber's operating voltages V_0/V where M_s is the chamber reading at the calibration voltage (V_0) and M_V is the chamber reading at the given voltage (V).

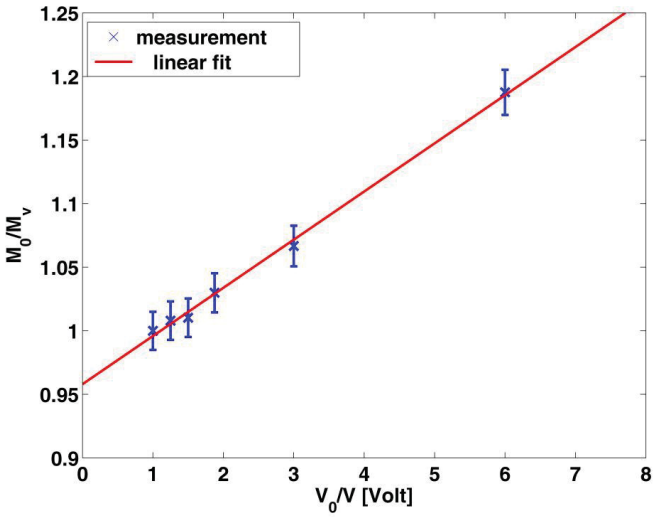

Figure 4.3.: Jaffé plot for the Advanced Markus chamber. The normalized measured values, M_s/M_V, are plotted against the normalized chamber's operating voltages V_0/V. M_s is the chamber reading at the calibration voltage (V_0) and M_V is the chamber reading at the given voltage (V). The data are corrected for polarity effect (k_p), temperature, and air pressure ($k_{T,P}$). The solid line is a linear fit of the data. This curve is obtained for the 27 mGy/pulse produced by 9 MeV electrons and a 100 mm applicator.

The data are corrected for polarity effect (k_p), temperature, and air pressure ($k_{T,P}$). As can be seen, there is an almost linear relationship in the range from 50 V up to 300 V. The resulting $(k_s)_{th}^{jaff}$ value deviates from the reference value ($(k_s)_w^{ref}$) by +1.2%.

4.1.5. Uncertainty analysis

According to Laitano et al. the combined uncertainty of the $(k_s)_{th}^{'}$ values at 70 mGy/pulse is 2% [11]. Sources of uncertainty were the factors ω, τ and the chamber spacing d. As a result of the combined uncertainty of optical density ($\Delta = 1\%$), polarity effect ($\Delta = 0.6\%$) and calibration ($\Delta = 1\%$), the uncertainty of the $D_{w,Gaf}$ values was calculated as 1.5%. The optical density (OD) uncertainty of 1.0% at 1 Gy was considered based on the analysis performed by Martisikova et al., the calibration uncertainty of 1.0% was accounted for by the determination of the beam quality correction factor based on the TRS-398 dosimetry protocol [91]. The uncertainty of $D_w^{'}$ was 1.5%. This is the square product of $\Delta = \pm 0.6\%$ on the calibration factor, $N_{D,w}$, based on the TRS-398 protocol, $\Delta = \pm 1.1\%$ on the beam quality correction factor, $k_{Q,Q'}$, based on the manufacturer's calibration sheet (Co-60 as the calibration quality), and $\Delta = 0.8\%$ for the polarity effect. Resulting from eq. (3.4), the combined uncertainty for $(k_s)_w^{ref}$ was estimated as 2.1%. Combining the Δ =2.0% on $(k_s)_{th}^{'}$ with the uncertainty of $(k_s)_w^{ref}$ led to an overall uncertainty of almost 3% for the $(k_s)_{th}^{'}/(k_s)_w^{ref}$ ratios.

4.2. Monte Carlo simulation and commissioning of the NOVAC7

The commissioning was performed for the biggest available applicator (100 mm, 0°), which is the reference field size in this study. The values of the most probable energy and the mean energy of the initial electron beams used as input into the Monte Carlo simulation are reported in table 4.3. The results were further evaluated for the other applicators. The electron source, was modeled as an isotropic point source with a primary Gaussian distribution on z axis. The FWHM of the curve of average of 22% provided the best match with the measured PDD and profile data. In figures 4.4(a-d) the calculated and measured PDDs obtained with the IOERT applicator of 100 mm diameter are reported for all nominal energies. Similar results have been obtained for the applicators with diameters of 40, 60 and 80 mm. For achieving the measured R_{50}, the most probable energy was varied in steps of 0.05 MeV around the appropriate nominal energies and the calculated PDD was compared with measured PDD.

Table 4.3.: The characteristics of the energy spectra for all energies. E_p is the most probable energy, E_{mean} refers to the mean energy and FWHM is the full-width-at-half-maximum of the energy spectrum.

Nominal energy (MeV)	$E_{p,0}$ (MeV)	E_{mean} (MeV)	$FWHM$ (MeV)
3	4.17	3.99	1.14
5	5.00	5.02	1.74
7	7.50	6.95	1.66
9	9.00	8.70	2.01

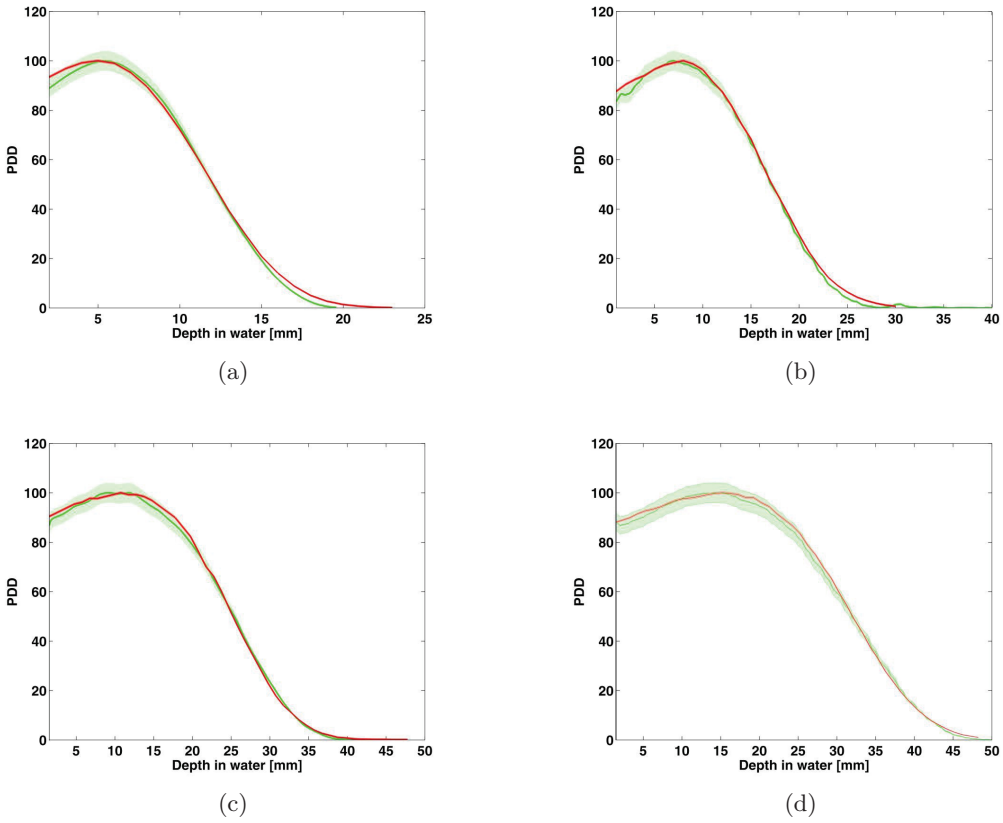

Figure 4.4.: Comparison of measured (green line, Gafchromic) and simulated (red line, Monte Carlo) PDDs for all electron beam energies (a) 3 MeV; (b) 5 MeV; (c) 7 MeV and (d) 9 MeV as a function of depth (mm) in water. The shaded areas around both lines represent the uncertainity of data.

In order to gain the proper dose gradient, the width of Gaussian distribution was varied iteratively until the best agreement between calculation and measured data was fulfilled. Similar results were concluded for other applicators using the same electron spectrum file as beam source to BEAMnrc. Table 4.4 shows the parameterised data of the PDDs. In this table, calculated R_{max}, R_{80}, R_{50} and R_p were compared with the measured values.

For all nominal energies, the calculated PDDs agree within ±2% or ±1 mm with those measured values. In all cases, the local percentage dose and distance to agreement were below the required thresholds. The criteria of 3 % local percentage dose difference and 3 mm distance to agreement were fulfilled. The build-up region could also be simulated and predicted accurately. As it can be seen from fig. 4.4, the most obvious deviation between measurements and calculated data is observed near the water surface. The low part of energy spectrum is the main reason of reproducing this effect. The effect of scattered particles on the surface dose plays a pronounced role. Another source of deviation is the increase of difference at larger depth in water for small energies and small applicators.

Table 4.4.: Parameterised data for the PDDs comparison between BEAMnrc calculation (calc.) and radiochromic (EBT2) film dosimetry (meas.). R_{max}, R_{80}, R_{50}, R_p and the difference between two methods (diff.) are reported in mm.

	Energy (MeV)	3	5	7	9
R_{max}	meas.	5.0	7.0	11.0	14.0
	cal.	5.5	8.0	11.5	15.0
	diff.	0.5	1.0	0.5	1.0
R_{80}	meas.	9.5	13.2	20.0	25.0
	cal.	9.6	13.1	20.0	26.0
	diff.	0.1	0.1	0.0	1.0
R_{50}	meas.	12.4	17.1	25.0	32.0
	cal.	12.5	17.0	25.0	32.0
	diff.	0.1	0.1	0.0	0.0
R_p	meas.	13.5	19.4	29.5	38.3
	cal.	13.6	19.7	29.5	38.8
	diff.	0.1	0.1	0.0	0.5

Another check for the accelerator modeling was that the mean energy of the primary electrons and the width of Gaussian distribution which yielded the best agreement in terms of RMS deviations and mean deviations to the measured depth dose values were determined. The RMS and mean deviation of all measured points compared to calculated points are shown in table 4.5. The RMS values of maximum 2% for all energies were achieved expect for 5 MeV. For this energy, the RMS value increased slightly in the practical range. The mean deviation was less than 1% for nearly all energies.

Figures 4.5(a-d) show the profile comparison between calculation and measurement of 80% depth of dose distribution. The radius and divergence of the initial electron beam, even if not influential on the PDD curves, were found beneficial in the iterative process and in modifying the off-axis distributions of the electron beams. The optimization of the accelerator modeling was gained with an initial electron beam with 1 mm radius and 1° divergence at the exit vacuum window and 114.5 mm distance from the first component module. As illustrated in fig. 4.5, a good match between calculated and experimental transverse dose profiles for all of the nominal energies was obtained with the chosen geometry. As it can be seen, the ±3% agreement with the experimental data was achieved all along the off-axis profiles except in the vicinity of the penumbra region which includes a less important modeling.

Table 4.5.: The RMS (Root Mean Square) and the Mean (mean deviation) values resulted from comparing PDDs calculated by BEAMnrc and those measured by radiochromic film for all energies and typical applicators (diam. 40 - 100 mm). The values are reported in percent.

Energy (MeV)	3		5		7		9	
App. (mm)	RMS	Mean	RMS	Mean	RMS	Mean	RMS	Mean
40	3.57	-2.26	2.15	0.31	1.46	-0.95	1.08	-0.77
50	1.29	-0.66	2.01	-0.20	1.23	0.17	1.29	-0.84
60	1.33	-0.70	1.62	-2.27	0.85	-0.35	0.88	0.01
70	1.56	-0.97	2.05	-1.50	1.50	-0.89	1.14	0.43
80	1.63	-1.18	1.15	-0.50	1.05	-0.34	1.22	-0.24
100	1.90	-0.80	1.74	-1.20	1.33	-0.43	1.55	-0.76

Table 4.6 represents the tabulated RMS and mean deviation of all measured points between 90% to 10% isodose compared to calculated points. The RMS value of less than 2% for all energies at both 90% and 80% isodose levels were achieved expect for 80% level and 9 MeV in which this deviation increased up to 2.2%. The mean deviation was within 1% for all energies and isodose levels.

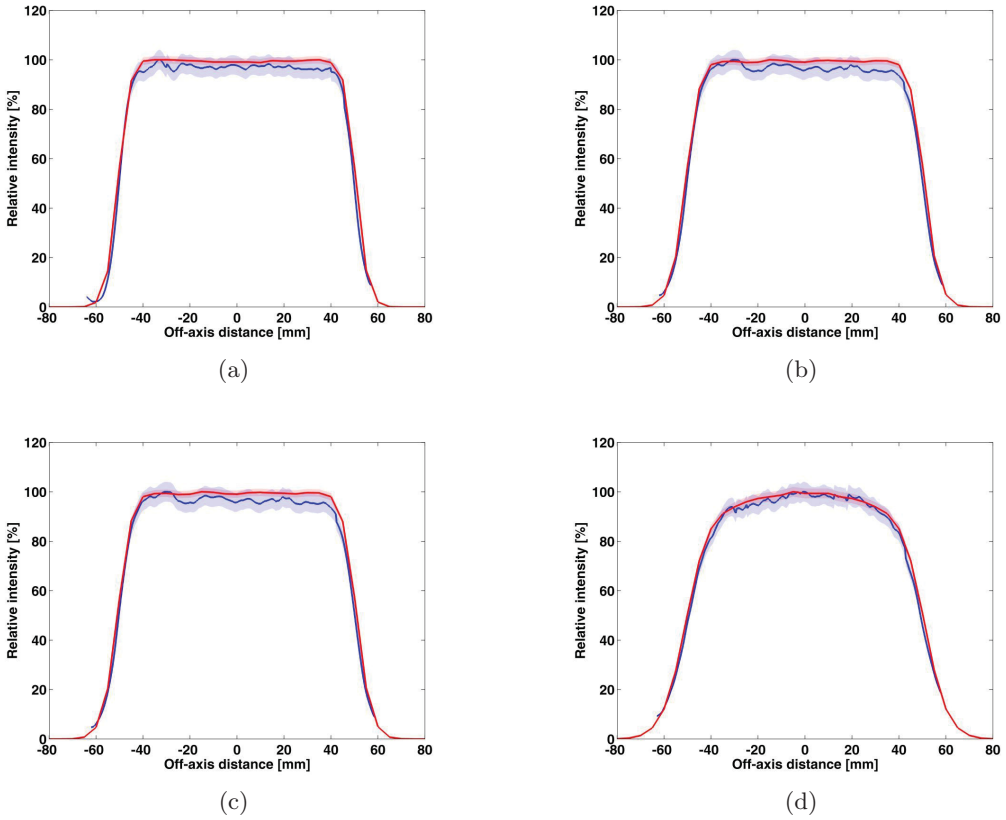

Figure 4.5.: Off-axis profiles comparison at 80% isodose level between DOSXYZnrc simulation (red line) and film measurement (blue line) for (a) 3 MeV; (b) 5 MeV; (c) 7 MeV and (d) 9 MeV electron beams. The shaded areas around the lines represent the uncertainity of obtained data.

4.2.1. Uncertainty analysis

As described in subsection 2.4.5, the uncertainty of a Monte Carlo calculation is proportional to the reciprocal root of number of histories ($\frac{1}{\sqrt{N}}$) used in the calculation. In this investigation, using BEAMnrc user code, the simulation of 10^7 to 10^8 histories was necessary to get a statistical uncertainty of calculated dose values of about 0.5 – 1% in the region between the surface and the depth corresponding to 10% of the maximum dose. The CPU time for calculating a depth dose curve was in the range of 24 h using a 3.2 GHz six-core processor with 6 GB RAM. The uncertainty in the dose calculation using DOSXYZnrc was 0.1%. Another source of uncertainty

was the NOVAC7 output constancy, for which a value of 2.5% was considered in this study. Moreover, the uncertainty inherited in the relative film dosimetry should not be ignored. Hence, in this study an uncertainty value of 1.5% was taken into account. Therefore, a maximum combined uncertainty of 3.1% should be considered for the results.

Table 4.6.: The RMS and mean values (in percent) obtained by comparing off-axis profiles resulted by DOSXYZnrc calculation and measured data in 80% to 10% dose fall-off region (see figure 4.5). The values are obtained at 80% and 90% isodose levels of the depth-dose profile for all available energies at 100 mm applicator. "plus" represents the positive off-axis distance and "minus" refers to negative off-axis distance.

Energy (MeV)	Isodose (%)	RMS plus	Mean plus	RMS minus	Mean minus
3	90	0.78	-0.68	0.75	0.37
	80	0.97	-0.89	0.71	0.56
5	90	0.93	-0.81	0.60	0.53
	80	1.98	-1.19	0.65	0.62
7	90	0.82	-0.07	0.73	0.70
	80	0.96	-0.82	0.90	0.86
9	90	1.75	-1.17	0.85	0.78
	80	2.21	-0.15	0.88	0.79

4.3. Stopping power ratios and output factors

4.3.1. Output factors

The deviations of the correction factors for ion recombination and the polarity effect, which are applied during ionization chamber dosimetry, were within 4% and 0.8%, respectively. Therefore, the ion chamber readings were corrected for these quantities. The uncertainty of the pin-point chamber for absorbed dose determination was about 2%. Table 4.7 shows the results of percentage dose measurements achieved by pin-point chamber and the extracted values of beam quality index (R_{50}) and z_{max} which were used for beam OF determination. The measured data are in good conformity with the tolerance level of acceptance recommended by the manufacturer ($\pm 3\,\mathrm{mm}$).

Table 4.7.: The electron beam parameters extracted from the percentage depth dose measured by the pin-point ionization chamber for 3, 5, 7, and 9 MeV electron beams, 100 mm applicator and 0 ° bevel. R_{50} is the depth at which the depth dose reaches its 50% dose level and z_{max} refers to the depth of maximum dose.

Energy (MeV)	R_{50}(mm)	z_{max}(mm)
3	1.2	5.5
5	1.7	7.2
7	2.6	10.7
9	33.4	14.0

It should be noted that, only the most accurate experimental OFs were considered, namely the OFs relevant to the higher energies (7 and 9 MeV) and are reported in table 4.8. At the lower energies (3 and 5 MeV), the PDD curves around z_{max} were rather sharp and the uncertainty on the dosimeter positioning at z_{max} had a prominent effect on the dosimeter response. This effect is considerably less important at the energies of 7 and 9 MeV.

Table 4.8.: Monte Carlo calculated and measured relative output factors (ROFs) for 7 and 9 MeV nominal electron beams for intraoperative radiation therapy at different fied sizes (40-80 mm). Output factors measurement was performed by a pin-point ion chamber in water and the calculated data are obtained from depth dose calculation in BEAMnrc user code.

Nominal energy (MeV)	Applicator (mm)	ROF calculated	ROF measured	Difference (%)
7	40	1.468	1.440	+1.9
	50	1.414	1.385	+2.1
	60	1.347	1.309	+2.9
	70	1.216	1.222	-0.5
	80	1.145	1.141	+0.3
9	40	1.609	1.567	+2.7
	50	1.519	1.520	-0.1
	60	1.416	1.380	+2.6
	70	1.261	1.241	+1.6
	80	1.178	1.150	+2.4

As table 4.8 shows, the calculated OFs are in close agreement with the measured results. The table also shows that the difference between calculated and measured results did not change significantly at lower applicator's diameter. It it notable to mention that, the OF values measured by ion chamber are mostly lower than corresponding predicted values (see table 4.8). This tendency was also observed by a previous study and it is mainly due to the usage of ionisation chambers for such measurements [23].

Table 4.9 illustrates electron fluence on the plane positioned at the end of the applicators and number of charged particle steps in dose regions per initial histories. As it is shown, the electron fluence increased with decreasing the applicator diameter which is in consistent with the findings of Miahalescu et al. [23]. The number of charged particle steps in dose region per initial history which is an indicator of the number of interactions in the dose region are also shown in this table. It can be claimed that as the applicator diameter decreased, the number of steps increased which led to a rise of the deposited energy and consequently to higher OF values in dose regions.

Table 4.9.: BEAMnrc calculation regarding the electron fluence on the calculation plane positioned (simulated) at the end of the applicators (40-100 mm) and the number of charged particle steps in dose regions per initial histories for 7 and 9 MeV electron beams produced by the NOVAC7.

Energy (MeV)	Applicator (mm)	Electron/cm^2 per incident particle	Num. of particle steps in dose region per initial history
7	40	3.873E-03	2.919
	50	4.063E-03	2.832
	60	4.067E-03	2.679
	70	3.831E-03	2.427
	80	3.684E-03	2.279
	100	3.332E-03	2.016
9	40	5.855E-03	5.210
	50	5.934E-03	4.988
	60	5.784E-03	4.663
	70	5.354E-03	4.151
	80	5.068E-03	3.872
	100	4.313E-03	3.299

4.3.2. Water-to-air stopping power ratios

The data shown in tables 4.10 and 4.11 refer to the results of $s_{w,air}$ on the phantom surface (z_0) and at the reference depths (z_{ref}) according to the TRS-398 and DIN 6800-2 [7, 9]. These data are presented as a function of energy and applicator diameter. On the water surface, as it is seen in table 4.10, the differences between Monte Carlo values and those of TRS-398 are from -0.1% to -0.3%. Those differences are almost identical with the results reported by Pimpinella et al. [22]. In their study, the corresponding deviation was in the range from 0.3% to 0.0%. At the reference depth z_{ref}, as shown in table 4.11, the differences between Monte Carlo values and corresponding values obtained by TRS-398 for lower energies (3 and 5 MeV) are slightly less than higher energies (-0.3% vs. -0.7%).

In table 4.12, the deviations between the $s_{w,air}$ values obtained by Monte Carlo simulation and measurement are reported as a function of energy and applicator diameter. The difference between Monte Carlo calculated $s_{w,air}$ values and those determined using TRS-398 protocol at z_{ref} for 9 MeV, as it is shown in table 4.12, is between -0.6% and -0.8%. The corresponding deviation range for 7 MeV is between -0.7% and -0.8%, while for 5 and 3 MeV this variation changed in the range from -0.6% to -0.7% and -0.2% to -0.7%, respectively.

Furthermore, the variation of the $s_{w,air}$ values, changing the field size (from 40 mm diameter to 100 mm diameter), can be also observed in the following tables. Based on the data resulted from the calculation, the variation of $s_{w,air}$ at z_{ref} among different field sizes for 3, 5, 7 and 9 MeV was found to be within -0.2%, +0.09%, +0.05% and +0.1%, respectively. This variation of $s_{w,air}$ was not significant considering the combined uncertainty of 2% that should be taken into account for these data. This result is consistent with the data published by Pimpinella at al. for 9 MeV [22].

Table 4.10.: Comparison between $s_{w,air}$ values obtained using TRS-398 dosimetry protocol (meas.) and SPRRZnrc Monte Carlo code (sim.) on water surface for 100 mm applicator.

Energy (MeV)	R_{50}(mm)	$s_{w,air}(meas.)$	$s_{w,air}(sim.)$	Difference (%)
3	13.0	1.062	1.063	-0.12
5	18.0	1.046	1.045	-0.10
7	26.0	1.027	1.025	-0.17
9	33.0	1.014	1.010	-0.33

Table 4.11.: Comparison between $s_{w,air}$ values obtained using TRS-398 dosimetry protocol (meas.) and SPRRZnrc Monte Carlo code (sim.) at reference depth (z_{ref}) for 100 mm applicator.

Energy (MeV)	z_{ref}(mm)	$s_{w,air}(meas.)$	$s_{w,air}(sim.)$	Difference (%)
3	6.8	1.096	1.093	-0.27
5	9.8	1.084	1.080	-0.37
7	14.6	1.070	1.062	-0.75
9	18.8	1.061	1.053	-0.70

Table 4.12.: Difference between the $s_{w,air}$ values obtained by measurement and simulation for different electron energies (3, 5, 7 and 9 MeV) and applicators (40-100 mm).

Energy (MeV)	App. (mm)	z_{ref}(mm)	$s_{w,air}(meas.)$	$s_{w,air}(sim.)$	Diff. (%)
3	40	6.9	1.095	1.093	-0.22
	50	6.6	1.096	1.090	-0.59
	60	6.7	1.096	1.090	-0.56
	70	6.8	1.096	1.092	-0.36
	80	6.3	1.098	1.090	-0.73
	100	6.8	1.096	1.092	-0.34
5	40	9.4	1.085	1.078	-0.62
	50	9.7	1.085	1.077	-0.72
	60	9.7	1.085	1.077	-0.72
	70	9.6	1.085	1.077	-0.72
	80	9.7	1.085	1.077	-0.72
	100	9.6	1.085	1.077	-0.72
7	40	14.5	1.071	1.062	-0.84
	50	14.4	1.071	1.062	-0.84
	60	14.8	1.070	1.062	-0.75
	70	14.5	1.071	1.062	-0.84
	80	14.7	1.070	1.062	-0.75
	100	14.6	1.070	1.062	-0.75
9	40	18.2	1.062	1.053	-0.81
	50	18.3	1.062	1.054	-0.74
	60	18.5	1.062	1.053	-0.80
	70	18.6	1.061	1.054	-0.66
	80	18.3	1.062	1.053	-0.85
	100	18.8	1.061	1.053	-0.70

Figures 4.6(a-d) show the Spencer-Attix water-to-air stopping power ratios as a function of depth in water for all possible electron beams for the reference applicator (100 mm). The data are compared to the TRS-398 dosimetry protocol [7]. The differences between Monte Carlo values and those given by the TRS protocol were within 0.7% from water surface to reference depth.

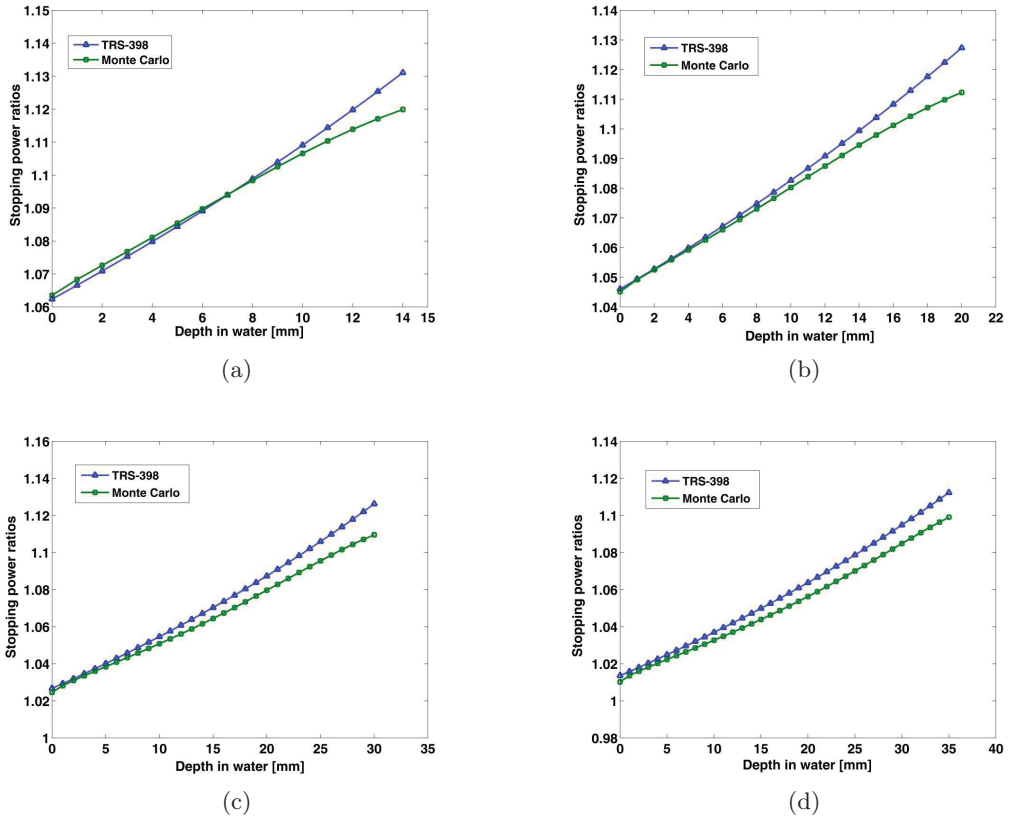

Figure 4.6.: Spencer–Attix water-to-air stopping power ratios (Δ=10 keV), $s_{w,air}$ as a function of depth in water for: (a) 3 MeV; (b) 5 MeV; (c) 7 MeV and (d) 9 MeV. The data are compared to the IAEA TRS-398 dosimetry protocol.

4.3.3. Uncertainty analysis

Different sources of uncertainties are involved. The combined uncertainty of the data for output factor determination shown in table 4.8 was 3.2% (1σ). This is the quadratic sum of the uncertainties of the absorbed dose measured with the pin-point chamber (2% at 1 SD) and the 2.5% long-term reproducibility of the NOVAC7 accelerator output. Furthermore, on the one hand, the absorbed doses calculated by Monte Carlo simulation were determined in circular voxels of 5 mm radius and 1 mm height with statistical uncertainties of about 0.6% (1σ) resulted at the depth of calculation. Therefore, a combined uncertainty of 3.3% should be considered for output

factor values. On the other hand, for determination of stopping power ratios, 1% uncertainty inherited in phase space files of BEAMnrc should be considered. In addition, for $s_{w,air}$ calculation using TRS-398, 3% uncertainty in the determination of R_{50} should be accounted. This is the sum of the 1.5% uncertainty of Gafchromic dosimetry and 2.5% output constancy of the NOVAC7. Thus, a combined uncertainty of 3.2% should be taken into account for the $s_{w,air}$ values in this study.

4.4. Scatter and contamination analysis

4.4.1. Energy fluence

The results regarding the characteristics of electron energy distribution has been given in this chapter (see section 4.2). In figures 4.7(a) and (b), the electron energy spectra are shown for direct, scattered and total electrons. The figures refer to low and high energies at reference field and important clinical fields. It was in general observed that the energy spectrum of electrons does not change significantly while decreasing the applicator diameter. This is in accordance with previous findings published by Björk et al. and Pimpinella et al. [22, 24]. Moreover, all the energy spectra were characterised by a low energy contribution.

4.4.1.1. Low Energies, Reference Field

As it is shown if fig. 4.7(a), the energy distribution of the direct electrons in general had a significant peak, at which the most probable energy of the spectrum occurred. This energy of the spectrum was at least 10% higher than the corresponding value resulted for scattered electrons. In this condition, 69 and 30% contribution at most probable energy was resulted for direct and scattered components, respectively. In this case, only the low energy area was dominated by scattered component while in the high energy region the direct electrons influenced substantially. However, the maximum contribution of scattered electrons for both energies achieved in average 38% of the maximum value of the most probable energy of the total electrons.

4.4.1.2. High Energies, Reference Field

Contrary to low energies, the contribution of scattered electrons were substantially lower than the direct ones. At its most probable energy, the scattered component had only 17% contribution to the total electron distribution. In other words, their contribution was decreased approximatly

13%, compared to the corresponding contribution of lower energies. A maximum contribution of 26% of scattered electrons was observed, compared with the energy fluence of total electrons (see fig. 4.7(b)). Scattered electrons were dominant at low energy regions, whereas direct electrons were more significant at higher energy regions of the spectrum.

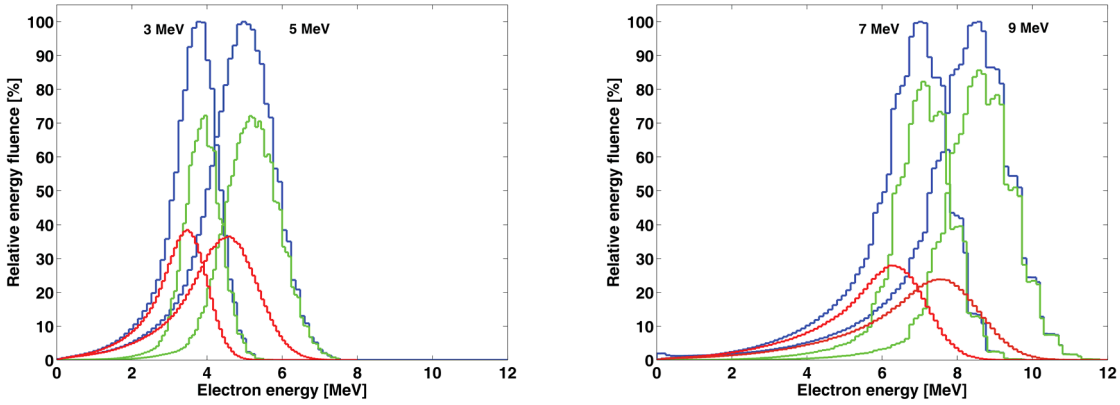

(a) (b)

Figure 4.7.: Relative energy fluence distribution of total (blue), direct (green) and scattered (red) components for (a) 3 and 5 MeV electron beams versus (b) 7 and 9 MeV as a function of electron energy for 100 mm applicator.

4.4.1.3. Low Energies, Clinical Fields

The results show that the contribution of scattered electrons was increased significantly. It can be seen from fig. 4.8(a) that the relative contribution of them was 61% at 3 MeV and 40 mm applicator, compared to the maximum value of total electron. Scattered component played a dominant role not only at low energies but also at high energies where direct electrons are typically present. Hence, relative contribution of the scattered electrons to the total energy fluence was increased with decreasing the applicator diameter. There are no data to verify these results quantitatively but Pimpinella et al. reported similar results regarding 60 mm applicator [22].

4.4.1.4. High Energies, Clinical Fields

Similar to low energies, it was observed that the scatter contribution was increased when the field size was decreased. This tendency was, however, less significant for lower energies. The

relative contribution of direct component was still dominant at higher energies. Its fluence was greater than scattered component. At the smallest field size of 40 mm, however, both components showed equal relative contribution to the value of most probable energy, as it is depicted in figs. 4.8(c) and (d).

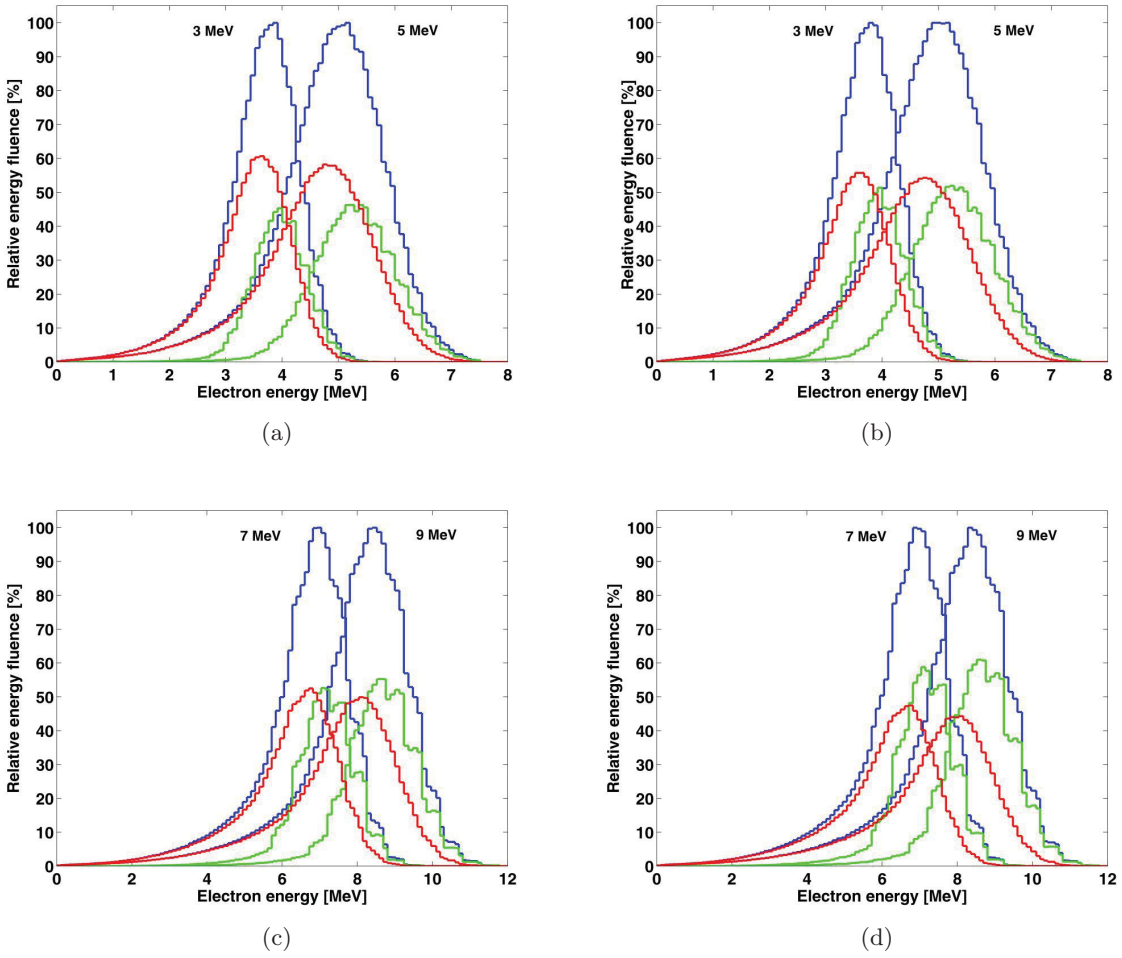

Figure 4.8.: Relative energy fluence distribution of total (blue), direct (green) and scattered (red) components (a) and (b) for low energies, 40 and 50 mm applicators, respectively, and (c) and (d), high energies, 40 and 50 mm applicators, respectively.

4.4.1.5. Energy fluence of contaminant photons

The photon energy spread curves, as can be seen in figs. 4.9(a-c), were similar for all energies and applicator diameters. They had large intensity at low energy bins and were decreased toward zero with increasing the values of energy bin. The maximum contribution of photon fluence at 40 mm applicator was nearly 1.7% of the maximum intensity of the most probable energy of

total electrons (see figs. 4.7(b) and 4.8(d)). The photon energy fluence for 50 mm applicator was larger than that of 40 and 100 mm applicators. It reached 6.0, 7.0, 5.3 and 6.0% of the intensity of the most probable energy of total electrons for 3, 5, 7 and 9 MeV, respectively (see figs. 4.8 and 4.9). As indicated in fig. 4.9(c), at reference field size (100 mm), the contribution of photon component was decreased significantly compared to 50 mm applicator. It reached in average 1.6% of the intensity of the most probable energy of total electrons.

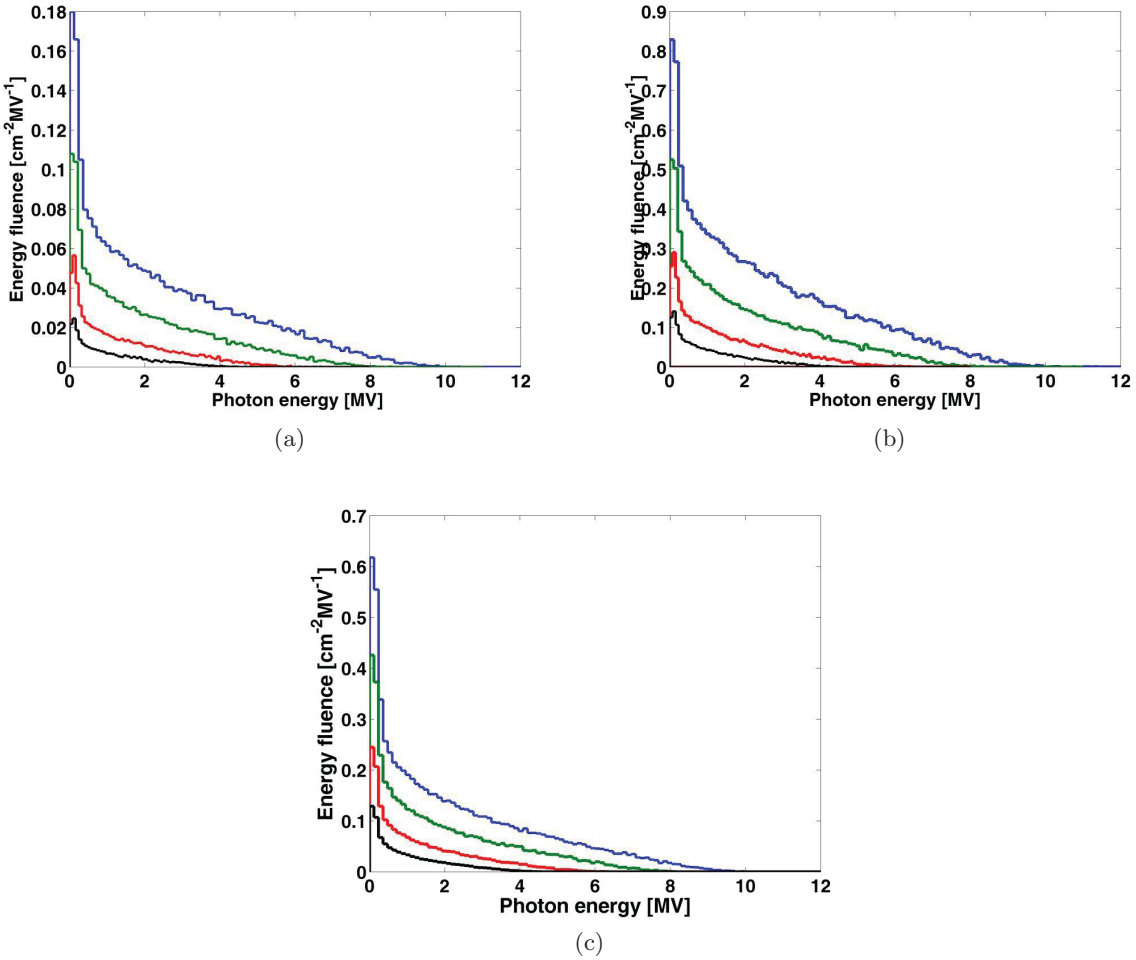

Figure 4.9.: Simulated (BEAMDP) energy spectra of bremsstrahlung photons at the exit of the applicator resulted for 3 (black), 5 (red), 7 (green) and 9 MeV (blue) electrons and (a) 40 , (b) 50 and (c) 100 mm applicator diameters.

4.4.2. Fluence distribution

Fluence and mean energy of electrons were determined to investigate the beam uniformity at the phantom surface. Figs. 4.10 (a-d) shows the electron fluence distribution of direct, scattered and total components as a function of radial (off-axis) distance at 100 mm applicator for 3, 5, 7 and 9 MeV electron beams, respectively. At this field size, different behaviors were observed for different energies which are presented in detail in the following subsections.

4.4.2.1. Low Energies, Reference Field

On the one hand, the total fluence for 3 and 5 MeV was flat around the central axis but was increased 6.5 and 8.5% toward the field edge for each energy, respectively. Around the central axis on the other hand, increasing the energy from 3 to 5 MeV led to a decrease of the fluence of the scattered component from 45 to 41%, relative to the maximum value of the total component. It means a 4% raise of the contribution of the direct component. Toward the field edge, increasing the energy from 3 to 9 MeV caused reduction to the fluence of the scattered electrons of approximately 10%. The corresponding change was -18% on the central axis (see figs. 4.10(a) and (b)).

4.4.2.2. High Energies, Reference Field

The total fluence for 7 MeV was flat around the central axis but was increased 4.8% toward the field edge. However, it was decreased about 3.4% for 9 MeV. It should be noted that the values are relative to the maximum value of total electrons. The contribution of scattered electrons toward the field edge was higher than that of direct ones. For 7 MeV, the contribution of scattered electrons was increased from 34% on the central axis to 53% towards the applicator wall. The corresponding change for the direct component was from 65% to 47%. Moreover, at 9 MeV, 72% of the fluence around the central axis was related to the direct electrons against 28% of the scattered ones. Toward the field edge, however, each component contributed equally (50%) as can be seen from figs. 4.10(c) and (d).

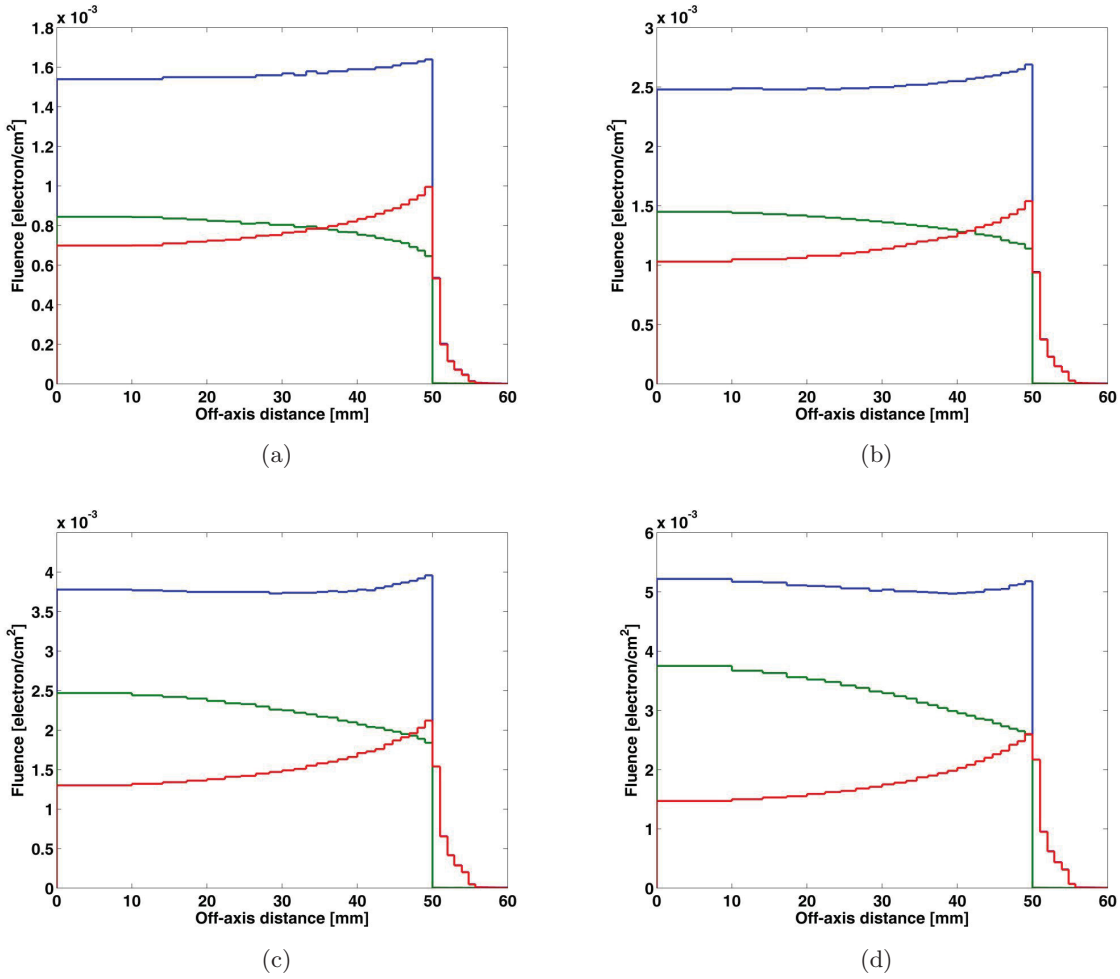

Figure 4.10.: Comparison of total, direct and scattered contribution of (a) 3, (b) 5, (c) 7 and (d) 9 MeV electrons on the fluence distribution as a function of off-axis distance for 100 mm applicator. The blue, green and red lines represent the total, direct and scattered components, respectively.

4.4.2.3. Low Energies, Clinical Fields

According to fig.4.11, the electron total fluence in clinical fields increased in average 17%, compared to the reference field. In addiation, the contribution of the scattered electrons to the total fluence was increased in average 17%. It is noteworthy that the direct and scattered components had similar contribution to the total componet. Moreover, reducing the field size from 50 to 40 mm caused in average 2.5% raise of the contribution of the scattered component.

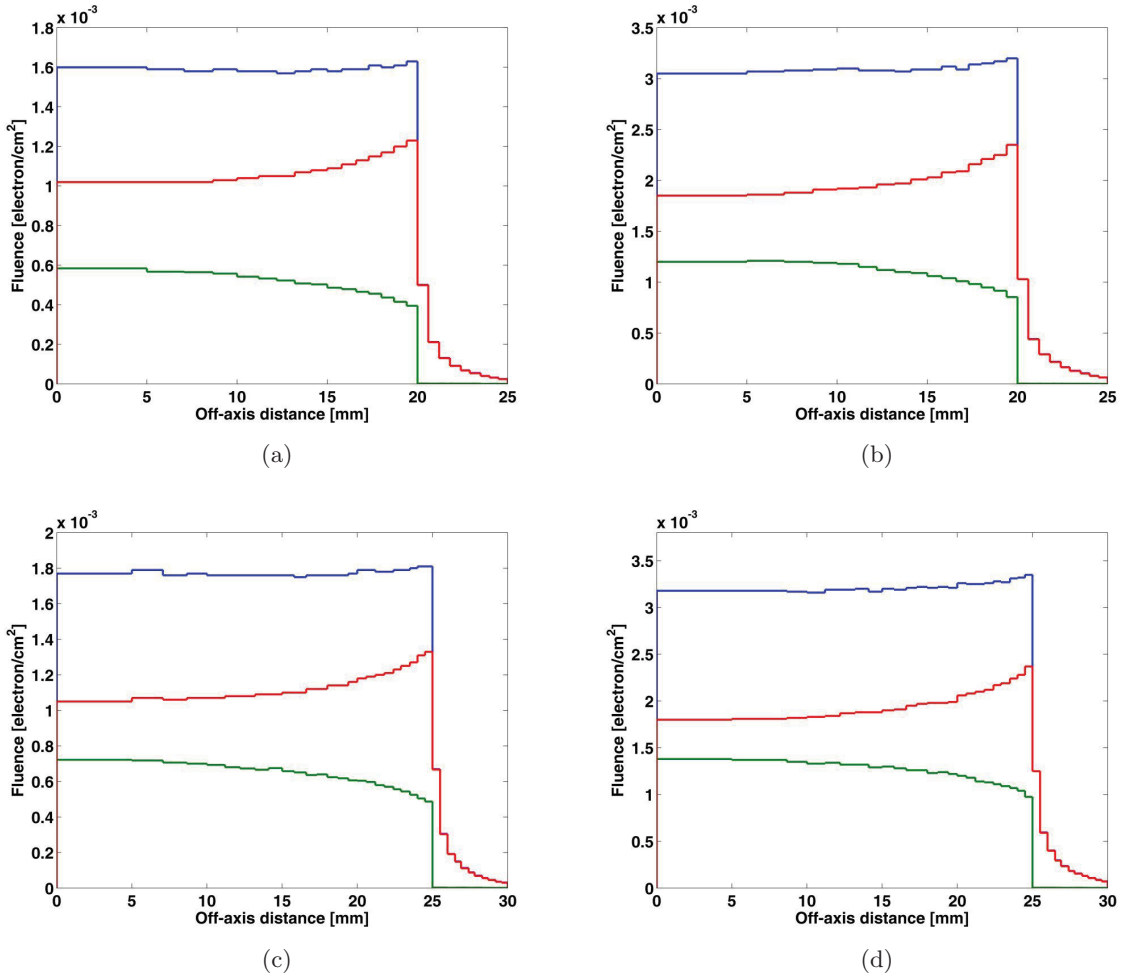

Figure 4.11.: Electron fluence of total (blue), direct (green) and scattered (red) components of low energies (3 and 5 MeV) for, (a) and (b), 40 mm and, (c) and (d), 50 mm applicators as a function of off-axis distance.

4.4.2.4. High Energies, Clinical Fields

As illustrated in figure 4.12, the fluence uniformity of the total component was similar to low energies. It was flat around the central axis but showed in average an increase of 9% around the field edge. Its intensity was increased in average 33% compared to the value of the reference field. The scattered component had a larger fluence than the direct component except for 9 MeV and 50 mm applicator. Its contribution to the total fluence was increased in average 22.5 and 16% around the central axis and field edge, respectively, compared to the corresponding values at the reference field. Moreover, reducing the field size from 50 to 40 mm increased this contribution in average 3.5%.

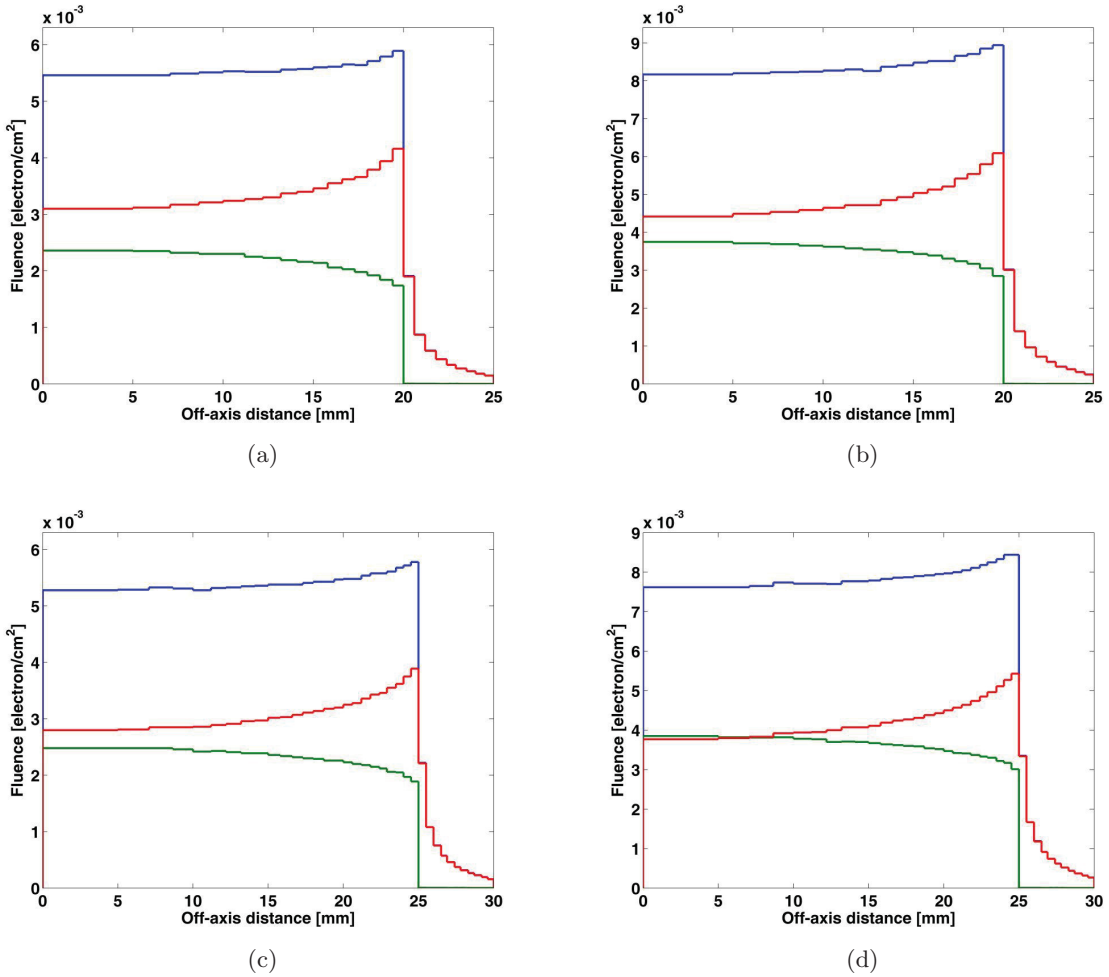

Figure 4.12.: Electron fluence of total (blue), direct (green) and scattered (red) components of high energies (7 and 9 MeV electron beams) for, (a) and (b), 40 mm and, (c) and (d), 50 mm applicators as a function of off-axis distance.

4.4.2.5. Fluence distribution of contaminant photons

The photon fluence as presented in fig. 4.13 had a flat shape around the central axis but reached a sudden peak around the field edge. For 100 mm applicator, the change of photon fluence towards the field edge with respect to the corresponding value at the central axis was -0.7, +3.8, +9.5 and +16% for 3, 5, 7 and 9 MeV, respectively. Analogous results were obtained for clinical fields as shown in fig. 4.13. The variation of this parameter near the applicator wall depended strongly on the filed size and energy. Björk et al. have also found similar conclusions [24]. The total photon fluence was increased approximately 29%, decreasing the applicator diameter.

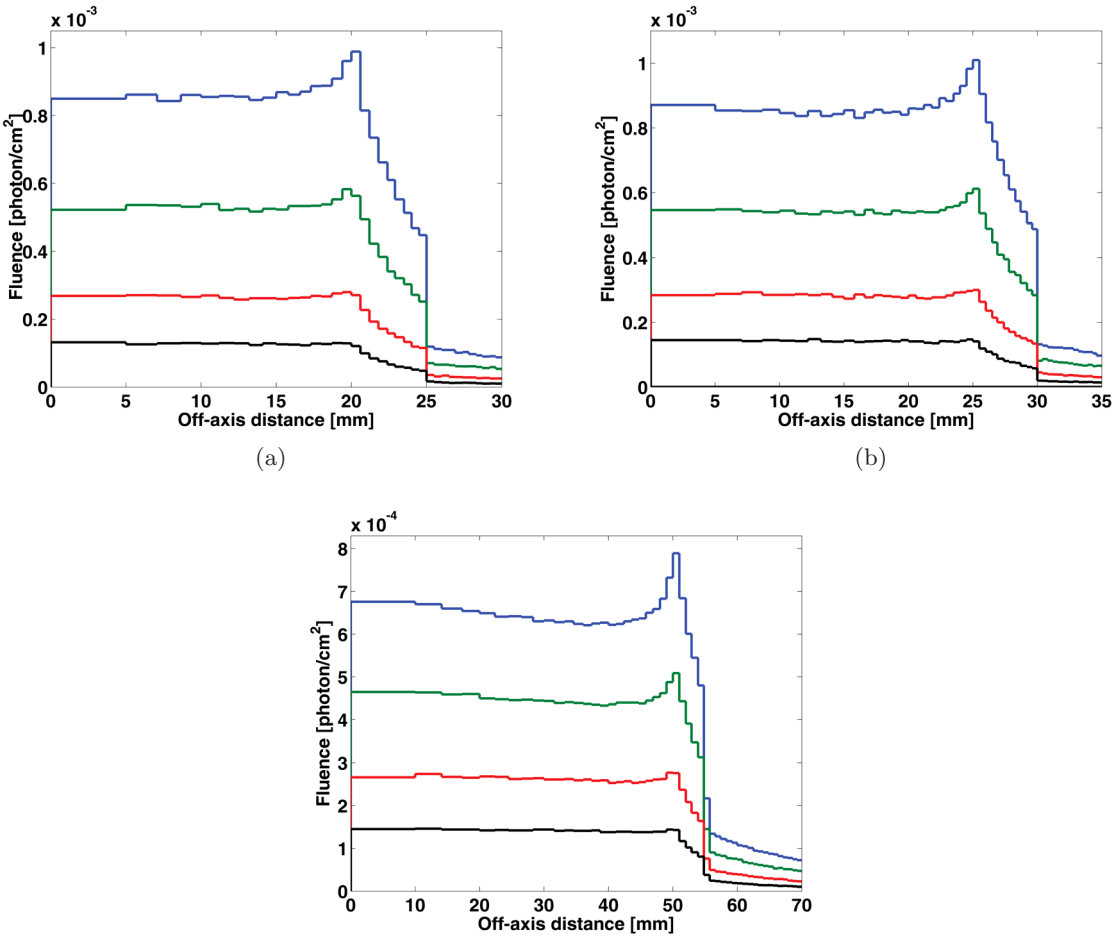

Figure 4.13.: Simulated fluence profiles of contaminent photons at the exit of the applicator resulted from 3 (black), 5 (red), 7 (green) and 9 MeV (blue) electron beams at (a) 40, (b) 50 and (c) 100 mm applicators as a function of off-axis distance.

4.4.3. Mean energy distribution of electrons

4.4.3.1. Low Energies, Reference Field

The mean energy distribution of low energy electron beams are presented in fig. 4.14. The values of mean energy for direct, scattered and total components obtained for 5 MeV beams were 4.91, 3.30 and 3.69 MeV, respectively. The corresponding values for 3 MeV were 3.65, 2.50 and 2.79 MeV. The mean energies of direct electrons were 47% more than the mean energies of the scattered electrons. The direct electrons had constant values inside the field and were always higher than the corresponding values of the total electrons. The mean energy distribution of scattered electrons showed an increase of about 2.5% moving toward the field edge.

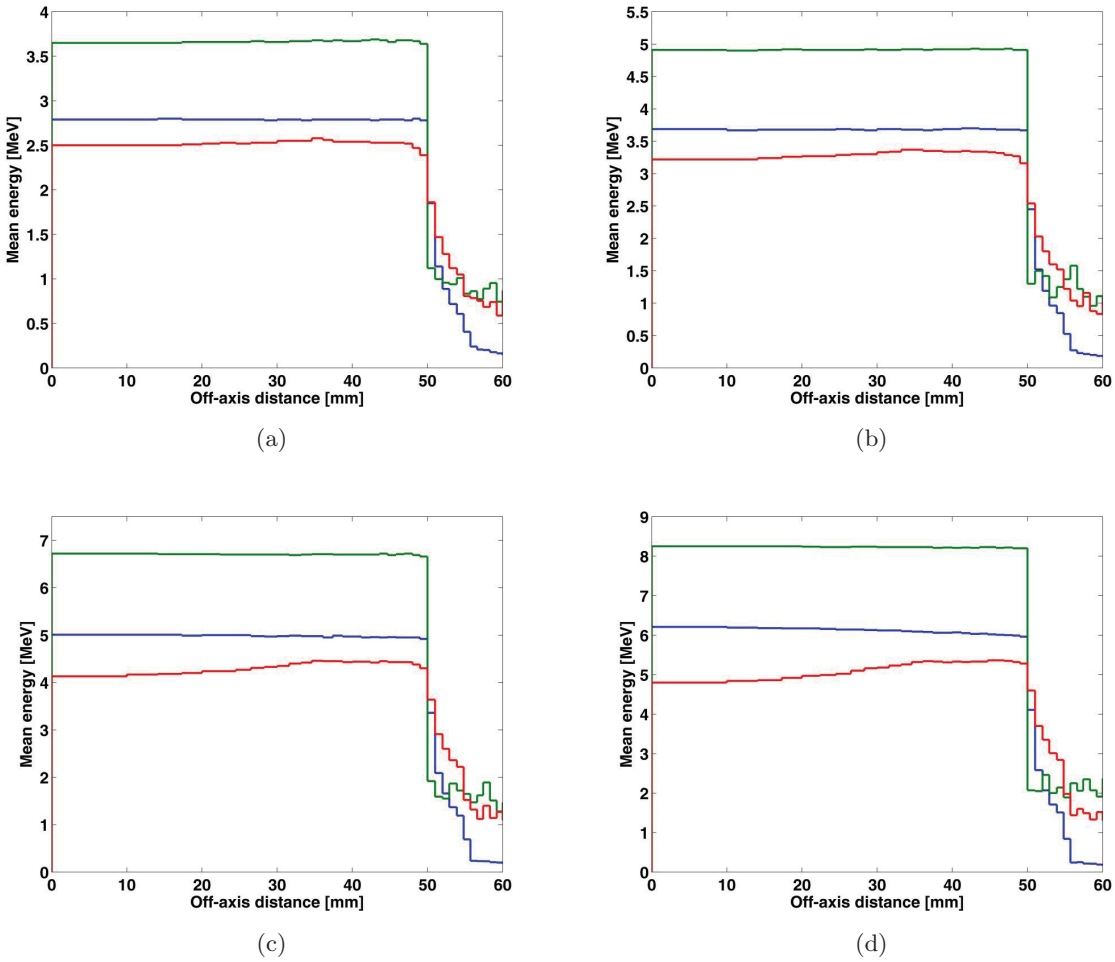

Figure 4.14.: Mean energy distribution of total (blue), direct (green) and scattered (red) electron components on the phantom surface for (a) 3, (b) 5, (c) 7 and (d) 9 MeV electron beams for 100 mm applicator.

4.4.3.2. High Energies, Reference Field

At the energy of 9 MeV, the mean energy of direct, scattered and total electrons were 8.25, 5.00 and 6.10 MeV, respectively (see figs. 4.14(c) and (d)). For 7 MeV, the corresponding values were 6.72, 4.30 and 5.00 MeV. The mean energies of direct electrons were 56 and 65% more than the mean energies of scattered electrons for 7 and 9 MeV, respectively. On the one hand, similar to low energies, the direct electrons showed constancy inside the field. On the other hand, contrary to low energies, the scattered electrons had low constancy inside the field. A 9% inconstancy was observed. In other words, the mean energy distribution of scattered electrons around the field edge showed an increase of about 7 and 11% for 7 and 9 MeV, respectively.

4.4.3.3. Low Energies, Clinical Fields

The mean energy distributions for low energies at clinical fields are plotted in fig. 4.15. The relation among direct, scattered and total electrons emerged a similar pattern. The mean energies related to the direct component deviated in average +4.5% from the corresponding values obtained for 100 mm applicator. Moreover, it is important to point out that the mean energy values of scattered component showed a 20% increase, compared to the value resulted for the reference field. This resulted to a 12.5% increase in the mean energy value of total electrons.

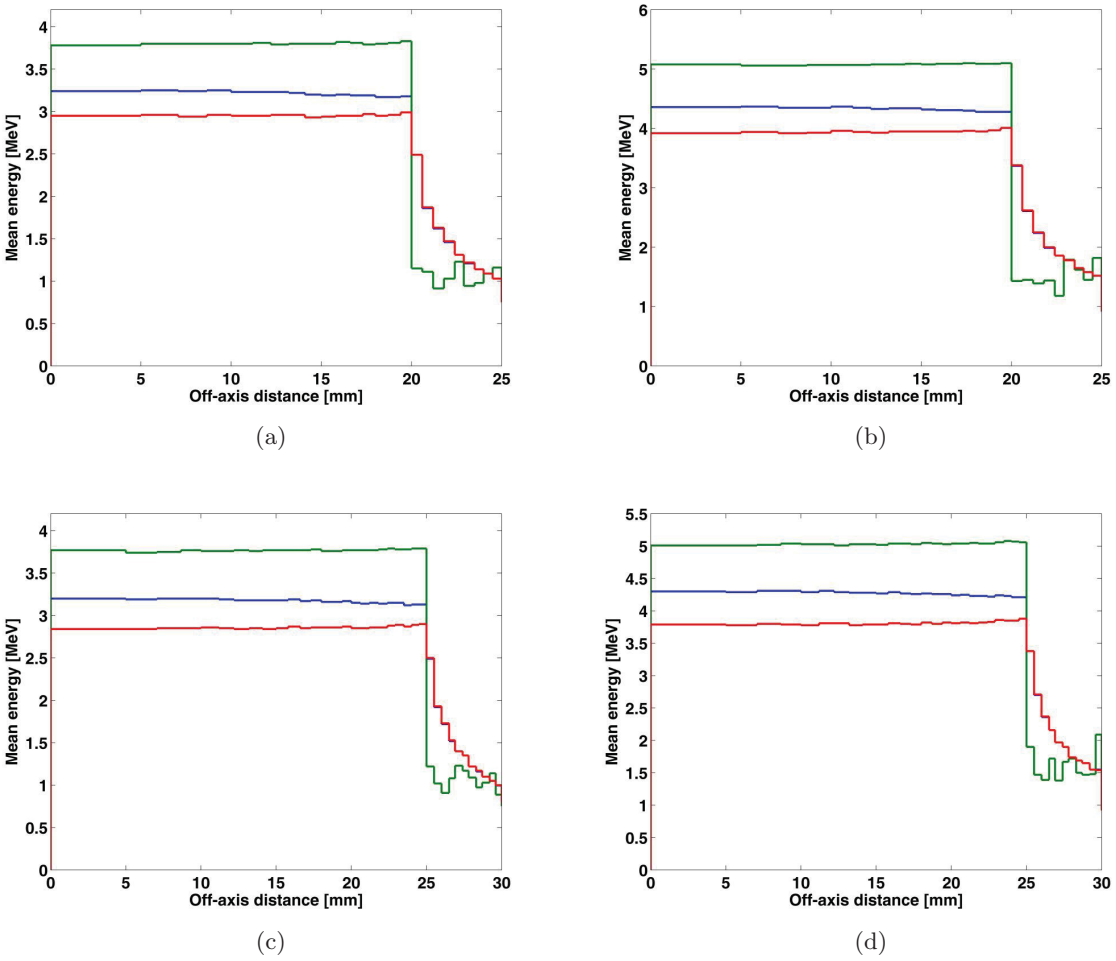

Figure 4.15.: Mean energy distribution of total (blue), direct (green) and scattered (red) components of low energies (3 and 5 MeV electron beams) for, (a) and (b), 40 mm and, (c) and (d), 50 mm applicators as a function of off-axis distance.

4.4.3.4. High Energies, Clinical Fields

The mean values of high energies for clinical applicators are plotted in fig. 4.16. The values related to the direct component deviated in average +2.1% from the calculated values for the reference field. It was observed that the mean energy values of scattered component raised 28%. This rise in the mean energy values of direct and scattered components led to a 18.2% increase in the mean energy value of total electrons. This trend was similar to the results obtained at low energy and clinical fields. It can also be seen that the constancy of direct electrons for both applicators was within 2% inside the field. This inhomogeneity ,however, was not observed for 100 mm applicators.

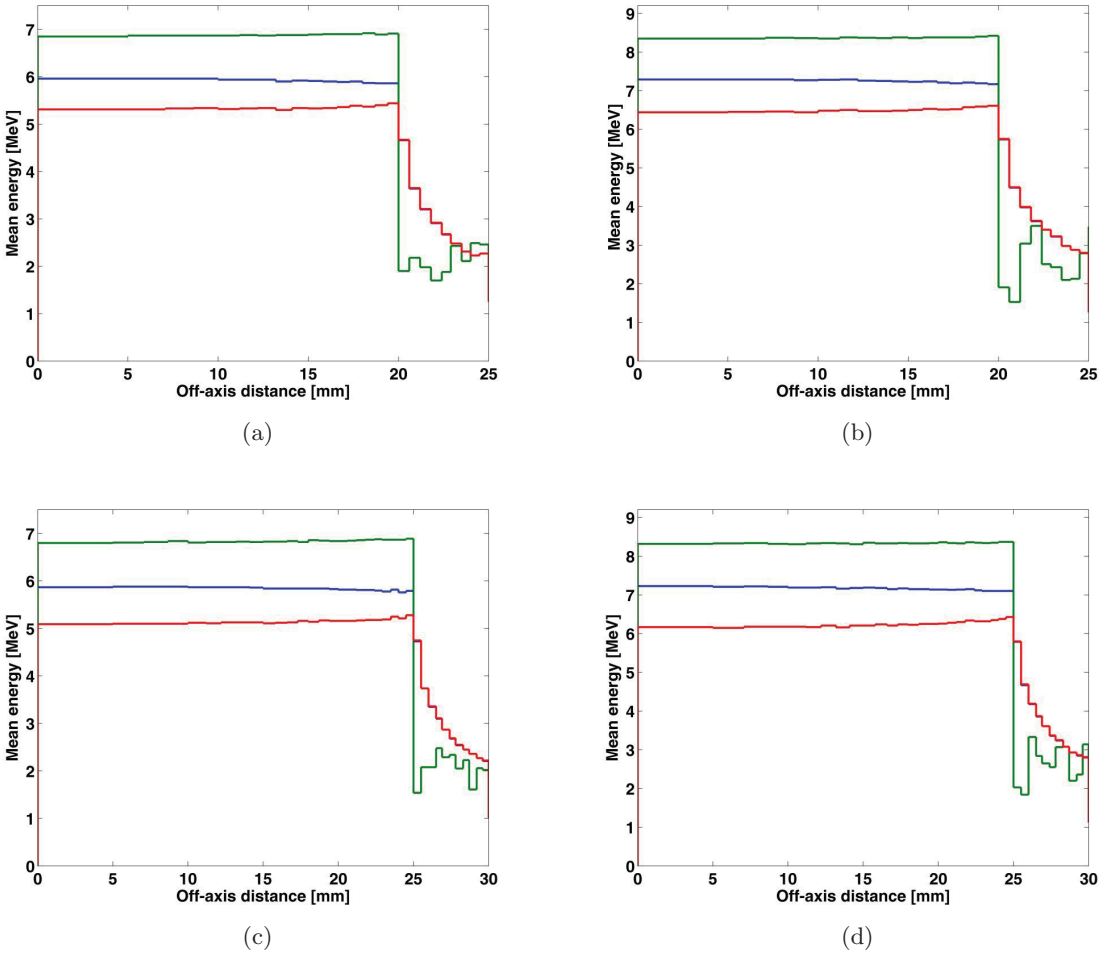

Figure 4.16.: Mean energy distribution of total (blue), direct (green) and scattered (red) components of high energies (7 and 9 MeV electron beams) for, (a) and (b), 40 mm and, (c) and (d), 50 mm applicators as a function of off-axis distance.

Consistent with the results obtained for low energies, an increase of 3.2% was observed in the mean energy distribution of scattered component near the field edge compared to central axis. It was much lower than the corresponding value of the reference field (about 9%).

4.4.3.5. Mean energy distribution of contaminant photons

Figure 4.17 shows the mean energy distribution of bremsstrahlung photons for 40, 50 and 100 mm applicators. It can be seen that this parameter was increased with decreasing the applicator diameter. This change was approximately 25% near the central axis. It was significant around the field edge (in average 17%).

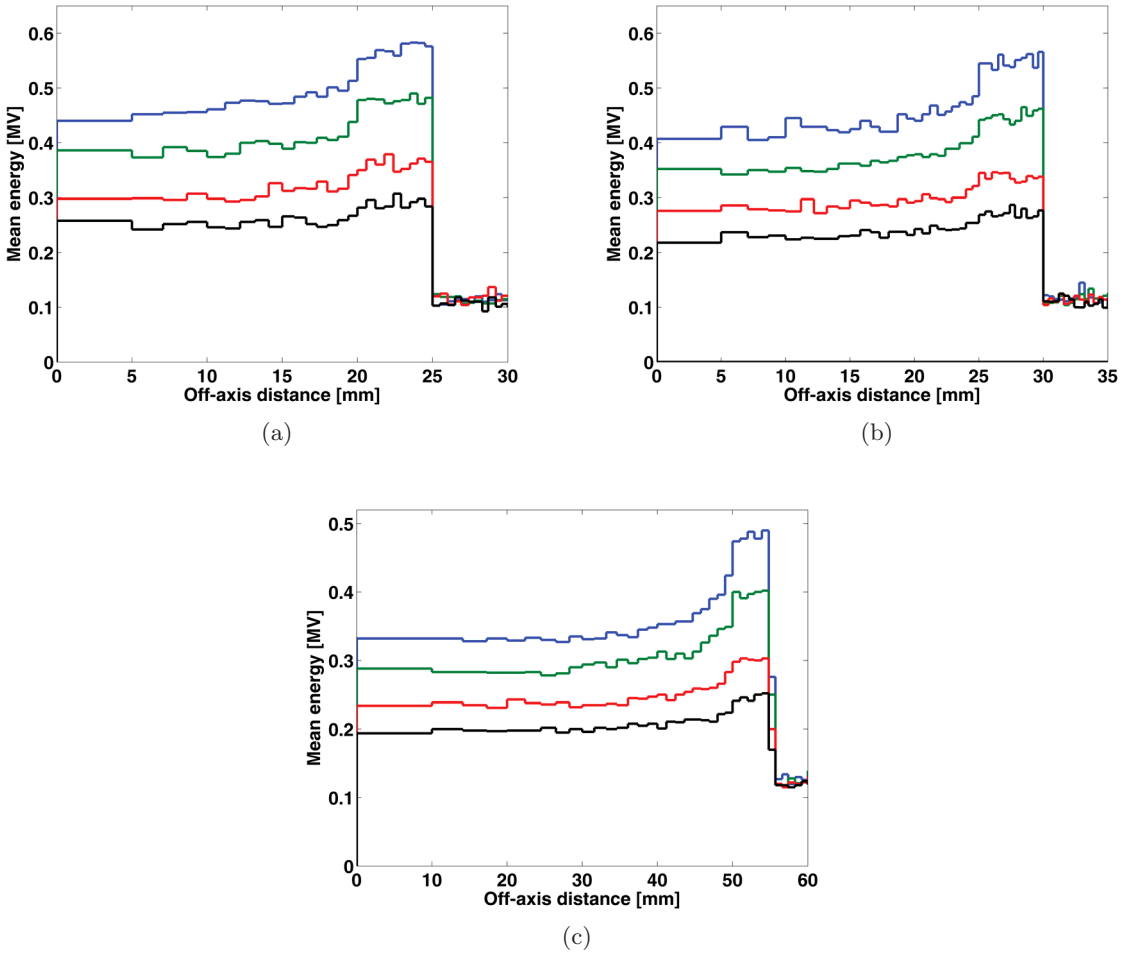

Figure 4.17.: Simulated mean energy distribution of contaminent photons at the exit of the applicator resulted from 3 (black), 5 (red), 7 (green) and 9 MeV (blue) electron beams at (a) 40, (b) 50 and (c) 100 mm applicators as a function of off-axis distance.

4.4.4. Angular distribution of electrons

The angular spread of the NOVAC7 electron beams is shown in figures 4.18 to 4.20. These figures refer to 3, 5, 7 and 9 MeV beams obtained for clinical (40 and 50 mm) and reference (100 mm) applicators. The angular distributions of the direct and the scattered electrons are also presented in these plots. A comparison of the most probable angle value, θ_p, the mean angle, θ_m and the full-width-at-half-maximum, Γ, values is given in table 4.13. As it can be seen in this table and corresponding plots, the angular distribution reached its maximum at small angles from central axis. The most probable angle for all components and energies, θ_p, changed between 2.2° and 9°, whereas the mean angle changed in the range from 3.6° to 15.3° and the Γ values varied between 2.7° and 13.5°. These results are consistent with findings of Pimpinella et al. [22]. The direct component had its maximum angle between 2.2° and 4.1° while the corresponding angle for the scatter component were from 4° to 9°. Due to remarkable change of angular parameters for each field size at different energy levels, an extensive discussion is necessary which is given below.

4.4.4.1. Low Energies, Reference Field

The θ_p value for the direct and the scattered electrons were 3.6° and 8.7°, respectively, which led to a value of 4.5° for the total electrons, as it is shown in figs. 4.18(a), (b) and in table 4.13. Furthermore, the θ_m value (10°) was more than twice higher than θ_p corresponded to the total electrons. Moreover, the Γ values were 5.8° and 11.8° for direct and scattered components, respectively, which caused a value of 7.3° for the total component. These results are consistent with the data reported by Pimpinella et al. [22].

4.4.4.2. High Energies, Reference Field

The angular distribution parameters of the scattered component were comparable to lower energies but smaller values were observed for the direct and total components. A reduction of 0.9°, 1.8° and 2.5° for the total component was observed compared to the corresponding values of lower energies for θ_p, θ_m and Γ, respectively. However, the corresponding change for the direct component was in average -0.6° regarding all angular parameters.

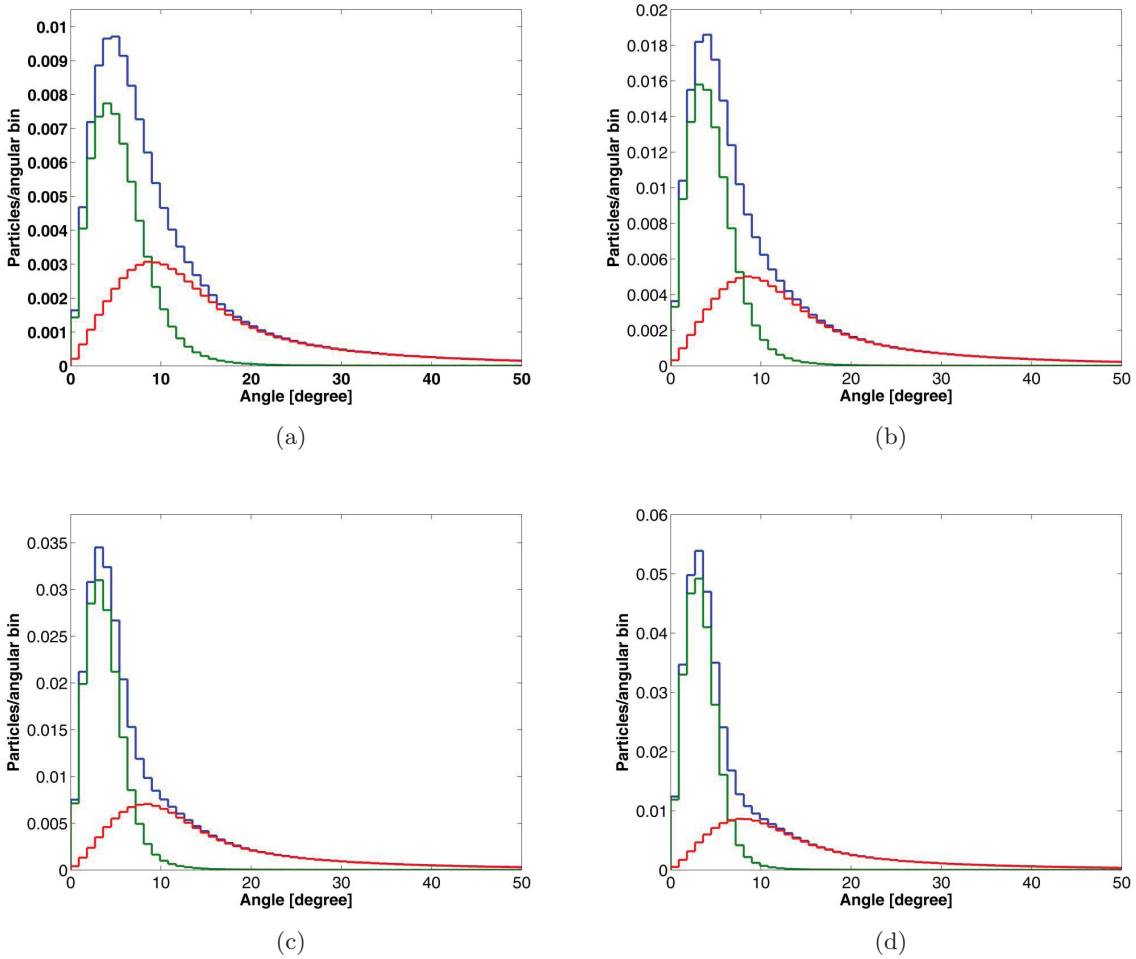

Figure 4.18.: Angular distribution of total (blue), direct (green) and scattered (red) electron components for (a) 3, (b) 5, (c) 7 and (d) 9 MeV electron beams for 100 mm applicator.

As presented in figs. 4.18(c) and (d), the most probable angle, θ_p, for the direct and total components was the same (3.1°) but increased to 8.1° for the scattered component. It can also be seen that Γ was 4.5° for the total and direct component, but was increased to 12.6° for the scattered component. The mean angle, was the smallest for the direct component (5.4°) and was increased significantly for the scatter component (14.1°), which is in accordance with the corresponding value reported in literature for 9 MeV and 100 mm applicator [22].

4.4.4.3. Low and High Energies, Clinical Fields

Figures 4.19 and 4.20 along with table 4.13 demonstrate that at clinical fields, the difference between angular parameters was lower than that of the reference field. Consistently, the θ_p value related to the total electrons for 5 MeV was the same as high energies although this difference

for 3 MeV increased slightly (less than 1°). It is noticeable that at clinical fields, θ_m and Γ corresponded to the total component decreased in average 2° when increasing the energy from 3 to 9 MeV. Meanwhile, angular parameters for direct and scattered components showed a slight reduction when increasing the energy from 3 to 9 MeV. In particular, for the direct component this reduction was 0.9°, 2.7° and 2.7° for θ_p, θ_m and Γ, respectively.

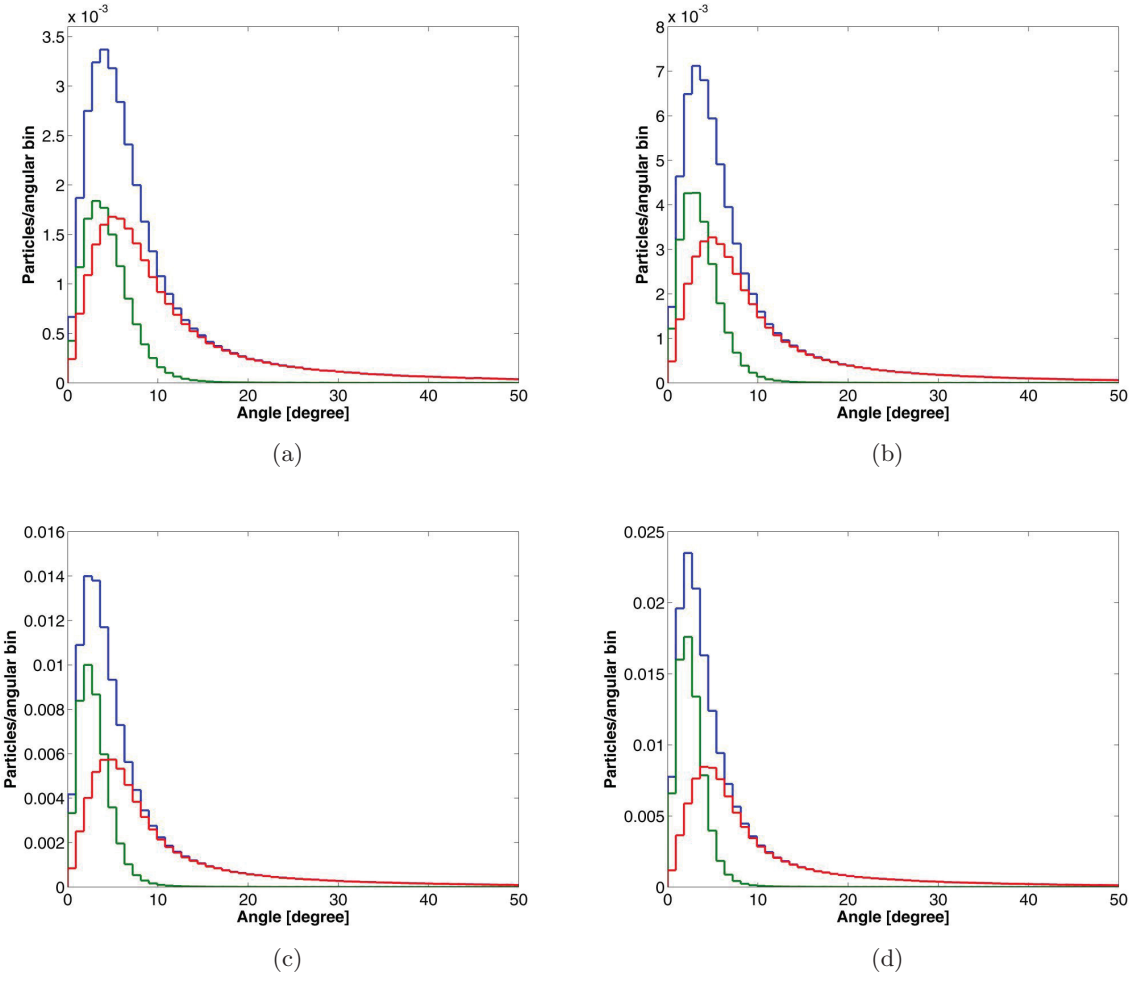

Figure 4.19.: Angular distribution of total (blue), direct (green) and scattered (red) electron components for (a) 3, (b) 5, (c) 7 and (d) 9 MeV electron beams for 50 mm applicator.

Changing the energy from 3 to 9 MeV for 50 mm applicator, a remarkable decrease of 0.9°, 1.8° and 2.7° was resulted for the scattered component for θ_p, θ_m and Γ, respectively. This difference was in average about 0.5° smaller for 40 mm applicator. Comparing these results at 9 MeV and 40 mm applicator with the data published by Pimpinella et al. resulted to a good agreement among different calculated parameters.

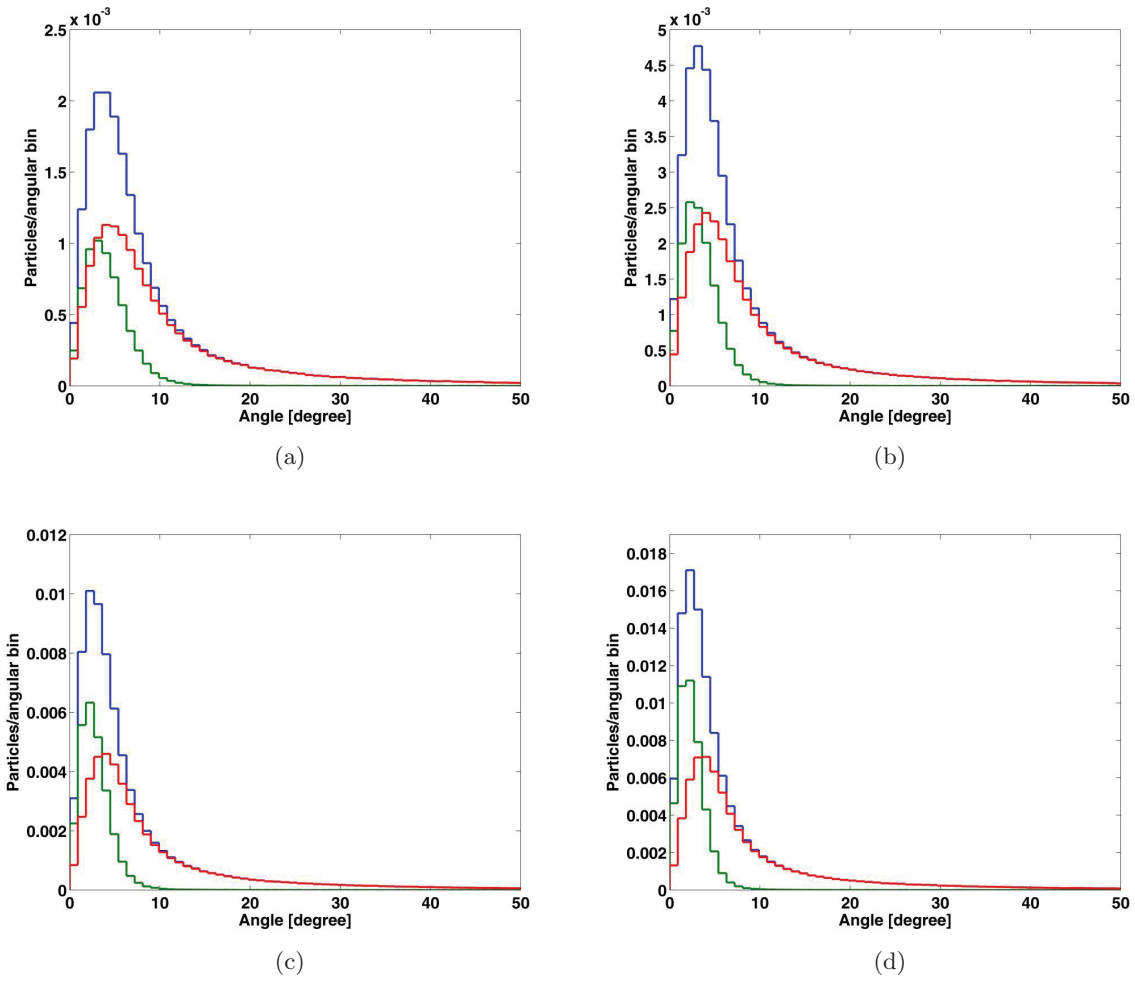

Figure 4.20.: Angular distribution of total (blue), direct (green) and scattered (red) electron components for (a) 3, (b) 5, (c) 7 and (d) 9 MeV electron beams for 40 mm applicator.

Table 4.13.: Angular distribution related to direct, scattered and total components of 3, 5, 7 and 9 MeV electron beams for 40, 50 and 100 mm applicators. θ_p, θ_m and Γ are the most probable angle, the mean angle and the full-width-at-half-maximum, respectively. The values are expressed in degrees.

Energy (MeV)	App.(mm)	Direct			Scattered			Total		
		θ_p	θ_m	Γ	θ_p	θ_m	Γ	θ_p	θ_m	Γ
3	40	3.1	6.3	5.4	4.5	9.9	8.1	3.6	9.0	5.4
5		2.2	5.4	4.5	4.0	9.0	7.2	3.1	8.1	5.4
7		2.2	4.5	3.6	4.0	9.0	6.3	2.2	7.2	4.5
9		2.2	3.6	2.7	4.0	8.1	6.3	2.2	7.2	3.6
3	50	3.1	6.3	5.4	4.9	10.8	9.0	4.0	9.0	7.2
5		3.1	5.4	4.5	4.9	9.9	8.1	3.1	8.1	6.3
7		2.3	4.5	3.6	4.6	9.9	7.2	2.2	8.1	5.4
9		2.2	3.6	2.7	4.0	9.0	6.3	2.2	7.2	4.5
3	100	4.1	8.1	7.2	9	15.3	13.5	5.0	10.8	8.1
5		3.2	6.3	5.4	8.5	14.4	12.6	4.0	9.0	7.0
7		3.1	6.2	4.5	8.3	14.4	12.5	3.3	8.1	5.4
9		3.1	5.4	4.5	8.1	14.1	12.6	3.1	7.2	4.5

4.4.4.4. Angular distribution of contaminant photons

The angular distributions of bremsstrahlung photons are shown in fig. 4.21 which refers to 3, 5, 7 and 9 MeV beams and 40, 50, and 100 mm applicators. A comparison of θ_p, θ_m and Γ is given in table 4.14. For each applicator size the angular distribution did not change dramatically varying the electron energy. However, a significant change in the θ_p, θ_m and Γ values was observed among the largest field size of 100 mm and the smaller applicator diameters.

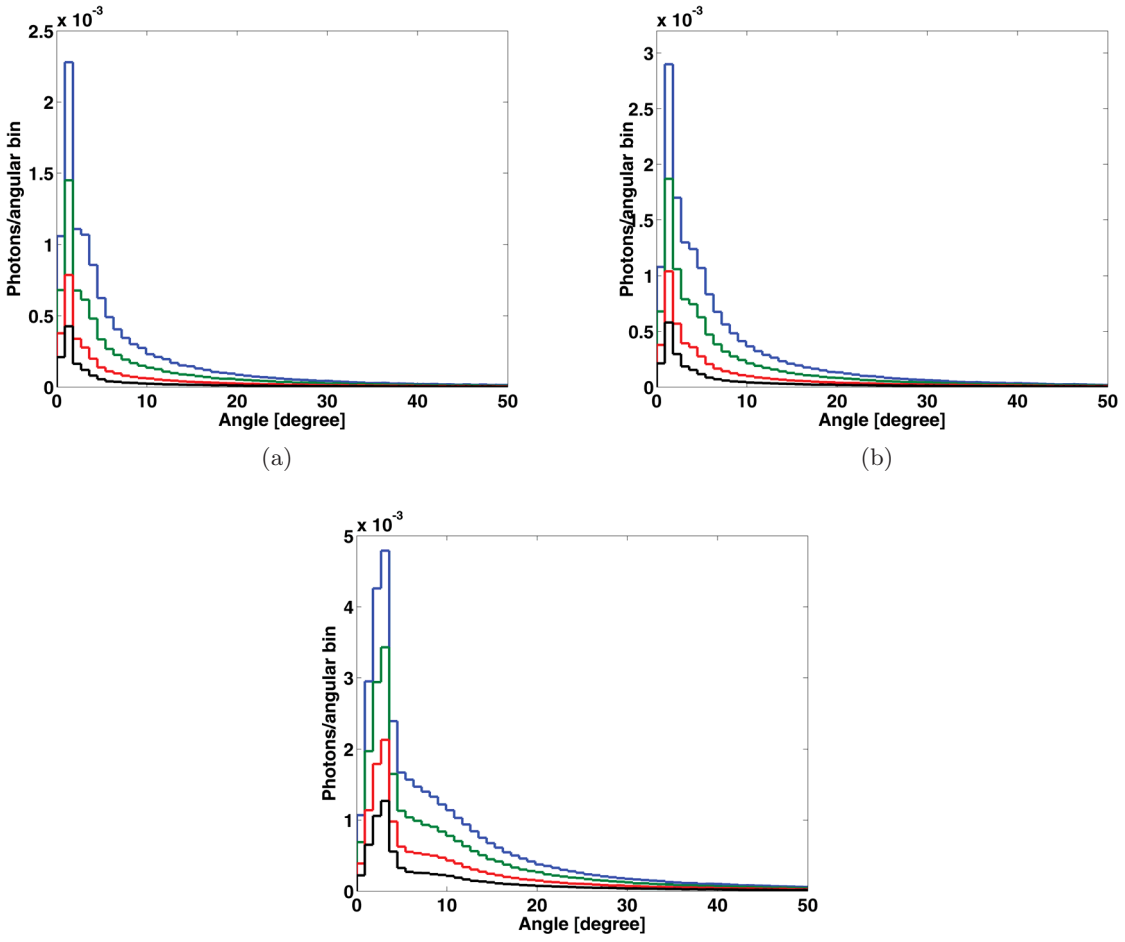

Figure 4.21.: Angular distribution of contaminant photons for 3 (black), 5 (red), 7 (green) and 9 MeV (blue) at (a) 40, (b) 50 and (c) 100 mm applicators.

Table 4.14.: Angular distribution of contaminant photons resulted from 3, 5, 7 and 9 MeV electron beams at 40, 50 and 100 mm field sizes. θ_p, θ_m and Γ are the most probable angle, the mean angle and the full-width-at-half-maximum, respectively.

Energy (MeV)	App. (mm)	θ_p	θ_m	Γ
3		1.3	4.5	0.9
5	40	1.3	5.4	0.9
7		1.3	5.4	0.9
9		1.3	6.3	0.9
3		1.3	5.4	1.8
5	50	1.3	6.3	1.8
7		1.3	6.3	1.8
9		1.3	7.2	1.8
3		3.1	5.4	2.7
5	100	3.1	6.2	2.7
7		3.1	7.2	2.7
9		3.5	8.1	2.9

4.4.5. Contribution to the depth dose and profile from direct and scattered electrons

The relative contributions of direct and scattered components to the absorbed dose to water have been determined as a function of depth in a phantom simulated in BEAMnrc and DOSXYZnrc.

4.4.5.1. PDD, Low Energies, Ref. vs. Clinical Field

As presented in figs. 4.22 (a) and (b), the contribution of different components to the absorbed dose of the total electrons for low energies at the reference field was in average 42 and 58% for direct and scattered ones, respectively, at the phantom surface (z_0). At the z_{max}, the corresponding contribution was 46.5 and 53.5%, whereas at R_{50}, the contribution of direct electrons was increased to 62% against 38% of scattered ones. At clinical field sizes, however, this contribution changed dramatically, as illustrated in figs. 4.22 (c) and (d). The scattered dose was increased in average 12.5 and 16.5% at the phantom surface and z_{max}, respectively. This pattern was more significant at the depth of 50% dose (R_{50}), where the contribution of scattered component increased in average 21%, compared to the reference field. Furthermore,

the contribution of contaminant photons changed from 0.007% at z_{max} for 3 MeV and 40 mm applicator to 0.040% at z_{max} for 5 MeV and 100 mm applicator.

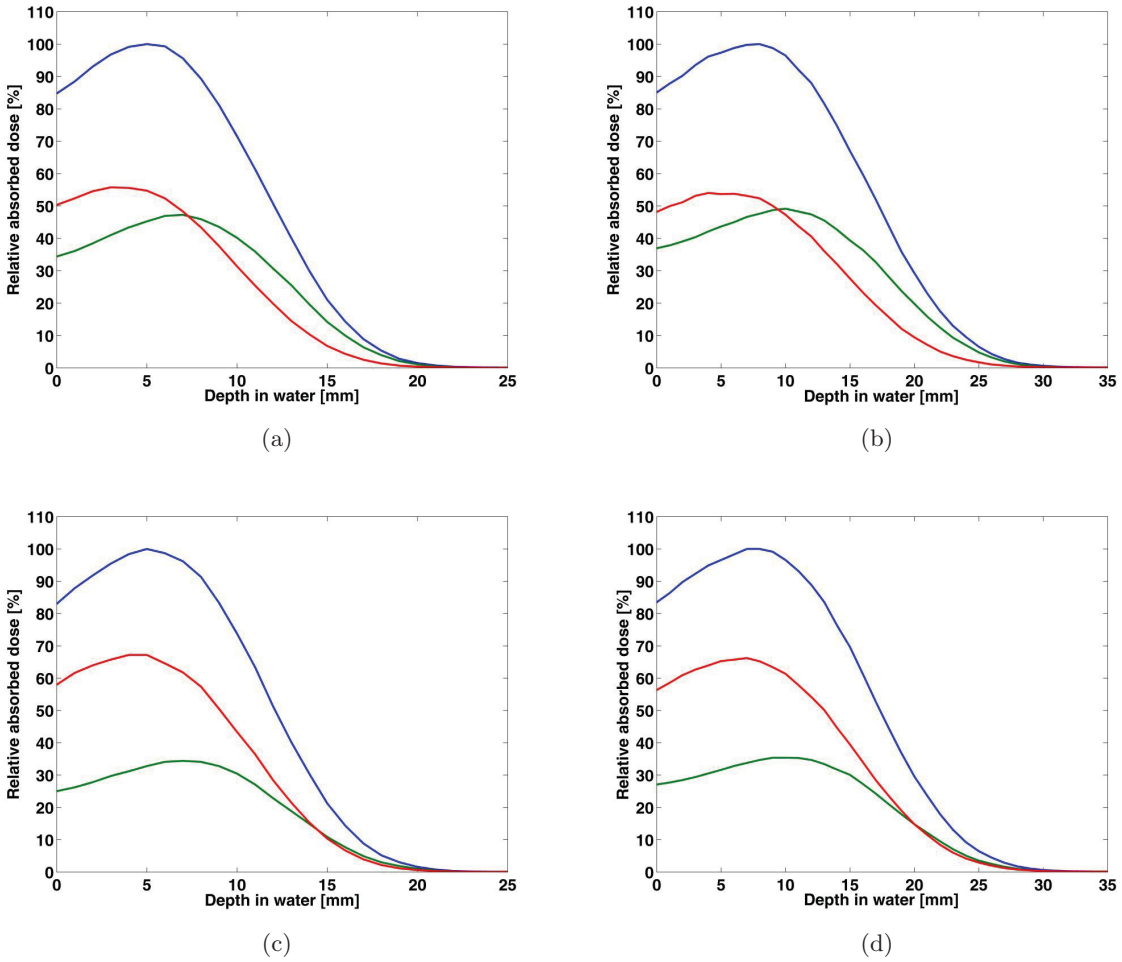

Figure 4.22.: Relative depth dose distribution of total (blue), direct (green) and scattered (red) components for low energies (3 and 5 MeV electron beams) at, (a) and (b), 100 mm and, (c) and (d), 50 mm field sizes. The results are reported as a function of depth in water.

4.4.5.2. PDD, High Energies, Ref. vs. Clinical Field

Figure 4.23 shows the PDD curves obtained for high energies at a clinical filed (50 mm) and the reference field. The absorbed dose at the clinical field due to the scattered electrons was increased in average 18 and 20% at the phantom surface and z_{max}, respectively, compared to the reference field. The corresponding raise was approximately 23% at R_{50}. The contribution of direct electrons was hence decreased correspondingly. The contaminant photons did not contributed significantly (between 0.02 and 0.06%) at different depths in water.

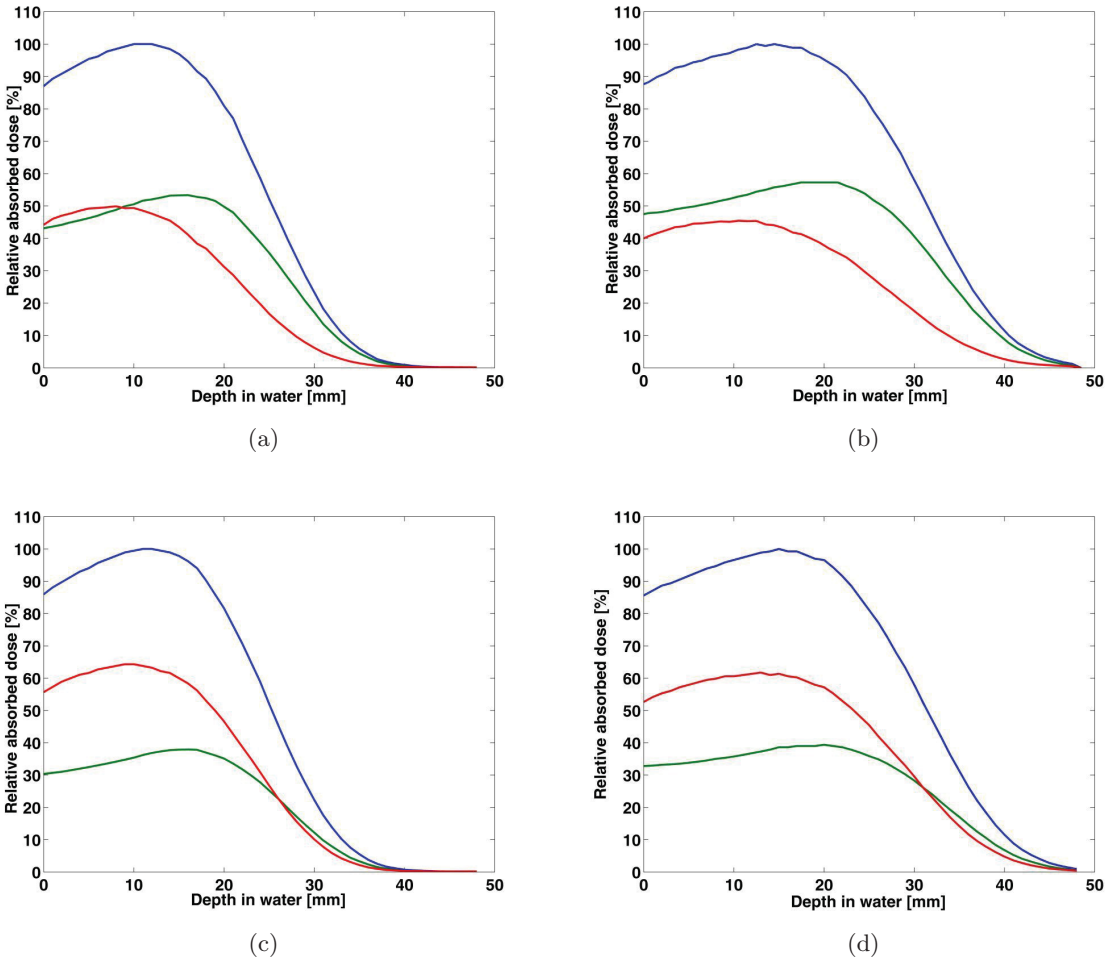

Figure 4.23.: Relative depth dose distribution of total (blue), direct (green) and scattered (red) components for high energies (7 and 9 MeV electron beams) at, (a) and (b), 100 mm and, (c) and (d), 50 mm field sizes. The results are reported as a function of depth in water.

4.4.5.3. Profile, Low Energy, Ref. vs. Clinical Field

Fig. 4.24 illustrates the profile distributions of low energies at different fields which refer to the water surface (z_0), depth of maximum dose (z_{max}) and depth of 50% dose (R_{50}). On the one hand, regarding the reference field, the calculated values of the field size were deviated in average +2% from the expected value (100 mm) at different depths of calculation. In this case, the penumbra increased 4 mm moving from water surface towards the R_{50} crossing through the z_{max}. The direct electrons lost 9% of their fluence around the field edge at larger depths. The scattered electrons, however, showed a more significant change in the profile distribution at larger depths. An inhomogeneity of about 12% was observed on the water surface for this component

which was mainly due to the increased peak around the applicator wall. This inhomogeneity was decreased at larger depths and reached almost 5% at R_{50}. The large inhomogeneity of the scattered component, as shown in fig. 4.24, influenced the profile distribution of total electrons, especially on the water surface.

With regards to clinical applicator, on the other hand, it was observed that the calculated values of the field size were deviated in average +3% from the nominal value at all three depths. Furthermore, moving from the phantom surface towards the larger depths caused an increase in the values of penumbra up to 3 mm. Regarding the inhomogeneity of electron components at different depths, a similar but less significant tendency also emerged in the clinical field. At this field, the inhomogeneity of the scattered electrons was decreased from 7% at water surface to 2% at the R_{50}.

4.4.5.4. Profile, High Energy, Ref. vs. Clinical Field

The calculated field sizes for the reference applicator deviated +3% from the nominal value, as shown in figs. 4.25(a-f). Furthermore, the penumbra was changed from 6 mm at the water surface to 16 mm at R_{50}. This is higher than the obtained values for low energies. At reference field, on the one hand, the direct electrons lost their fluence around the field edge remarkably (about 30%) compared to the value on the central axis, moving from the water surface to the depth of R_{50}. On the other hand, the scattered component had larger inhomogeneity on the water surface (around 15%), which was decreased to 6% at the larger depth of R_{50}. A great loss of homogeneity was also observed for the total electron component, mainly at R_{50}. Regarding the clinical field of 50 mm, +4% deviation was resulted comparing the calculated field size and the expected one, whereas the penumbra values were the same as for the reference field.

4.4.6. Uncertainty analysis

The uncertainty regarding the results of this chapter could be valued as 3.1% corresponding to the uncertainty of the Monte Carlo model used for dose calculation, as described in section 4.2.1. This value must be accounted for the calculation of energy fluence distribution, planar fluence, mean energy, angular distribution, depth dose distributions and off-axis profiles.

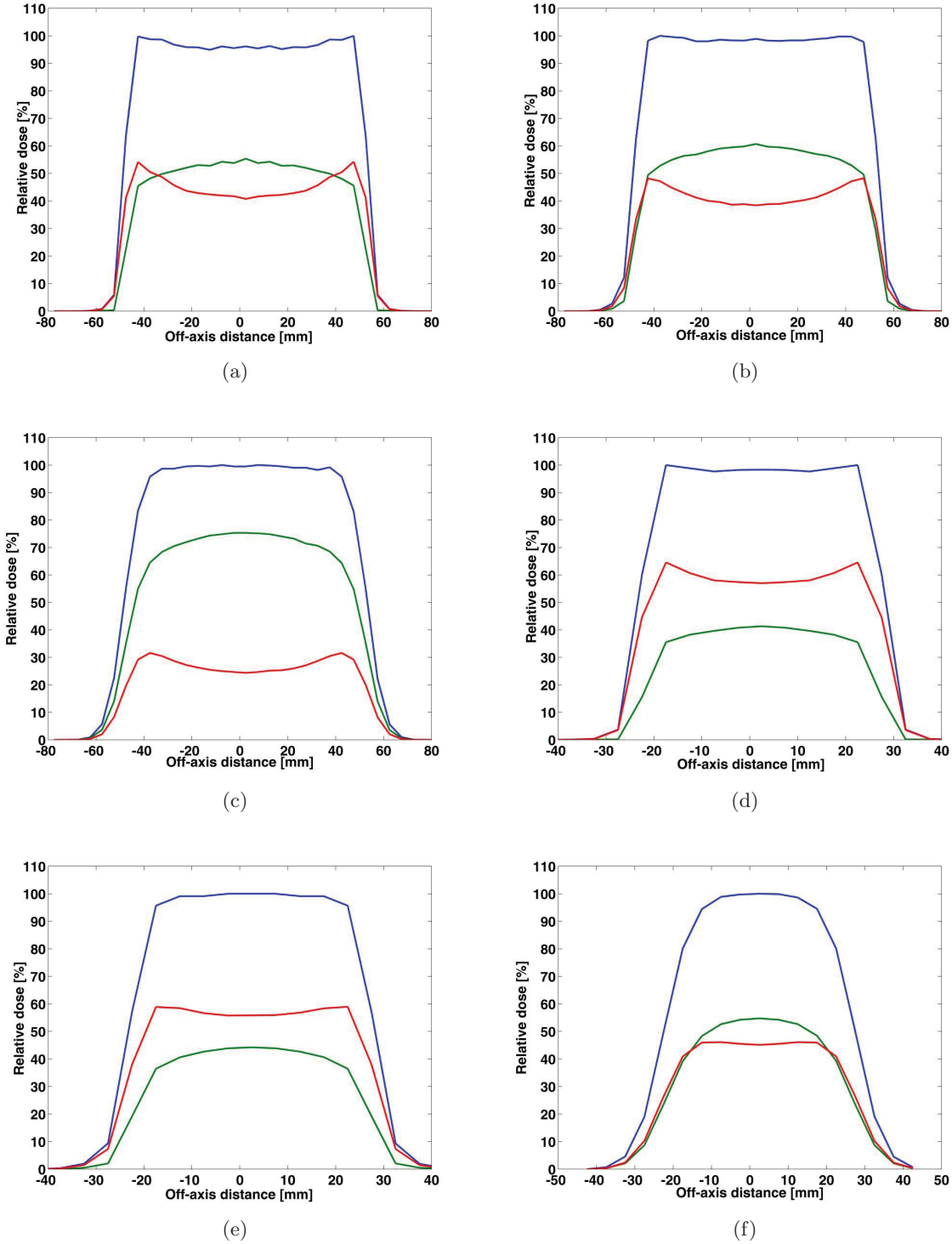

Figure 4.24.: Profile distribution corresponding to low energy of 5 MeV as a function of off-axis distance. The results contain the contribution of direct (green) and scattered (red) electron components to the profile of total electrons (blue) at different depths in water. (a), (b) and (c) refer to profile at z_0, z_{max} and R_{50}, respectively, for 100 mm applicator diameter and the corresponding profiles at 50 mm field size are shown in (d), (e) and (f), respectively.

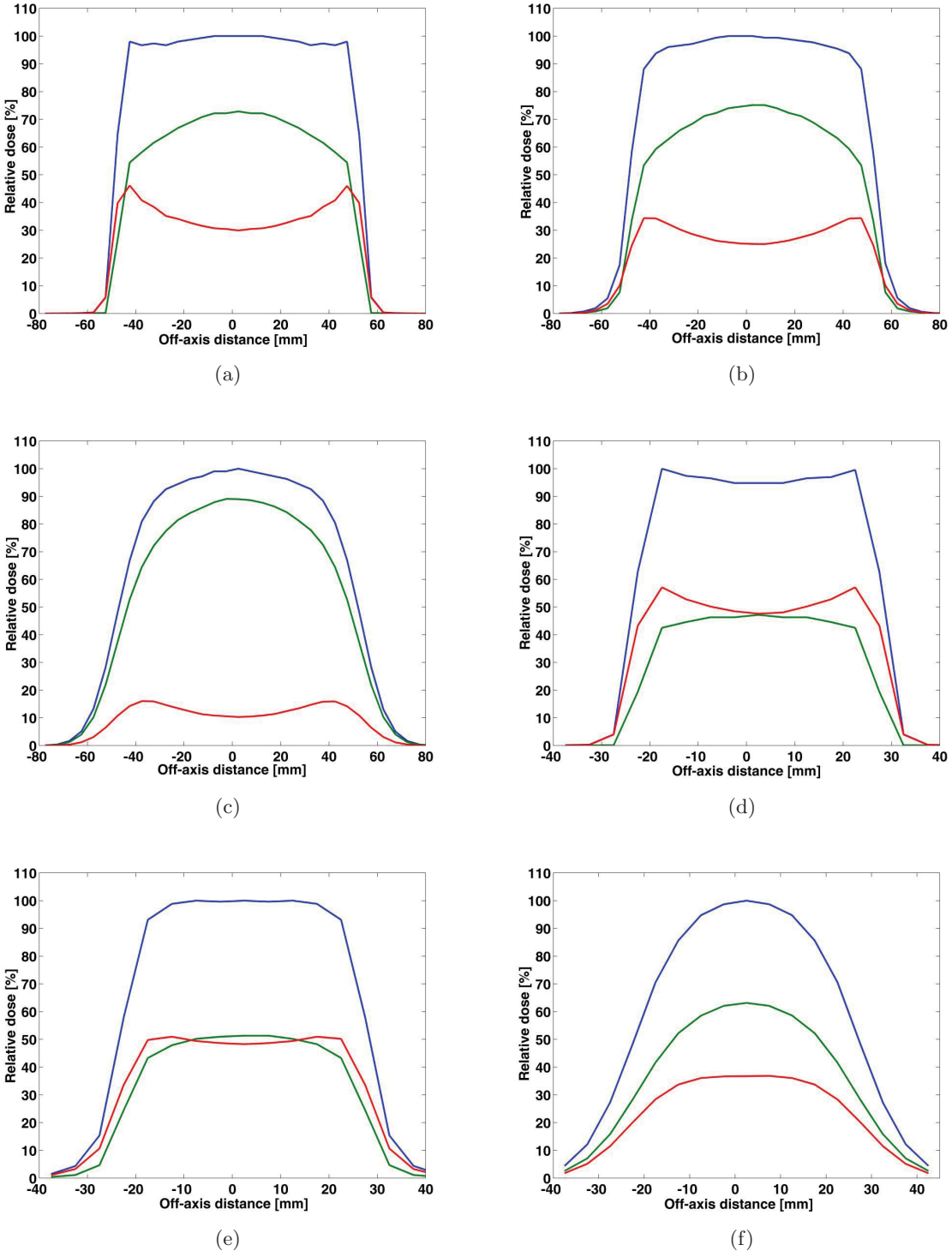

Figure 4.25.: Profile distribution corresponding to high energy of 9 MeV as a function of off-axis distance. The results contain the contribution of direct (green) and scattered (red) electron components to the profile of total electron (blue) at different depths in water. (a), (b) and (c) refer to profile at z_0, z_{max} and R_{50}, respectively, for 100 mm applicator diameter and the corresponding profiles at 50 mm field size are shown at (d), (e) anf (f), respectively.

5. Discussion

5.1. Ion recombination correction factor

During the past few years some efforts have been expended to determine the ion recombination correction factor k_s for different types of ion chambers using high dose-per-pulse electron beams of dedicated IOERT linacs. These studies have been carried out using both standard methods such as the TVA method reported in the TRS-398 protocol, the Jaffé method or recently suggested models called Boag's modified expressions [11, 14]. However, not much attention has been paid to determine whether the standard methods deliver acceptable results using an Advanced Markus chamber. Furthermore, detailed investigation focusing on medium dose-per-pulse ranges was necessary to be carried out because of lack of recorded date regarding this issue. The results of the current study contain the comparison of values of ion recombination correction factors $(k_s)_w^{ref}$, $(k_s)_{th}^{B'}$, $(k_s)_{th}^{B''}$, $(k_s)_{th}^{B'''}$, $(k_s)_{th}^{jaff}$ and $(k_s)_{th}^{TVA}$ obtained by different methods reported in the literature [11, 15] and performed under defined conditions.

The results shown in figure 4.1 extend those of Cella et al. [15], confirming that for 7 and 9 MeV electrons the dose-rate value increases almost linearly when the applicator diameter decreases. Furthermore, Monte Carlo calculations performed in this thesis at higher energies (7 and 9 MeV) showed that with decreasing applicator diameter the contribution of scattered electrons to the calculated dose at z_{max} and R_{50} increased, which consequently led to an increase of the dose-per-pulse value (see subsection 4.4.5). This trend was not observed for 3 and 5 MeV electrons in which most of the energies are transferred by scattered electrons. Based on the Monte Carlo simulation presented in section 4.4.5, it is resulted that at lower energies the contribution due to scattered electrons at z_{max} for low energies is lower (4%) than the corresponding value obtained for higher energies. That could influence the output of the beams and may be the reason for the constancy of dose-per-pulse with decreasing the applicator diameter which was also shown by Fantini et al. [17]. Further discussion including the influence of this phenomenon

on dosimetric parameters is given in section 5.3 where the output factor is discussed.

Figure 4.2 demonstrates the deviation of different theoretical models ($(k_s)_{th}^{B'}$, $(k_s)_{th}^{B''}$, $(k_s)_{th}^{B'''}$ and $(k_s)_{th}^{TVA}$) from the reference value ($(k_s)_w^{ref}$) as described in sections 3.3.2 and 3.3.7. The average deviation between $(k_s)_{th}^{B'}$ and $(k_s)_w^{ref}$ was about -1.5% and the analogous average deviations for $(k_s)_{th}^{B''}$ and $(k_s)_{th}^{B'''}$ were slightly larger, at -2.1% and -1.9%, respectively. Considering the large uncertainty of the $(k_s)_{th}^{'}/(k_s)_w^{ref}$ values (3%), the results from the three Boag's expressions are all within the tolerance limit of 3%. These results are not directly comparable with the findings of previous authors because they were performed for different chambers (Exradin A11, PTW Roos, etc.) and different dose-per-pulse ranges (higher than 40 mGy/pulse), but they are similar to the results published by Cella et al. [15]. Based on their study, the average deviations of $(k_s)_{th}^{B'}$, $(k_s)_{th}^{B''}$ and $(k_s)_{th}^{B'''}$ from $(k_s)_w^{ref}$ obtained by applying Laitano's method at dose-per-pulse values from 31 to 70 mGy/pulse for the Advanced Markus chamber were -1.1%, -1.8%, and -1.4%, respectively.

The corresponding deviation of calculated k_s values from reference values using Di Martino's method was -0.9% [14]. Even when the absolute deviation of each model at each dose-per-pulse level is considered, most of them are within the tolerance level (see table 4.1). This tendency was also observed in the work of Cella et al. [15] where considering the large uncertainty (combined uncertainty of about 6%) at dose ranges of 31 to 70 mGy/pulse most of the calculated k_s values derived from Laitano's [11] and Di Martino's [14] method for the Advanced Markus and the Markus chamber are within the given uncertainty range. Therefore within the applicable dose-per-pulse range of the NOVAC7, all three methods can be used for the calculation of the k_s factor.

All Boag's models show an underestimation of the k_s values (see table 4.1 and figure 4.2) which was also observed by Cella et al. [15]. They reported an average underestimation corresponding to the three models of 2.3% and 1.3% for Markus and Advanced Markus chambers, respectively. The reason for this may be the fact that the theoretical models proposed by Boag et al. investigated in this study are strongly dependent on the type of chamber used. It means that, changing the electrode distance (d) and chamber's operating voltage (V), affect the charge density distribution, free electron fraction (p) and the parameter, μ (see subsection 3.3.6). Therefore, none of these models are universal solutions for all types of gas-filled ionization chambers utilized under high dose-per-pulse electron beams. For a more accurate prediction of ion recombination correction factor future work should focus on optimizing Boag's models for each specific chamber

considering their geometrical and operational individuality.

The results in table 4.1 show the absolute deviation between $(k_s)_{th}^{TVA}$ and $(k_s)_w^{ref}$ values. The deviation increases with increasing dose-per-pulse value and reaches a deviation of +2% at 35 mGy/pulse, which is also within the tolerance level of ±3%. Increasing the dose-per-pulse rate to 42 mGy/pulse, the deviation increases up to +4.2% which is beyond the tolerance level. This high deviation at higher dose-rate values was expected because of avoiding the influence of free electron fraction for determination of $(k_s)_{th}^{TVA}$. As previously mentioned, $(k_s)_{th}^{TVA}$ ignores the free electron fraction, p, which is a remarkable disadvantage at higher dose-per-pulse region. It means that, for a non-zero value of p, increasing the dose-per-pulse which causes larger value of u (see eq. 2.46), has a significat influence on the k_s factor. $(k_s)_{th}^{TVA}$ can not then deliver approperiate results at higher dose rate values. Although there are not sufficient experimental data concerning $(k_s)_{th}^{TVA}$ in the dose-per-pulse range investigated in the current study for the Advanced Markus chamber, Laitano at al. have reported data for some other chambers (Capintec PS-033, Exradin A11, PTW Roos, NACP02, Markus, and Wellhöfer PPC 05) at the 40 mGy/pulse rate [11]. They showed that $(k_s)_{th}^{TVA}$ value could deviate from the reference value by up to +8% and +11% (in their case $(k_s)_{Frick}^{ref}$ obtained by Fricke dosimeter) for the Markus and Exradin A11 chamber, respectively.

The relative lower absolute deviation obtained for $(k_s)_{th}^{TVA}$ in the current study may be due to the fact that the electrode separation in the Advanced Markus chamber is half that of the Markus and Exradin A11 chambers investigated by Laitano et al. and consequently the effect of recombination in the sensitive volume of the Advanced Markus chamber is significantly reduced. As reported by Laitano et al., decreasing the chamber electrode distance from 2.4 to 0.6 mm would lead up to an 11% improvement of the results obtained by the TVA method [11]. Regarding the minor deviation of the $(k_s)_{th}^{TVA}$ values, the TVA method proposed by the TRS-398 protocol could be used for the determination of the ion recombination correction factor up to a dose-per-pulse value of 35 mGy/pulse.

The absolute deviation between the $(k_s)_{th}^{TVA}$ and k_s values resulting using Laitano's approach in eqs. (3.11), (3.12) and (3.13) is negligible at lower dose-rate values (about 0.3%) and increases up to around 7% at a dose rate of 42 mGy/pulse (see table 4.2). Similar findings has been also reported by Laitano et al. for a different chamber [11]: They observed a maximum deviation of 0.1% (between $(k_s)_{th}^{B''}$ and $(k_s)_{th}^{TVA}$) at 0.1 mGy/pulse and a maximum deviation of 30% at 70 mGy/pulse for the Exradin A11 chamber with an electrode distance of 2 mm at an operating

voltage of 300 V. The free electron fraction is not integrated in in the $(k_s)_{th}^{TVA}$ determination in contrary to eqs. (3.11), (3.12) and (3.13). The influence of this approximation is not remarkable at low dose-per-pulse values because in this condition u is small and thus the deviation between TVA and Boag's modified expressions was not significant. At larger values of dose-per-pulse, which means the higher values of u, TVA could not predict the charge distribution in the chamber appropriately which consequently resulted to the overestimation of recombination.

Table 4.2 shows the deviation of different ion recombination models from the reference value for the prediction of k_s as a function of the operating voltage of the chamber. These results are consistent with those of Laitano et al. [11]. As the chamber's operating voltage increases, the difference between the values of the four recombination models $(k_s)_{th}^{B'}$, $(k_s)_{th}^{B''}$, $(k_s)_{th}^{B'''}$ and $(k_s)_{th}^{TVA}$) decreases. This difference depends on the change of the u value when the voltage varies [11]. As expected, decreasing u in all four expressions (see eqs. (3.11), (3.12) and (3.13)) led to the same results. On the other hand, the quantity u is proportional to $1/V$ (see eq. (2.46)). Hence, it is obvious that as the value of V increases these four expressions tend to coincide with each other.

Following the data presented in figure 4.3, a +1.2% deviation from the reference value was concluded for $(k_s)_{th}^{jaff}$ at 27 mGy/pulse. A maximum deviation of 2.8% was observed between the $(k_s)_{th}^{jaff}$ and k_s values resulting from Boag's expressions, particularly between the $(k_s)_{th}^{jaff}$ and $(k_s)_{th}^{B'''}$ values. Laitano et al. obtained deviations of up to 6% between the $(k_s)_{th}^{jaff}$ and $(k_s)_{th}^{B'''}$ values at 70 mGy/pulse for the Exradin 11 chamber with a 2 mm electrode distance [11]. On the one hand, these values could not be directly compared with present results because they are obtained for different chamber. On the other hand, different absolute values of $(k_s)_{th}^{jaff}$ could be the result of different measurement conditions, especially the electrode distance of the applied chamber and the dose-per-pulse value investigated [100]. As reported by Burns and McEwen, a difference in the parallel-plate separation of 0.16 mm causes changes in the ion recombination factor of up to 8% [5]. Furthermore, a dose-rate difference of 10 mGy/pulse results in a difference of up to 5% in the value of the ion recombination correction factor [11]. The use of the Jaffé plot has shown to give appropriate result. The result represented here is only valid for dose-per-pulse value of 27 mGy/pulse. In clinical application it may be also possible that higher values of dose rate ($\geq$30mGy/pulse) are applied. The investigation on the linearity of Jaffé diagram and feasibility of this method for k_s determination at higher dose-per-pulse values would be therefore beneficial [101].

According to the expression corresponding to absorbed dose in water, eq. 3.1, ion recombination correction factor k_s has a direct influence on the dose value. In clinical application, 40 and 60 mm applicators combined with 5, 7 and 9 MeV beams have been frequently used. As it is shown in table 4.1, ignoring this factor in determination of absorbed dose may result to underestimation of delivered dose of about 3%. The results of this investigation are therefore highly significant for determination of absorbed dose delivered to patients in IOERT application.

5.2. Monte Carlo simulation and commissioning of the NOVAC7

The initial electron beam properties are often the poor known parameters of a linac. This includes the energy spectra for different energies. The spectra can hardly be measured directly, unless fundamental changes are performed to the accelerator. Hence, the adjustment of the spectra is mostly carried out iteratively in order to match calculated with measured depth-dose curves. Monoenergetic sources or Gaussian energy distributions are frequently used. In this work, Gaussian energy spectra were adjusted to the depth-dose and transverse-dose measurements. The electron spectrum was determined by the matching of calculated and measured data so that the 3 %/3 mm tolerance level was achieved and also the root mean square deviation of about 2 % between measurement and simulation of depth dose and profiles for all energies and applicators were reached.

The results show that the energy spectrum of the initial beam has great influence on the depth–dose distribution. Particularly varying the most probable energy of Gaussian distribution influences the R_{50} value directly. Since the value of the most probable energy affects the energy of electrons incoming to water, the beam quality index (R_{50}) increased linearly at larger values of that. Varying standard deviation of the Gaussian energy spectrum affects the dose gradient in 80% to 10% region of PDD. This parameter represents the distribution of low and high energy particles in the spectrum. The larger this value, the broader the electron final spectrum.

Furthermore, OAPs were calculated by modifying the source geometry (i.e. radius and divergence of the initial electron beam) to obtain the best conformity with experimental data. Moreover, the lateral dose profiles were unaffected by the energy spectrum of the initial beam. Thus, the only possibility for a major change of the lateral dose distribution was to modify the accelerator geometry. It was observed that the sensitivity of R_{50} to changes in standard deviation of the initial Gaussian distribution was insignificant. Similarly, it was revealed that the depth-dose distribution was independent of the geometrical properties of the initial beam. The change of source radius and its divergence influence the symmetry or beam direction but could not affect the R_{50} value because, through this change the most probable energy of the distribution which is responsible for the variation of R_{50} stays constant.

The high dose in build-up region was calculated by considering a continuous low energy tail in the spectrum. This part was changed iteratively until a good match (3%-3mm) between calculation and measurement was achieved. Due to high mass collision stopping power, low

energy electrons deposit most of their energy near the water surface (build up region) and therefore do not have sufficient energy to reach the larger depths in water. As it is seen in fig. 4.4 the low energy region was resulted to be individual for each energy. In particular, using an energy spectrum for the initial beam instead of a monoenergetic beam made it possible to reproduce the unusual high surface dose typical of the experimental PDD curves for the NOVAC7 beams.

As it is shown in table 4.5, with an exact design and modeling of all components and matching them to the measurements, the spectrum resulted for different energies was independent of the applicator diameter. The energy spectrum should be independent of the field size as it will be discussed in section 4.4.1 and only the contribution of direct and scattered electrons is influenced by changing the applicator diameter. The output factor is expected to change which is explained in section 5.3. The difference between the mean energy E_{mean} and the most probable energy E_p is due to the presence of a low-energy tail in the energy spectrum. As stated by the manufacturer, this low-energy component is permanently present as no filtering system or bending magnet are available in this type of autofocusing linacs.

In this work, the FWHM of the Gaussian distribution of the initial energy was greatly more than that of conventional linacs and was about 22% of the most probable energy. In the work of Björk et al., the change of primary electron radiation for SL25 (Philips/Elekta) conventional linac was discussed [18]. It was shown that, for this linac the FWHM of more than 10% of the most probable energy is not expected. The intraoperative treatment field however contains a larger amount of scattered electrons, which leads to a broader energy spectrum as well as a wider angular distribution of electrons at the phantom surface. Furthermore, the IOERT spectra contain a larger amount of low-energy electrons compared to the conventional spectrum. In consequence, the spectrum is broadened and the mean energy is decreased.

The present results show considerable differences in the energy and angular distributions even if compared with other IOERT beams as those analysed by Björk et al. [24]. The collimation systems considered in this work are actually different from each other and this explains why the energy and angular distributions change under these two experimental conditions. Considering that four energies may be chosen using flat or bevelled applicators (0, 22.5° und 45°), with eight possible diameters, a thorough accelerator commissioning requires a total of 84 dose distributions and OF measurements. Using this virtual model in the future will significantly reduce the measuring expenditure for clinical dosimetry and commissioning. Also other challenging issues

such as determination of lung dose in intraoperative radiation of breast, the development of the shielding plates for intraoperative application behind the target region or dosimetric evaluation of other accessories in radiation direction, will be possible. The results of present work supports the conclusion that only a few measurements are required to obtain dose distributions for all other geometries. Therefore, MC simulation as a predictor of dose distribution in all geometry setups proved to be a good tool for physicists in commissioning the dedicated IOERT linacs.

Moreover, lack of Monte Carlo based treatment planning system for IOERT reduces the accuracy of dose estimation of electron radiation delivered to the tumour bed or absorbed by organ at risks such as lung and ribs. The present model can be used to make a Monte Carlo based planning system for precise dose calculation in the patient. In addition, the determination of chamber perturbation correction factors irradiated with high dose-per-pulse electrons is not thoroughly investigated yet (see section 2.7). The Monte Carlo based model of the NOVAC7 electron beams could be utilized to study them with high precision. Due to importance, complexity and time-needed, above mentioned investigations will be treated in future separately.

5.3. Stopping power ratios and output factors

The calculated and measured OFs match within the combined uncertainty. The relative differences between calculated and measured OFs (see table 4.8) were maximally 3% but only 1.8% in average. The high deviation occurred for small filed sizes and may have two reasons. On the one hand, for small applicators, due to numerous interactions of electrons with the applicator wall a precise Monte Carlo treatment of the whole interactions involved with larger uncertainty. On the other hand, absorbed dose measurement for small applicators is more inaccurate than for the larger applicators mainly due to measurement setup and the influence of greater dose-per-pulse at smaller fields on the ion recombination correction factor which affects the collected signal of the chamber (see section 4.1). This difference is similar to the results obtained by Pimpinella et al. where an average deviation of 1.4% for 7 and 9 MeV IOERT electron beams was found [22].

It can be seen in table 4.8 that the OF values grow with decreasing applicator diameter, which is in contrary to the behavior of other linacs [21]. The dependence of the OFs on the applicator diameter is different in the NOVAC7 beams with respect to other linacs because of particular scatter effects due to its applicator geometry. Contrary to other accelerators, the employed applicators are positioned very close to the exit window and their lengths are exceptionally large. Monte Carlo simulations showed that under such experimental conditions, the ratio electron/cm^2 became greater as the applicator section reduced (see table 4.9, 100-50 mm). This increase of the electron/cm^2 values, hence the electron fluence, causes a larger absorbed dose and consequently a larger OF value as experimentally confirmed.

With regard to applicators with small diameter (e.g. 40 mm), the fluence was surprisingly not grown, but as it is shown in table 4.9, the number of charged particle steps in dose region per initial history was increased. This demonstrates that, although the fluence beneath the applicator was not increased, deposited energy and number of electron interactions which are caused by greater number of scattered electrons in dose region were increased. Nevertheless, the underestimation of the ion chamber measuring OFs is related to the restrictions of using this detector for IOERT beam dosimetry. As previously stated by Björk et al., the electron fluence perturbation correction factor of the ion chamber changes for the given and the reference field [21]. The constancy of this factor might be a proper assumption for broader electron beams, but not necessarily for IOERT fields which are substantially influenced by scattered electrons. This approximation will further give raise to the uncertainty related to dosimetry with ionization

chambers in degraded electron beams. Measuring the OFs with gel dosimetry, as reported by Pimpinella et al., has shown that higher values of output factors could be resulted [22]. Under these conditions, the output factors could be considered as an indication that the NOVAC7 IOERT electron beams have been properly simulated.

Considering our previously stated results and the combined uncertainty of ±2% in $s_{w,air}$ determination, a good agreement was found with the TRS-398 dosimetry protocol at water surface and z_{ref}. A maximum deviation of -0.3% at water surface and -0.7% at z_{ref} occured. This difference is nearly identical with the results of Pimpinella et al. [22]. In their study, the corresponding deviation has been reported to vary in the range of 0.3%-0.0% and 0.2%-0.4%, respectively. The minor discrepancies between Monte Carlo calculation and TRS-398 results are due to the fact that the presented $s_{w,air}$ values are calculated for a dedicated IOERT linac (namely the NOVAC7), whereas the Monte Carlo generated values in TRS-398 are based on a variety of linac types.

Moreover, uncertainty in determining the R_{50} from measured PDD curves may also lead to differences in the calculated $s_{w,air}$ values. According to the data in table 4.12 which presents the difference between simulation and those of TRS-398 for 9 MeV and different applicator diameters, the level of agreement ensures that an appropriate phase-space description of different electron beams has been achieved. This result is in consensus with a previous study carried out by Pimpinella et al. [22]. According to their results, a difference between +0.0% and +0.2% was obtained comparing $s_{w,air}$ values determined using SPRRZnrc Monte Carlo code and TRS-398 protocol for 9 MeV considering 40, 60 and 80 mm applicators at z_{ref}. It should be noted that ±2% uncertainty in electron beam simulation was also considered in their investigation. There are few data regarding other energies (3, 5 and 7 MeV) and lower applicators (80 mm and lower) which makes the comparison difficult. However, the results regarding $s_{w,air}$ are consistent with literature at similar conditions [22].

Furthermore, it is of great importance to investigate how the $s_{w,air}$ values vary at different field sizes, as it is shown in table 4.12. The variation was insignificant. A difference within 0.2% for the $s_{w,air}$ values at different field sizes is an acceptable tolerance considering the combined uncertainty of the $s_{w,air}$ value in this study. There are not enough data to compare these results directly but Björk et al. have performed similar comparisons for 6 and 12 MeV IOERT electron beams for 105 × 105 mm^2 against 20 × 20 mm^2 [21]. At corresponding depth of calculation (z_{ref} = 14.5 and 18 mm for 7 and 9 MeV, respectively), they have reported 0.5 and 0.6% un-

derestimation of stopping power ratios in 20×20 mm^2, compared to 105×105 mm^2 for 7 and 9 MeV, respectively. The corresponding variation of $s_{w,air}$ in their study was within +0.2%. A tolerance level of ±2% has been reported for their measured data.

The reason for the difference between our results and the data published by Björk et al. might be due to the use of different energy and the very small field size. Because of dimension of the applying field of 20×20 mm^2, stopping power ratios were affected due to larger amount of low-energy scattered electrons at this field size, which will decrease the mean energy at z_{ref} (6 mm) and consequently increase the $s_{w,air}$ values. Furthermore, the results of this work, shown in table 4.12 agree with those of Pimpinella et al., confirming that for 9 MeV, a difference of about 0.2% was observed comparing SPRRZnrc based calculated $s_{w,air}$ values for 100 and 40 mm applicator at specific depths in water. There are no data provided regarding lower energies for further verification.

Although the deviations between the TRS-398 $s_{w,air}$ values and the SPRRZnrc $s_{w,air}$ values were not remarkable on water surface and z_{ref}, the difference between them increases with depths in water. However, this deviation increases slightly in larger depths and the maximum deviations, within 1.5%, are only at depths greater than R_{50}. The differences are particularly 1.0, 1.3, 1.4 and 1.2 % beyond R_{50} for 3, 5, 7 and 9 MeV, respectively. Previous works made by Björk et al., Pimpinella et al. and Mihailescu et al. have also shown deviations more than 1% at larger depths. The electron energy spectrum changes at larger depth in water so that the results calculated based on TRS-398, which are based on electron spectrum of conventional linacs deviate from that of the NOVAC7 electron spectrum especially around z_{ref} and R_{50}.

As discussed in section 4.4, the scattered electrons contribution to the energy spectrum, fluence and mean energy changes significantly which affect the depth dose and off-axis profiles remarkably. Such variation influences the mass stopping power ratios at larger depth in water and causes such contradiction as can be seen in fig. 4.6. For the other electron beams (3, 5 and 7 MeV), rather similar deviations of SPRRZnrc-based calculated $s_{w,air}$ values from the corresponding values resulted using TRS-398 protocol were obtained as a function of depth (see fig. 4.6).

The results corresponding to OFs demonstrated that the Monte Carlo model discussed in section 5.2 could be able to simulate electron beams produced by the NOVAC7 accurately. In addition, based on the eq. 2.39, determination of $s_{w,air}$ values were necessary for absorbed dose determination. Therefore, the variation of this parameter as a function of depth was carefully

investigated under non-reference condition. The results of present study demonstrated that ignoring this effect caused up to 1.0 and 1.5% overestimation of the delivered dose to the patient at z_{ref} and R_{50}, respectively. For clinical patient dose delivery, this dose uncertainty may not be significant but for accurate dosimetry they are mandatory to be considered.

5.4. Scatter and contamination analysis

5.4.1. Energy fluence

It was mentioned in subsection 4.4.1 that the energy spectrum of electrons did not change remarkably with reducing of the field size. This occurs because changing the field size must influence only the spatial distribution as well as the distribution of the scattered and direct electrons (see figs. 4.7 and 4.8). These results are consistent with the calculated values published by Pimpinella et al. [22]. They claimed that the most probable energy values for 9 MeV resulted for smaller applicators deviated 0.5% from the corresponding value obtained for the reference field. In this study, a maximum corresponding deviation of 2% was found. This difference is because, on the one hand, the energy fluence characteristics of each NOVAC7 linac are not completely identical. They could differ from model to model. On the other hand, the tolerance level Pimpinella at al. reported for their simulation ($\pm 2\%$) was lower than the value accepted for this investigation ($\pm 3.1\%$). Furthermore, they considered a long term reproducibility of $\pm 1.5\%$, whereas a corresponding value of at least $\pm 2.5\%$ was taken into account in this investigation.

The significant difference between the low and high energies at the reference field was that, the relative contribution of the scattered electrons at low energies is larger than that of higher energies. The reason could be the higher energy loss of the low energy electrons interacting with the applicator and the adaptor inner wall, compared to the high energy ones. It can be also because mainly the electrons in the low energy tail of the high energy spectrum make interactions with the field edge, rather than the higher energy part of the spectrum. A variation was observed in the relative energy fluence values of the scattered electrons at the low and high energies for clinical applicators. It might be due to the fact that each scattered electron at the low energies undergoes more scatter events with the field edge, rather than the scattered electrons at the higher energies. This may lead to a dominant percentage contribution of scattered component to the energy spectrum at 3 and 5 MeV beams.

The relative contribution of the scattered electrons increased 30% at the clinical fields compared to the reference field. This might be explained as the large part of electrons of the energy spectrum at the clinical fields participated in the scatter process compared to those of the reference field. This significant raise could explain why the output factor increased at the clinical fields compared to the reference field as discussed previously (see subsection 4.3.1). Moreover, the scattered component shifted towards the higher energy regions in the clinical fields, contrary

to the reference field. This might be caused by participation of greater fraction of electrons in the interactions with the applicator wall at the clinical fields. As a result, the energy loss of an individual electron at each interaction could be lower, compared to the reference field.

5.4.2. Fluence

The electron total fluence at the reference field increased about 240% at 9 MeV, compared to the corresponding value resulted at 3 MeV. A similar behavior was observed among different energies in clinical fields. The reason for this substantial increase is that, the number of particles which cross the unit area per unit time at higher energies of electrons will increase. Since this calculation was performed on the phantom surface beneath the applicator, no influence of interaction in the water phantom was recorded.

The total fluence of electrons at a particular energy around the central axis in the clinical fields increased up to 57%, compared to the corresponding value of the reference field. This must be due to the dramatic increase of the fluence of the scattered electrons when decreasing the applicator diameter, as it can be seen in figs. 4.10, 4.11 and 4.12. For example, the relative contribution of the scattered electrons was increased 26% with decreasing the field size from 100 mm to 40 mm at 9 MeV beams (see figs. 4.10(d) and 4.12(b)). This might be a further reason for the increase of the output factor at the smaller field sizes.

As noted in subsection 4.4.2, the contribution of the direct and the scattered electrons on the total fluence was changed depending on the applied energy moving from central axis towards the applicator wall. With respect to the fluence of direct electrons, the contribution of the scattered component was remarkably lower on the beam axis but increased significantly near the field edge. This is mainly due to the dramatic increase of the interaction events occurred inside the therapeutic beam between electrons and the applicator wall. Particularly, with decreasing the applicator diameter from 100 mm to 40 mm, the contribution of the scattered electrons to the total fluence around the applicator wall was increased up to 18% at 9 MeV beams, as it is shown in figs. 4.10(d) and 4.12(b). However, the total fluence which is the sum of the fluence contribution of the direct and the scattered electrons had a good uniformity (+2%) in radial distance near the central axis (approximately half the applicator radius).

Additionally, the total photon fluence was increased approximately 29% with decreasing of the applicator diameter and reached its maximum at 50 mm. On the one hand, the bremsstrahlung photons are mainly produced due to the interaction of electrons with the applicator wall. At

higher energies, more energy might be delivered to the released photons and therefore higher photon fluence occurred. On the other hand, the energy loss of electrons near the field edge at clinical fields may be higher compared to the reference field. This could explain why the photon fluence reached its maximum at clinical fields around the applicator wall. In addition, the contribution of scattered electrons increased 18% near the applicator wall which explains the larger photon fluence in this region due to bremsstrahlung production.

Furthermore, although fluence distribution supplies less information about the energy distribution, the substantial increase of the fluence related to the scattered electrons may explain why this component had much higher relative energy distribution than the direct electrons at specific energy levels in the clinical fields. Results of the energy spectrum and fluence at the reference and clinical fields reveal that there is a direct relation between the fluence value of the scattered electrons and their energy fluence distribution at each particular field size.

5.4.3. Mean energy

As reported in subsection 4.4.3, the mean energy of scattered electrons was increased dramatically with decreasing the applicator diameter up to approximately 28%. There might be two reasons for that. Firstly, considering the results regarding the fluence distribution in subsection 4.4.2, the percentage fluence contribution of the scattered electrons was increased 26% around the central axis with reducing the field size from 100 mm to 40 mm. Secondly, the results in subsection 4.4.1 regarding the energy fluence distribution showed that the contribution of the scattered electrons to the energy spectrum at the clinical fields was expanded to the high energy region. Therefore, it can be concluded that due to the increased number of scattered electrons (higher fluence) and their larger energies, their mean energy was increased. Moreover, since the mean energy of the direct electrons did not change significantly and was constant within 2%, this component could not cause the substantial increase of the mean energy of the total electrons.

Moreover, this result helps us to comprehend the increase of output factor, decreasing the field size. Regarding this, it has been demonstrated that there is a direct relation among mean energy, fluence and energy spectrum reducing the field size from 100 to 40 mm. In other words, the higher values of the mean energies caused the larger values of the output factors at smaller fields.

The cause of the inhomogeneity in the mean energy distribution of the direct, scattered and total electrons might be due to the inhomogeneity in the fluence distribution of each component

at specific energy and applicator. For example, a 9% inhomogeneity of the mean energy of the scattered electrons was observed at high energies and the reference field (see subsection 4.4.3). The fluence distribution corresponding to this condition had a 20% inhomogeneity. Therefore, this high inhomogeneity of the mean energy related to the scatterd electrons should be unavoidable.

5.4.4. Angular distribution

Increasing the energy of electrons at the reference field decreased the angular parameters of the total component. This has occured due to the significant change in the values related to the direct electrons. The parameters related to the scatter component did not vary remarkably. The direct electrons at higher energies move in a straightforward direction because of their greater velocity. Therefore, smaller values were resulted for angular parameters of them at higher energies.

These results are similar to the data reported by Pimpinella et al. [22]. On the one hand, at low energy and reference field, they reported the θ_p values of 3.6°, 7.7° and 4° for the direct, scattered and total components which deviate in average 0.5° from the results of this study. On the other hand, the θ_m and Γ values in this investigation differ only 0.8° and 0.9°, respectively, from the corresponding values published in literature [22]. Comparing with the results of other studies, a difference which was within 1° was observed, taking into account different electron components, energies and field sizes. As discussed in sections 5.2 and 5.3, the Monte Carlo model for calculating these parameters was benchmarked by experimental data and therefore these results are reliable.

As it can be seen from fig. 4.21, θ_p reached its maximum at about 3° for the reference applicator and 1.3° at the lower field sizes. This might be caused by reducing the field size more than half. θ_m changed in the range from 4.5° to 8.1°. Changing the applicator diameter from 100 to 40 mm led to a reduction in the θ_m value of 1.3°. This parameter varied also depending on the electron energy and changed 1° with increasing the energy from 3 to 9 MeV at 100 mm applicator. The corresponding change of +0.5° was resulted at clinical fields which is not clinically relevant. The Γ values were the same for different energies and resulted to be 0.9°, 1.8° and 2.7° for 40, 50 and 100 mm applicators, respectively.

5.4.5. Depth dose and profile

Increasing the energy at the reference field of 100 mm led to the reduction of delivered dose by scattered electrons at the phantom surface (approximately 9%). This change was lower at z_{max} and R_{50} (approximately 4%). This can be, on the one hand, due to the lower value of the most probable energy of scattered electrons when increasing the energy compared to direct electrons, as discussed in subsection 4.4.1 and shown in figs. 4.7 and 4.8. However, the electron fluence (see subsection 4.4.2) and mean energy distribution (see subsection 4.4.3) of scattered electrons increased at larger energies.

On the other hand, the stopping power ratio increases moving from water surface towards the larger depths in water, as discussed in section 5.3. Moreover, around the z_{max} and R_{50}, both direct and scattered components undergo multiple scattering caused by elastic and inelastic collisions, as it is known from electron interaction with matter explained in chapter 2. Therefore, both components participate in dose delivery and their difference in dose contribution at z_{max} and R_{50} will be less significant than the water surface.

Considering the results discussed above, the change in the stopping power ratio could be understood. Due to reduction in the most probable energy of the scattered electrons, the direct electrons contribute to the multiple scattering process at larger depths significantly. This causes reduction of the mass stopping power ratio calculated by SPRRZnrc. Consequently, the calculated $s_{w,air}$ values deviate from the values obtained by TRS-398. Regarding this, further investigation of the change of energy spectrum, fluence and mean energy at z_{max} and R_{50} may be beneficial to understand this difference better.

In clinical fields, however, increasing the energy led to a higher contribution of the scattered component to the absorbed dose not only at water surface but also at z_{max} and R_{50}. An explanation for that might be the change in the field size, because decreasing the applicator diameter resulted to a significant increase of their energy fluence. This was demonstrated in figs. 4.7 and 4.8 in subsection 4.4.1. Moreover, the electron fluence and mean energy of scattered component increased with decreasing the field size and also with increasing the electron energy. That is previously discussed in subsections 5.4.2 and 5.4.3. The influence of these factors could cause a dramatic rise in the relative contribution of scattered dose to the total depth dose.

Comparing the results with the data published for conventional linacs showed large discrepancies. Ding and Rogers reported the contribution of the direct electrons on the total dose at z_0 and z_{max} for some medical accelerators such as Varian Clinac 2100C and Therac 20

[19]. They resulted that for 9 MeV beam at z_0, 60 and 70% of contribution is due to direct electrons for Clinac and Therac, respectively. Furthermore, the corresponding values at z_{max} were 75 and 96%. These relative contributions of direct electrons are significantly larger than the corresponding values of the NOVAC7 electron beams reported here. This is mainly because the conventional linacs apply different types of collimation system and have a different radiation head geometry. As demonstrated previously, the NOVAC7 beams contain much larger component of scattered electrons compared to conventional medical linacs.

Moreover, data published by Björk et al. showed that the photon contamination dose for Philips/Elekta SL25 at z_{max} is about 1% [24]. This is remarkably higher than the values resulted from the NOVAC7 (up to 0.06%). Therefore, it is important to note that the photon contamination in the NOVAC7 beams is significantly lower than that of conventional linacs.

This investigation demonstrated significant results through which a deeper comprehension related to important dosimetric parameters was achieved. The increase of output factor with decreasing the applicator diameter could be fully understood. The deviation between $s_{w,air}$ values obtained using Monte Carlo simulation and those determined by TRS-398 protocol could be extensively demonstrated and discussed. Moreover, the difference between dosimetric characteristics of the NOVAC7 and conventional linacs were successfully presented, especially with respect to scattered electrons and photon contamination.

6. Conclusion

6.1. Ion recombination correction factor

The main rationale of the present investigation was to determine the ion recombination correction factor (k_s). This issue is important for clinical dosimetry corresponding to the IOERT application. This study was specifically carried out for the Advanced Markus chamber in medium dose-per-pulse levels, which has never been investigated in detail previously. It should be noted that, in determining the k_s value using Boag's expressions, there are several parameters that play a remarkable role, e.g. the calculation of the free electron fraction, the chamber's electrode separation, the applied voltage, the type of ionization chamber, and the dose-per-pulse value considered. The results of this study are as follows:

1. All three Boag's modified expressions ($(k_s)_{th}^{B'}$, $(k_s)_{th}^{B''}$ and $(k_s)_{th}^{B'''}$) are suitable to determine the k_s factor. Due to the dose-per-pulse range investigated in this study (4 - 42 mGy/pulse), the average deviation of k_s values resulting from them lay within the measurement uncertainty (an overall uncertainty of 3% should be considered for $(k_s)_{th}^{'}/(k_s)_{w}^{ref}$ values).

2. The ion recombination correction factor assessed from the TRS-398 protocol ($(k_s)_{th}^{TVA}$) also showed reliable results up to a dose-per-pulse value of 35 mGy/pulse. It is recommended not to use this protocol for k_s determination above this value of dose-per-pulse.

3. The difference between k_s values resulted from the four evaluation models ($(k_s)_{th}^{B'}$, $(k_s)_{th}^{B''}$, $(k_s)_{th}^{B'''}$ and $(k_s)_{th}^{TVA}$) tends to reduce as the chamber's operating voltage increases. This result is consistent with theory.

4. The result for k_s using the Jaffé plot is promising and should be examined in further details.

5. On the basis of the results achieved in this study, ion recombination correction factor should be considered in low as well as high dose-per-pulse beams otherwise, an underestimation

up to 3% can occur in patient dose delivery during the IOERT clinical application.

6.2. Monte Carlo simulation and commissioning of the NOVAC7

The Monte Carlo method is a powerful tool to study the effects of different initial electron beam characteristics in general and in particular of an intraoperative electron linac. This investigation has been performed on a dedicated IOERT mobile linac with nominal electron energies of 3, 5, 7 and 9 MeV. The virtual model was accomplished using the EGSnrc Monte Carlo system. BEAMnrc and DOSXYZnrc user codes were employed to simulate the linac head and calculate the relative dose distribution in water phantom. The results were verified by two independent procedures which both provided remarkable conclusions. A very good agreement was obtained between calculated and measured dose distributions. It was necessary to assume a spectral distribution in the initial electron beam in order to obtain an acceptable conformity (better than ± 2%) with the experimental data.

Because of the large electron scatter in the IOERT applicators both energy and angular distributions of the beams were considerably different from those from conventional electron beam linacs. The proper consistency (within ± 2%) between calculated and measured beams showed that the values adapted in order to obtain the initial electron beams are realistic. It is therefore of greater importance in Monte Carlo simulations to use the correct geometrical description of the treatment head. The procedure was found to be effective and could lead to the development of a tool to assist medical physicist during the NOVAC7 commissioning where the amount of dosimetric measurements is time-consuming.

The phase-space files obtained in this work contains the full description of the beam at the phantom surface. Thus, they can be used for determination of the characteristics of any clinical beam produced by the NOVAC7. They can also be beneficial in calculating required parameters for accurate absorbed dose measurements such as perturbation factors, detector response, stopping power ratios, etc. In addition, as previously indicated (see section 1.2), using this model in a treatment planning system to generate an accurate Monte Carlo based calculation unit can be reliable alternative to radiochromic films, which are currently used for delivered dose estimation.

6.3. Stopping power ratios and output factors

The OFs were calculated and compared with measured data obtained by means of an ionization chamber in water. Furthermore, the $s_{w,air}$ values were calculated and compared with the data determined from TRS-398 dosimetry protocol. An accurate clinical dosimetry of the IOERT beams requires investigating such dosimetric characteristics, which generally can be studied only by Monte Carlo methods. The results of these simulations for the investigated beams are verified by a close compatibality achieved between calculated and measured values of output factors mostly within ±2%. This assures that an accurate Monte Carlo model of the NOVAC7 electron beams has been conducted. A supplementary verification of the results was carried out in which, they were compared with the data currently available in literature.

For absorbed dose determination under non-reference condition, beam's physical parameters (as stopping power ratios and output factors) are needed to be investigated carefully. These parameters are influenced by different energy and angular distributions deriving from various collimator systems. This clarifies why $s_{w,air}$ differed from the corresponding values resulted from dosimetry protocols. The deviation between the $s_{w,air}$ values calculated in this work and those determined using TRS-398 changes with the measurement depth in water. These differences are up to 1.5% at larger depths, where absorbed dose measurements are not performed regularly. Moreover, the discrepancy is within 0.3% at the phantom surface and less than 1% at z_{ref} .

In spite of the noticeable degradation of the electron energy at phantom surface caused by the long PMMA cylindrical IOERT applicators, such differences may not be remarkable. However, they are essential for clinical absolute dosimetry.

6.4. Scatter and contamination analysis

In summary, an investigation regarding characteristics of electrons produced by the NOVAC7 has been performed. This was presented to be essential to comprehend the results relating to important dosimetric parameters such as stopping power ratios and output factors. The difference between the NOVAC7 and other clinical linacs regarding the scattered electrons and photon contamination was successfully analysed.

On the one hand, it was demonstrated that energy fluence distribution of electrons does not change when varying the field size. On the other hand, the scattered and direct electrons have shown significant differences at altered field sizes. It would be interesting to know how the energy

fluence distribution changes at larger depth in water. That could be helpful to understand the depth dose distribution and off-axis profiles of the scattered electrons at depth of z_{max} and R_{50}.

It was also demonstrated that the fluence and mean energy of different electron components increase at larger energies and smaller applicators especially in the vicinity of the applicator wall. A more extensive study regarding the influence of this effect on patient skin dose may be required.

6.5. Future directions

This research has answered many questions and also provided the opportunity to investigate electron characteristics not previously carried out. However, there are several experimental and theoretical studies regarding this subject to be undertaken in future. On the one hand, further research needs to assess new models of charge density distribution introduced in section 4.1. This can be invaluable for determination of a more accurate value of the k_s factor. According to that, it would also be advantageous to examine the Jaffé plot extensively at very high dose-per-pulse values. This investigation was not undertaken in this work for the sake of a clear structure also to avoid confusion arising from using multiple methods for k_s determination.

On the other hand, Linear Matrix Inequation (LMI) solver included in MATLAB software should be investigated for its feasibility to obtain energy spectrum. This method was already investigated in our clinic with GEANT4 and delivered acceptable results. However, further studies on this procedure are still necessary to be carried out [102].

Meanwhile, the feasibility of using the Monte Carlo model described in this investigation in an IOERT treatment planning system should be studied. To author's knowledge, there is still no IOERT planning system established for the NOVAC7 dose calculation based on the Monte Carlo system. Moreover, the cylindrical applicators of the NOVAC7 are supplied with different beveled angles (0°, 22.5° and 45°). Therefore, further Monte Carlo simulations including beveled applicators are required to be performed to validate the current model.

It would be also noteworthy to study the chamber simulation using EGS++ Monte Carlo user code. Investigation on the chamber effective point of measurement and perturbation correction factor would be beneficial. Such studies are necessary for determination of absorbed dose in water working with medium to high dose-per-pulse electron beams. Last but not least, the development and availability of suitable ionization chambers for high dose-per-pulse beams for

the dedicated linac (NOVAC7) should be promoted.

Bibliography

[1] Halperin EC, Perez CA, Brady LW. Principles and Practice of Radiation Oncology. Lippincott Williams & Wilkins; 2008.

[2] Beddar A, Biggs P, Chang S, Ezzell G, Faddegon B, Hensley F, et al. Intraoperative radiation therapy using mobile electron linear accelerators: report of AAPM Radiation Therapy Committee Task Group No. 72. Medical physics. 2006;33(72):1476–1489.

[3] Rosi A, Viti V. Guidelines for quality assurance in intra-operative radiation therapy. Oncología. 2004;27(7):442–475.

[4] Ronsivalle C, Picardi L, Vignati A, Tata A, Benassi M. Accelerators development for intraoperative radiation therapy. PACS2001 Proceedings of the 2001 Particle Accelerator Conference. 2001;4:2494–2496.

[5] Burns DT, McEwen MR. Ion recombination corrections for the NACP parallel-plate chamber in a pulsed electron beam. Physics in medicine and biology. 1998;43:2033–2045.

[6] McEwen M, DeWerd L, Ibbott G, Followill D, Rogers DO, Seltzer S, et al. Addendum to the AAPM's TG-51 protocol for clinical reference dosimetry of high-energy photon beams. Medical physics. 2014;41(4):041501–20.

[7] IAEA. Absorbed dose determination in external beam radiotherapy. An international code of practice for dosimetry based on standards of absorbed dose to water TRS-398.IAEA, Vienna. 2004;(April).

[8] AAPM. Protocol for clinical reference dosimetry of high-energy photon and electron beams, TG-51. Medical physics. 1999;26(September):1847–1870.

[9] DIN. Procedures of dosimetry with probe-type detectors for photon and electron radiation Part 2: ionization chamber dosimetry of high energy photon and electron radiation, Technical Report No. DIN6800 part2, Berlin; 2008.

[10] Piermattei A, Canne SD, Azario L, Russo A, Fidanzio A, Micelit R, et al. The saturation loss for plane parallel ionization chambers at high dose per pulse values. Physics in medicine and biology. 2000;45:1869–1883.

[11] Laitano R, Guerra A, Pimpinella M, Caporali C, Petrucci A. Charge collection efficiency in ionization chambers exposed to electron beams with high dose per pulse. Physics in medicine and biology. 2006;51:6419–6436.

[12] Hochhaeuser E, Balk OA, Schneider H, Arnold W. Die Bedeutung der Lebensdauer und Absaugzeit freier Elektronen fuer die Rekombinationskorrektur in der ionometrischen Puls-dosimetrie. Physics in medicine and biology. 1994;27:431–440.

[13] Boag J, Hochhäuser E, Balk O. The effect of free-electron collection on the recombination correction to ionization measurements of pulsed radiation. Physics in medicine and biology. 1996;41:885–897.

[14] Di Martino F, Giannelli M, Traino A, Lazzeri M. Ion recombination correction for very high dose-per-pulse high-energy electron beams. Medical physics. 2005;32:2204–2210.

[15] Cella L, Liuzzi R, Salvatore M. The Italian affair: the employment of parallel-plate ionization chambers for dose measurements in high dose-per-pulse IORT electron beams. Medical physics. 2010;37:2918–2924.

[16] Ghorbanpour Besheli M, Simiantonakis I, Zink K, Budach W. Determination of the ion recombination correction factor for intraoperative electron beams. Zeitschrift für Medizinische Physik. 2015;In press.

[17] Fantini M, Santoni F, Soriani A, Creton G, Benassi M, Begnozzi L. IORT Novac7: a new linear accelerator for electron beam therapy. Frontiers of radiation therapy and oncology. 1997;31:54–59.

[18] Björk P, Knöös T, Nilsson P. Influence of initial electron beam characteristics on Monte Carlo calculated absorbed dose distributions for linear accelerator electron beams. Physics in medicine and biology. 2002;47:4019–4041.

[19] Ding GX, Rogers D. Energy spectra , angular spread and dose distributions of electron beams from various accelerators used in radiotherapy, Institue for National Measurement Standards, Canada. PIRS-0439; 1995.

[20] Kawrakow I, Rogers DWO. The EGSnrc Code System : Monte Carlo Simulation of Electron and Photon Transport. NRCC Report PIRS-701; 2003.

[21] Björk P, Knöös T, Nilsson P. Measurements of output factors with different detector types and Monte Carlo calculations of stopping-power ratios for degraded electron beams. Physics in medicine and biology. 2004;49:4493–4506.

[22] Pimpinella M, Mihailescu D, Guerra A, Laitano R. Dosimetric characteristics of electron beams produced by a mobile accelerator for IORT. Physics in medicine and biology. 2007;52:6197–6214.

[23] Mihailescu D. Monte Carlo calculation of depth-dose distribution, dose components and output factors for degraded electron beams produced by an IORT accelerator. In: Analele Stiintifice Ale Universitatii; 2006. p. 97–102.

[24] Björk P, Nilsson P, Knöös T. Dosimetry characteristics of degraded electron beams investigated by Monte Carlo calculations in a setup for intraoperative radiation therapy. Physics in medicine and biology. 2002;47:239–256.

[25] Ma CM, Rogers DWO. BEAMDP Users Manual. NRCC Report PIRS-0509(c)revA. 2009;.

[26] Rogers DWO, Walters B, Kawrakow I. BEAMnrc Users Manual. NRCC Report PIRS-0509; 2009.

[27] Walters B, Kawrakow I, Rogers DWO. DOSXYZnrc Users Manual. NRCC Report PIRS-794revB; 2011.

[28] Comas C, Prio A. Irradiation roentgen preventive intraabdominale, apres intervention chirurgicale dans un cas de cancer de luterus. In: Congres International dElectrologie. Imprenta Francesca Badia. Barcelona; 1906. p. 5–14.

[29] Beck C. On external Roentgen treatment of internal structures (eventration treatment). New York Medical Journal. 1909;89:621–622.

[30] Gunderson LL, Willett CG, Calvo FA, Harrison LB. Intraoperative Irradiation. 2nd ed. Springer Science+Business Media; 2011.

[31] Abe M, Takahashi M. Intraoperative Radiotherapy: The Japenese Experience. Int J Radiation Oncology Biol Phys. 1981;7:863–868.

[32] Abe M . Intraoperative Radiotherapy-past, Present and Future. Int J Radiation Oncology Biol Phys. 1984;10:1987–1990.

[33] Gerbi B, Antolak J, Deibel F, Followill D, Herman M, Higgins P, et al. Recommendations for clinical electron beam dosimetry: supplement to the recommendations of Task Group 25. Medical physics. 2009;36(July):3239–3279.

[34] Attix F. Introduction to Radiological Physics and Radiation Dosimetry. New York: John Wiley & Sons; 1986.

[35] Podgorsak E. Radiation Physics for medical physicists. 2nd ed. Springer; 2010.

[36] Bethe J, Ashkin H. Experimental Nuclear Physics. Seger E, editor. New York: John Wiley & Sons; 1953.

[37] Evans RD . The Atomic Nucleus. Florida: Robert Krieger Co.; 1982.

[38] Griffiths D. Introduction to elementary particles. 2nd ed. WILEY-VCH Verlag GmbH & Co. KGaA; 2004.

[39] Podgorsak EB. Radiation Oncology Physics: A Handbook for Teachers and Students. Austria: IAEA; 2005.

[40] Seco J, Verhaegen F. Monte Carlo Techniques in Radiation Therapy. Florida: Taylor &Francis Group; 2013.

[41] Compte de Buffon G. Essai darithmetique morale. Supplement a la Naturelle; 1777.

[42] Metropolis N. The begining of the Monte Carlo method. Los Alamos Science (Special Issue). 1987;p. 125–130.

[43] Echhart R, Ulam S, Von Neumann J. The Monte Carlo method. Los Alamos Science (Special Issue). 1987;p. 131–141.

[44] Metropolis N, Ulam S. The Monte Carlo method. Amer Stat Assoc. 1949;44:335–341.

[45] Kalos M, Witlock P. Monte Carlo Methods. Weinheim: WILEY-VCH Verlag GmbH & Co. KGaA; 2004.

[46] Rogers DWO. Fifty years of Monte Carlo simulations for medical physics. Physics in medicine and biology. 2006;51(13):R287–R301.

[47] Berger M. Monte Carlo calculation of the penetration and diffusion of fast charged particles. Methods in Computational Physics. 1963;1:135–215.

[48] Berger M, Seltzer S. ETRAN Monte Carlo code system for electron and photon transport through extended media. Radiation Schielding Information Center, Cpmputer Code Collection, CCC-107; 1968.

[49] Briesmeister J . MCNP - A general purpose Monte Carlo code for neutron and photon transport, Version 3A.; 1986.

[50] Nelson R, Hirayama H, Rogers DWO. The EGS4 Code System; 1985.

[51] Bielajew A, Hirayama H, Nelson W, Rogers DWO . History, overview and recent improvements of EGS4. Ottawa, Canada: National Research Council of Canada: History, overview and recent improvements of EGS4 Technical Report PIRS-0436; 1994.

[52] Ford R, Nelson W. The EGS code system, version 3. Stanford, CA: Stanford Linear Accelerator Center; 1978.

[53] Bielajew A, Rogers D. PRESTA: The parameter reduced electron-step transport algorithm for electron Monte Carlo transport. Nucl Instrum Methods. 1987;B18:165–181.

[54] Kawrakow I . Accurate condensed history Monte Carlo simulation of electron transport: I. EGSnrc, the new EGS4 version. Medical Physics. 2000;27:485–98.

[55] Hirayama H, Namito Y, Bielajew A, Wilderman S, Nelson W. The EGS5 code system. SLAC-R-730, KEK-2005-8, KEK-REPORT-2005-8; 2005.

[56] Agostinelli S, Allison J, Amako K, Apostolakis J, Araujo H, Arce P, et al. GEANT4, a simulation toolkit. Nucl Instrum Methods A. 2003;A506:250–303.

[57] Baro J, Sempau J, Fernandez-Varea J, Salvat F. PENELOPE: An algorithm for Monte Carlo simulation of the penetration and energy loss of electrons and positrons in matter. Nucl Instrum Methods. 1995;B100:31–46.

[58] ICRU. Specification of high activity gamma-ray sources, ICRU Report 18, ICRU, Washington, DC; 1971.

[59] Petti P, Goodman MS, Gabriel T, Mohan R. Investigation of buildup dose from electron contamination of clinical photon beams. Medical physics. 1983;10(18).

[60] Teng S, Anderson D, Lindstorm D. Monte Carlo electron-transport calculations for clinical beams using energy grouping. Appl Radiant Isotopes. 1986;p. 1189–1194.

[61] Mackie T. Applications of the Monte Carlo method in Radiotherapy. In Dosimetry of Ionizing Radiation. eds Kase K, Bjärngard B, Attix F, editors. Academic Press, New York; 1990.

[62] Spezi E, Lewis G. An overview of Monte Carlo treatment planning for radiotherapy. Radiat Prot Dosimetry. 2008;131(1):123–129.

[63] Reynaert N, van der Marck S, Schaart D, van der Zee W, Tomsej M, van Vliet-Vroegindeweij C, et al. Monte Carlo treatment planning: An Introduction; 2006.

[64] James F. Monte Carlo theory and practice. Reports on Progress in Physics. 1980;43(9):1145–1189.

[65] de Vries R. An EGSnrc Monte Carlo Investigation of Backscattered Electrons from Internal Shielding in Clinical Electron Beams. Ph.D. Thesis. Canterbury; 2014.

[66] Verhaegen F, Seuntjens J. Monte Carlo modelling of external radiotherapy photon beams. Physics in medicine and biology. 2003;48:107–64.

[67] Moreno M. Monte Carlo simulations for dosimetric verification in photon and electron beam radiotherapy. Ph.D. Thesis. Nova De Lisboa; 2012.

[68] Krieger H. Radiation Measurement and Dosimetry. Wiesbaden: Springer Fachmedien; 2013.

[69] Spencer L V and Attix F H . A theory of cavity ionization. Radiat Res. 1955;3:239–358.

[70] Nahum A. Water/air stopping-power ratios for megavoltage photon and electron beams. Physics in medicine and biology. 1978;23:24–38.

[71] IAEA. The use of plane parallel ionization chambers in high energy electron and photon beams: An international code of practice for dosimetry TRS-381, IAEA, Vienna; 1997.

[72] Khan FM. The Physics of Radiation Therapy. 3rd ed. Lippincott Williams & Wilkins; 2003.

[73] Zink K, Wulff J. Beam quality corrections for parallel-plate ion chambers in electron reference dosimetry. Physics in Medicine and Biology. 2012;57(7):1831–1854.

[74] Zink K, Wulff J. On the wall perturbation correction for a parallel-plate NACP-02 chamber in clinical electron beams. Medical physics. 2011;38(2):1045–1054.

[75] Zink K, Wulff J. Monte Carlo calculations of beam quality correction factors kQ for electron dosimetry with a parallel-plate Roos chamber. Physics in medicine and biology. 2008;53(6):1595–1607.

[76] Czarnecki D, Zink K. Monte Carlo calculated correction factors for diodes and ion chambers in small photon fields. Physics in medicine and biology. 2013;58(8):2431–44.

[77] Wulff J, Heverhagen J, Zink K. Monte-Carlo-based perturbation and beam quality correction factors for thimble ionization chambers in high-energy photon beams. Physics in medicine and biology. 2008;53(11):2823–2836.

[78] Wulff J, Heverhagen J, Karle H, Zink K. Investigation of correction factors for non-reference conditions in ion chamber photon dosimetry with Monte-Carlo simulations. Zeitschrift fur Medizinische Physik. 2010;20(1):25–33.

[79] Boag JW. Ionization Measurements at Very High Intensities–Part I: Pulsed Radiation Beams. British Journal of Radiology. 1950;23(October):601–611.

[80] SIT. NOVAC7 Operation Manual. Italy; 2007.

[81] Ottosson R. Monte Carlo Treatment Planning for Advanced Radiotherapy, Commissioning, workflow and applications for IMRT and VMAT. Ph.D. Thesis. DTU Nutech; 2012.

[82] Muir B. Measurements and Monte Carlo simulations for reference dosimetry of external radiation therapy beams. Ph.D. Thesis. Carleton; 2013.

[83] PTW-Freiburg. Gebrauchsanweisung PinPoint 3D-Kammer; 2008.

[84] PTW-Freiburg. Gebrauchsanweisung Advanced Markus-Kammer Ionisationskammer Typ 34045; 2013.

[85] Ashland. Gafchromic EBT2, Scan Handling Guide. Covington, USA; 2009. February.

[86] Ferreira B, Lopes M, Capela M. Evaluation of an Epson flatbed scanner to read Gafchromic EBT films for radiation dosimetry. Physics in Medicine and Biology. 2009;54(4):1073–1085.

[87] Aland T, Kairn T, Kenny J. Evaluation of a Gafchromic EBT2 film dosimetry system for radiotherapy quality assurance. Australasian Physical and Engineering Sciences in Medicine. 2011;34(2):251–260.

[88] Butson M, Cheung T, PKN Y, Alnawaf H. Dose and aborption spectra response of EBT2 Gafchromic film to high energy x-rays. Aust Phys Eng Sci Med. 2009;32(4):196–202.

[89] Arjomandy B, Tailor R, Anand A, Sahoo N, Gillin M, K P, et al. Energy dependence and dose response of Gafchromic EBT2 film over a wide range of photon, electron, and proton beam energies. Medical physics. 2010;37(5):1942–1947.

[90] Devic S, Seuntjens J, Sham E, Podgorsak E. Precise radiochromic film dosimetry using a flat-bed document scanner. Medical Physics. 2005;32(7):2245–2253.

[91] Martisíková M, Ackermann B, Jäkel O. Analysis of uncertainties in Gafchromic EBT film dosimetry of photon beams. Physics in medicine and biology. 2008;53:7013–7027.

[92] IBA-Dosimetry. OmniPro-I'mRT User's Guide. Schwarzenbruck, Germany; 2013.

[93] Karsch L, Beyreuther E, Burris-Mog T, Kraft S, Richter C, Zeil K, et al. Dose rate dependence for different dosimeters and detectors: TLD, OSL, EBT films, and diamond detectors. Medical Physics. 2012;39(5):2447.

[94] Blad B, Nilsson P, Knöös T. The influence of air humidity on an unsealed ionization chamber in a linear accelerator. Physics in medicine and biology. 1996;41:2541–2548.

[95] Weinhous MS, Meli JA. Determining Pion, the correction factor for recombination losses in an ionization chamber. Medical physics. 1984;11:846–849.

[96] Hochhauser E, Balk OA. The influence of unattached electrons on the collection efficiency of ionisation chambers for the measurement of radiation pulses of high dose rate. Physics in Medicine and Biology. 1986;31:223–233.

[97] Rogers DWO, Kawrakow I, Seuntjens J, Walters B. NRC User Codes for EGSnrc. NRCC Report PIRS-702revB; 2010.

[98] Burns D, Ding G, Rogers D. R50 as a beam quality specifier for selecting stopping-power ratios and reference depths for electron dosimetry. Medical physics. 1996;23(3):383–388.

[99] Kosunen A, Rogers D. Beam Quality Specification for Photon Beam Dosimetry. Medical Physics. 1993;20:1181–1188.

[100] Bruggmoser G, Saum R, Schmachtenberg A, Schmid F, Schüle E. Determination of the recombination correction factor ks for some specific plane-parallel and cylindrical ionization chambers in pulsed photon and electron beams. Physics in medicine and biology. 2007;52:N35–N50.

[101] Eroglu Z. Untersuchungen des Sättigungseffektes gasgefüllter Ionisationskammern an verschiedenen medizinischen Linearbeschleunigern. Master Thesis. Dusseldorf; 2013.

[102] Martini P. Monte-Carlo Simulation und Vergleich mit der Basisdosimetrie von Elektronenstrahleigenschaften eines mobilen intraoperativen Bestrahlungssystems. Bachelor Thesis. Dusseldorf; 2011.

A. Free electron parameters

A.1. Drift velocity

The electron drift velocity, ω, in air was calculated for Advanced Markus chamber with an electrode spacing of 1 mm based on the formula suggested by Laitano et al. This equation is obtained on the basis of experimental data previously published, as described in the literature [11]. In this regard, the ω value is obtained by

$$\omega = a + b[(1 - e^{-cE}) - d/n(1 + ce^{-nE} - ne^{-cE}/n - c)], \tag{A.1}$$

where E is the electric field strenght (Vcm^{-1}) and other constants are listed in table A.1:

Table A.1.: The values of constants in equation A.1

n	$d + e(cmV^{-1})$
a	$5.835353 \times 10^{4} cms^{-1}$
b	$2.4181 \times 10^{7} cms^{-1}$
c	$1.568094 \times 10^{-4} cmV^{-1}$
d	$3.863959 \times 10^{-3} cmV^{-1}$
e	$1.030391 \times 10^{-3} cmV^{-1}$

A.2. Life time

The equation for τ, the electron lifetime (mean time until attachment) in the air cavity of the Advanced Markus ionization chamber were taken from the experimental results by Laitano et al. and is given as

$$\tau = f(1 - e^{-gE}) + h(1 - e^{-iE}), \tag{A.2}$$

where E is the same as above and the constants are listed in table A.2:

Table A.2.: The values of constants in equation A.2

E	$V/d(Vcm^{-1})$
f	$6.269504 \times 10^{-8}s$
g	$1.826788 \times 10^{-4}s$
h	$6.444005 \times 10^{-8}s$
i	$1.811122 \times 10^{-4}s$

B. TVA method

B.1. TVA based on Boag's modified expressions

The TVA to be solved for each recombination model described in this study (eqs. 3.11, 3.12 and 3.13) to determine u_1 are shown below. The equations B.1, B.2 and B.3 are obtained by Latiano et al. [11] based on the Boag et al. [13] recombination models. Once the pair of charge values Q_1, Q_2 corresponding to the pair of chamber voltages V_1, V_2 was measured, each of these equations are able to be solved to obtain u_1.

TVA method for the first recombination model, eq. 3.11:

$$Q_1/Q_2 = V_1/V_2 \left(\frac{ln\left[1 + \dfrac{e^{p_1 u_1} - 1}{p_1}\right]}{ln\left[1 + \dfrac{e^{V_1 V_2^{-1} p_2 u_1} - 1}{p_2}\right]} \right) \tag{B.1}$$

TVA method for the second recombination model, eq. 3.12:

$$Q_1/Q_2 = \frac{p_1 u_1 + ln\left[1 + (1 - p_1)\, u_1\right]}{p_2 u_1 + \frac{V_1}{V_2} ln\left[1 + \frac{V_1}{V_2}(1 - p_2)\, u_1\right]} \tag{B.2}$$

TVA method for the third recombination model, eq. 3.13:

$$Q_1/Q_2 = \frac{\lambda_1 u_1 + ln\left[1 + \frac{1}{\lambda_1}\left(e^{\lambda_1(1-\lambda_1)u_1} - 1\right)\right]}{\lambda_2 u_2 + \frac{V_2}{V_1} ln\left[1 + \frac{1}{\lambda_2}\left(e^{\lambda_2(1-\lambda_2)\left(\frac{V_1}{V_2}\right)u_1} - 1\right)\right]} \tag{B.3}$$

The values for u_1 thus obtained by Newton's iterative method (described below) are substi-

tuted in the equation of $(k_s)_{th}^{B'}$, $(k_s)_{th}^{B''}$ or $(k_s)_{th}^{B'''}$ (according to the specific recombination model) in order to obtain the ion recombination correction factor at the chosen chamber voltage, V_1.

B.2. Newton's iterative method

Newton's method, is a root-finding algorithm that uses the first few terms of the Taylor series of a function in the vicinity of a suspected root. Let x_0 be a good estimate for x and let $x = x_0 + \epsilon$. Since the true root is x, and $\varepsilon = x - x_0$, the number ϵ measures how far the estimate x_0 is from the truth. Since ϵ is 'small', we can use the linear (tangent line) approximation to conclude that

$$0 = f(x) = f(x_0 + \epsilon) \approx f(x_0) + \epsilon f^{'}(x_0), \tag{B.4}$$

and therefore, unless $f^{'}(x_0)$ is close to zero,

$$\epsilon = -\frac{f(x_0)}{f^{'}(x_0)}. \tag{B.5}$$

It follows that

$$x = x_0 + \epsilon \approx x_0 - \frac{f(x_0)}{f^{'}(x_0)}. \tag{B.6}$$

Our new improved estimate x_1 of x is therefore given by

$$x_1 = x_0 - \frac{f(x_0)}{f^{'}(x_0)}. \tag{B.7}$$

The next estimate x_2 is obtained from x_1 in exactly the same way as x_1 was obtained from x_0:

$$x_2 = x_1 - \frac{f(x_0)}{f^{'}(x_0)} \tag{B.8}$$

Continue in this way, if x_n is the current estimate, then the next estimate x_{n+1} can be obtained iteratively by

$$x_{n+1} = x_n - \frac{f(x_0)}{f'(x_0)}. \tag{B.9}$$

The Newton iteration is then given by equation B.9 , start with an initial guess of the root x_0, then find the limit of the iteration [13].

C. Acknowledgements

I would like to express my deep gratitude to my supervisor Dr. Ioannis Simiantonakis for his unconditional support throughout the course of my Ph.D. His academic supervision and personal assistance were invaluable to conclude this work. I thank him for the time he spent on the revision of the manuscript and useful discussions. He was always there to provide help with my presentations, abstracts, and papers.

I thank my scientific father and clinic director, Prof. Wilfried Budach for his unwavering, permanent support and advice during last six years. I am also very grateful to Burkhardt Bannach, chief physicist. Without his positive attitude towards my project, it would never have been finished. My appreciation goes to my mentor Prof. Thomas Heinzel for his guidance throughout the research and his support whenever it was needed. I would like to thank Prof. Edwin Bölke for organizing administrative issues concluded to start my Ph.D course in Dusseldorf. I would also wish to thank the assistance of my colleagues in the Dep. of Radiotherapy at University Hospital of Dusseldorf. The success of this project is largely due to their support and patience. They created a positive working environment.

I would like to thank Prof. Klemens Zink and Philip von Voigts-Rhetz from IMPS for providing the EGSnrc Monte Carlo system. I acknowledge the great assistance of Elham Ehsandar, who read the manuscript and gave me detailed comments. I thank Oliver Fielitz for all the help he provided me answering tricky LaTeX questions. I would like to thank my best friends Patrick Kleinmann, Maik Gellrich and Daniel Mengai for the wonderful time I spent with them, for giving encouragement and enthusiasm during past few years.

Finally, I thank the support of my family and friends, especially my brother Reza whose financial support made travelling to Germany in 2010 possible.

D. Statement of originality

I, Majid Ghorbanpour Besheli, declare that the work presented in this thesis with the title "Monte Carlo Simulation, Analytical Investigation and Dosimetric Verification of Intraoperative Electron Beams" is my independent endeavor. Where information and graphics have been derived from other sources, I confirm that this has been indicated in the thesis.

Dusseldorf, 25.01.2016 Majid Ghorbanpour Besheli

Determination of the ion recombination correction factor for intraoperative electron beams

Majid Ghorbanpour Besheli[a,b,*], **Ioannis Simiantonakis**[a,b], **Klemens Zink**[c], **Wilfried Budach**[a]

[a] Department of Radiotherapy and Radiation Oncology, University Hospital of Duesseldorf, Germany
[b] Faculty of Physics/Medical Physics, Heinrich-Heine University of Duesseldorf, Germany
[c] Institute of Medical Physics and Radiation Protection (IMPS), University of Applied Science (THM) Gießen, Germany

Received 11 January 2015; accepted 15 June 2015

Abstract

The ion recombination correction factor (k_s) is determined for the Advanced Markus chamber exposed to electron beams produced by a dedicated intraoperative radiation therapy (IORT) accelerator at medium dose-per-pulse values. The authors evaluate five different methods. Three of them are known as Boag's modified expressions, which are based on the two-voltage-analysis method and include the free-electron component. In the fourth method the IAEA TRS-398 protocol is applied, which uses the same two-voltage-analysis method but ignores the free-electron component, and finally the fifth approach is known as the Jaffé plot. k_s values were obtained in the range of 4 mGy/pulse to 42 mGy/pulse and were compared with k_s values determined by means of radiochromic films, which are independent of the dose rate. It was found that k_s values that resulted from the three Boag's modified expressions and the TRS-398 protocol deviated by on average 1.5% and 1.4%, respectively, from the reference k_s values based on film dosimetry. These results are within the estimated relative uncertainty of ±3%. On the other hand, the absolute deviation of each method depends on the dose-per-pulse value at which the method is investigated. In conclusion, in the medium dose-per-pulse range all Boag's modified expressions could be used for k_s determination. Above a dose-per-pulse value of 35 mGy/pulse, the TRS-398 approach should be avoided. At 27 mGy/pulse and a

Bestimmung des Korrekturfaktors der Ionenrekombination für intraoperative Elektronenstrahlen

Zusammenfassung

Der Korrekturfaktor der Ionenrekombination (k_s) bei Bestrahlung mit Elektronen aus einem dedizierten Linearbeschleuniger für die intraoperative Strahlentherapie (IORT) bei mittleren Dosisbereichen pro Puls mittels fünf unterschiedlicher Ansätze für eine Advanced-Markus-Kammer wurde untersucht: Die ersten drei sind als modifizierte Boag-Ansätze bekannt, welche auf der Zweispannungsanalyse basieren und die Komponente der freien Elektronen einbeziehen. Die vierte Methode verwendet das IAEA TRS-398-Protokoll, welches ebenfalls die Zweispannungsanalyse anwendet, allerdings die Komponente der freien Elektronen nicht berücksichtigt, während die letzte Methode als Jaffé-Plot geläufig ist. Die k_s-Werte wurden im Bereich von 4 bis 42 mGy/Puls ermittelt und mit den Ergebnissen aus radiochromen Filmen verglichen, welche unabhängig von der Dosisleistung sind. Sie variierten je nach verwendeter Methode (modifizierte Boag-Ansätze, TRS-398 Protokoll und Jaffé-Plot) im Mittel um 1,5%, 1,4% und 0,3% relativ zu den mittels Filmdosimetrie ermittelten k_s-Werten. Diese Ergebnisse liegen einerseits innerhalb der tolerierten relativen Ungenauigkeit von ±3%,

*Corresponding author: Majid Ghorbanpour Besheli, Department of Radiotherapy and Radiation Oncology, University Hospital of Duesseldorf, Duesseldorf, Germany.
E-mail: majid.ghorbanpour@med.uni-duesseldorf.de (M. Ghorbanpour Besheli).

maximum operation voltage of 300 V the k_s value resulting from the Jaffé plot showed a 0.3% deviation from the reference value. More investigation on the Jaffé plot is necessary at higher dose-per-pulse values.

Keywords: Intraoperative radiation therapy, ion recombination correction factor, Two-Voltage-Analysis, free-electron fraction

andererseits ist die absolute Abweichung jeder Methode abhängig vom Wert der Dosis pro Puls für welchen sie jeweils untersucht wurde. Zusammenfassend ist festzuhalten, dass die Ansätze nach Boag allesamt für die k_s-Bestimmung geeignet sind. Ab etwa 35 mGy/puls sollte die Berechnung nach dem TRS-398-Protokoll vermieden werden. Für 27 mGy/Puls und die Maximalspannung der Ionisationskammer von 300 V weist der Jaffé-Plot eine Abweichung des k_s-Wertes von lediglich 0,3% gegenüber dem Referenzwert auf. Für höhere Dosis pro Puls-Werte sind weitere Untersuchungen erforderlich.

Schlüsselwörter: Intraoperative Strahlentherapie, Korrekturfaktor der Ionenrekombination, Zweispannungsanalyse, freie Elektronen-Komponente

1 Introduction

In intraoperative radiation therapy (IORT) a high single dose is applied to the tumor bed directly after resection of the malignancy. This therapy option allows achieving a selective radiation boost on the tumor volume. In some cases, it can also be used as a single-fraction/stand-alone treatment in initial cancers of small volume, or in unresectable malignancies for palliative purposes [1,2]. IORT treatments can be realized using dedicated electron linear accelerators that produce high dose-per-pulse electron beams, which in particular significantly shortens the treatment time compared to other methods [3].

Producing high dose-per-pulse beams however introduces new challenges of measuring the absorbed dose using ionization chambers. This is mainly because the effect of the ion recombination correction factor k_s will be more profound. This factor corrects the response of the ionization chamber for the ion loss due to the recombination of ions inside the chamber [4]. Based on current dosimetric protocols, the k_s factor is mostly determined by Boag's two-voltage-analysis (TVA) method or the Jaffé method [5–8].

Recent publications have shown that at high dose-per-pulse values these methods do not predict the k_s factor accurately [9,10]. Piermattei et al. have reported that these protocols are not suitable for dosimetry of high dose-per-pulse electron beams [9]. They observed that the k_s values resulting from these protocols deviate up to 20% from the values obtained by means of dose-rate-independent dosimeters. Discrepancies are caused by an effect known as free-electron fraction p, which is disregarded in the current protocols but is significant for k_s determination in high dose-per-pulse beams.

Free electrons are electrons generated by a radiation pulse that do not attach to oxygen molecules and reach the collecting electrode of the chamber [11]. Therefore, due to the collection of free electrons a reduction in recombination and an increase in chamber efficiency occur. These effects are neglected in current dosimetry protocols. Consequently the k_s factor will be overestimated. In order to solve this problem, three improved theoretical models for the charge collection process incorporating the free-electron component have been introduced by Boag et al., called Boag's modified expressions [12]. Di Martino et al. have used one of these models and proposed a method to determine the p value for Markus and PTW-Roos chambers [13]. In their method k_s values were determined using a dose-per-pulse-independent dosimeter. Another experimental approach, which used Boag's three expressions, was proposed by Laitano et al. [10]. Here k_s values were determined for different ion chambers without using any dose-per-pulse-independent dosimeter. In their method the value of p was calculated as a function of chamber characteristics and experimental conditions. These two approaches were compared by Cella et al. for the Markus chamber and the Advanced Markus chamber [14]. They concluded that, for the Markus ion chamber, the first model of Boag's modified expressions could predict the k_s value more accurately than other models for dose rates above 30 mGy/pulse.

However, although the effect of free electrons on the k_s factor was demonstrated more than ten years ago, not much attention has been paid to determine whether the standard methods (IAEA TRS-398 and Jaffé diagram) deliver acceptable results using an Advanced Markus ionization chamber. Moreover, the determination of the ion recombination correction factor for dose rates varying from 4 mGy/pulse to about 42 mGy/pulse has not been extensively examined yet.

The intention of this article is to determine this k_s factor using different approaches and compare them with a dose-per-pulse-independent dosimeter. Furthermore the results reported by Cella et al. and Laitano et al. will be evaluated especially for the Advanced Markus chamber in medium dose-per-pulse levels [10,14]. To start with we obtained the reference ion recombination correction factor ($(k_s)_w^{ref}$). This

was done by measuring absorbed dose to water with dose-per-pulse-independent Gafchromic EBT radiochromic films ($D_{w,Gaf}$) and an Advanced Markus chamber (D_w) (sec. 2.2.1). Subsequently we tested five different methods to determine k_s.

2 Materials and Methods

2.1 Novac7 IORT system

The NOVAC7 (SIT, Vicenza/Italy) is a dedicated mobile electron linear accelerator for IORT and has been used in several European IORT facilities since 1998 [15]. It has many advantages compared to other non-dedicated IORT treatment systems: high surface dose (>80%), low total bremsstrahlung photon dose (<0.3%), small in size and light weight with different electron energies (3, 5, 7 and 9 MeV) and different cylindrical applicator sizes with diameters from 30 mm to 100 mm [3]. By combining different energies and applicators, dose-per-pulse values in the 4-42 mGy/pulse range may be produced, which is much higher than the values obtained from conventional linear accelerators used in external beam therapy (∼0.1 mGy/pulse).

2.2 Measurement

An absolute dose measurement in water $D_{w,Gaf}$ was performed using dose-per-pulse-independent Gafchromic EBT2 films (Ashland, Wayne/USA) [16]. The films were calibrated using a thimble chamber type 23332 (PTW-Freiburg, Freiburg/Germany) with a sensitive volume of 0.3 cm^3. The ionization chamber was positioned centrally in a $10 \times 10\,cm^2$ square field at a depth of 5 cm in a small water phantom ($30 \times 30 \times 30\,cm^3$) type T41023 (PTW-Freiburg) at a source-to-surface distance of 95 cm. It was irradiated with 200 monitor units. The polarizing voltage was set to 400 V. The reference dose irradiation system was a clinical linear accelerator of 6 MV photon beam (Precise, Elekta AB, Stockholm/Sweden). Corrections were made for polarity, temperature and air pressure. Humidity was measured as 47% but not corrected for, because of its insignificant effect on the results [17]. For dose calibration the films were cut into $5 \times 5\,cm^2$ square sheets and were irradiated with 50, 100, 150, 200, 250, 300, 400, 500, 600, 700 and 800 monitor units. In addition, an unexposed film was used to obtain the background optical density (OD). The films were stored in a dark place at room temperature and evaluated 24 h after irradiation. The film digitalization was done using a commercial flat panel scanner (Perfection V750 PRO, Epson, Nagano/Japan). The films were positioned in the middle of the scanner area and processed with a scanning resolution of 72 dpi. The red channel was used in order to determine the net optical densities (*netOD*). The Omnipro I'MRT software (IBA Dosimetry GmbH, Schwarzenbruck/Germany) was applied to obtain the relationship of OD values versus dose. The plot of dose as a function of optical density is shown in Figure 1.

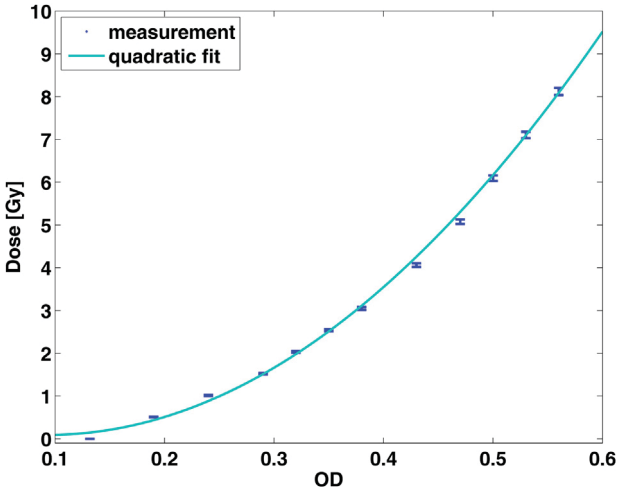

Figure 1. Gafchromic EBT2 film calibration curve in terms of optical density (OD) versus absorbed dose to water, by using a photon beam of 6 MV supplied by an ELEKTA Precise linear accelerator. The fit was obtained by using a quadratic function. The error bars show the combined uncertainty of the measured doses and ODs.

2.2.1 *The reference recombination factor,* $(k_s)_w^{ref}$

The absolute dose measurement was also carried out using an Advanced Markus chamber (PTW-Freiburg type 34045). An UNIDOS webline electrometer (PTW-Freiburg) was used for chamber read-out. The Advanced Markus ionization chamber was used to determine the recombination correction factors ($(k_s)_{th'}^{B'}(k_s)_{th}^{B''}$ and $(k_s)_{th}^{B''}$), applying the method suggested by Laitano et al. [10]. Additionally, according to the IAEA TRS-398 dosimetry protocol [5], absorbed dose to water at the reference depth z_{ref} for a reference beam of quality Q is given as:

$$D_w = M \cdot k_{elec} \cdot k_{TP} \cdot k_{pol} \cdot k_s \cdot N_{D,w,Q_0} \cdot k_{Q,Q_0}. \quad (1)$$

The parameters of Eq. (1) are defined in [5]. For abbreviation D_w may be written as:

$$D_w = D'_w \cdot k_s \quad (2)$$

with

$$D'_w = M \cdot N_{D,w,Q_0} \cdot k_{T,P} \cdot k_{pol} \cdot k_{elec} \cdot k_{Q,Q_0}. \quad (3)$$

Here D'_w is the absorbed dose in water not corrected for ion recombination.

On the other hand it is supposed that

$$D_w = D_{w,Gaf}. \quad (4)$$

$D_{w,Gaf}$ is the absorbed dose measured by a Gafchromic EBT2 film. Following Equations (2), (3) and (4) the reference value for the recombination correction factor ($(k_s)_w^{ref}$) is:

$$(k_s)_w^{ref} = \frac{D_{w,Gaf}}{D'_w} = \frac{D_{w,Gaf}}{M \cdot N_{D,w,Q_0} \cdot k_{TP} \cdot k_{pol} \cdot k_{elec} \cdot k_{Q,q_0}}. \quad (5)$$

2.2.2 Jaffé diagram, $(k_s)_{exp}^{jaff}$

The Jaffé diagram refers to a reciprocal plot of the chamber's reading ($1/M$) against the reciprocal of the polarizing voltage ($1/V$) [18].

In IAEA TRS-398, k_s is given by the following equation [5].

$$k_s = M_s/M, \quad (6)$$

where M_s is the dosimeter reading corresponding to the ideal situation of complete charge collection, and M is the actual reading. The dosimeter readings M were corrected for the polarity effect, temperature and pressure. On theoretical basis the plot of 1/M versus 1/V should be approximately linear, thus k_s can be obtained by linear extrapolation to an infinite chamber voltage ($1/V = 0$) [4]. In the case of pulsed beams, as recommended in the TRS-398 protocol, the range of linearity of a chamber must be established over a range of polarizing voltage up to the manufacturer's recommended maximum. According to the TG-51 dosimetry protocol, using voltages above normal operating voltages simply to reduce k_s should be avoided [6]. The applied voltages were 50 V, 100 V, 160 V, 200 V, 240 V, and 300 V. We paused 10 min between each measurement to allow the conditions in the chamber to stabilize. Each measurement was repeated three times with negative and positive polarity.

2.3 Laitano's approach

To calculate the recombination factor (k_s), we applied the formulation given by Laitano et al., where the three Boag expressions as a function of p and u were used [10,12]. These expressions are:

$$(k_s)_{th}^{B'} = \frac{u}{\ln\left(1 + \frac{e^{pu}-1}{p}\right)}, \quad (7)$$

$$(k_s)_{th}^{B''} = \frac{u}{pu + \ln[1 + (1-p)u]} \quad (8)$$

and

$$(k_s)_{th}^{B'''} = \frac{u}{\lambda u + \ln[1 + \frac{e^{\lambda(1-\lambda)u}-1}{\lambda}]}, \quad (9)$$

where $\lambda = 1 - \sqrt{(1-p)}$ and the variable u is given by

$$u = \frac{\mu d^2 r}{V}, \quad (10)$$

where d is the chamber's electrode separation, μ is a constant which depends on the filling gas, the factor r is the initial uniform charge density of positive or negative ions following a pulse of radiation, and V is the polarizing voltage.

The differences between the three models are different thicknesses of the layer free of negative charge and different negative charge density in the remainder of the cavity space. In radiation fields of low dose-per-pulse values (small values of u) the difference among the three models will be negligible and they deliver approximately similar values. For high dose-per-pulse values (larger values of u) the results of k_s obtained from different models will be different from each other [10].

This method requires the determination of the appropriate values of u. For this purpose, at different dose-per-pulse values, a set of repeated measurements of charge values Q_1 and Q_2, corresponding to the pair of chamber voltages $V_1 = +300$ V and $V_2 = +100$ V were performed. Then three equations corresponding to the expressions (7), (8), and (9) regarding the charge ratio Q_1/Q_2 according to the TVA technique were solved for the factor u by iterative methods.

This approach also requires the calculation of the free-electron fraction p as

$$p = \frac{\omega\tau}{d}\left(1 - e^{-\frac{d}{\omega\tau}}\right), \quad (11)$$

where τ (s) is the life time (mean time until attachment to the collecting electrode), ω (m/s) is the drift velocity of the free electrons in the chamber gas, and d is the chamber's electrode separation [10]. The quantity p depends on the chamber's operational conditions through d, τ and ω. τ and ω are both dependent on the electric field strength and the type of gas of the ion chamber. The coefficients τ and ω were determined as described by Laitano et al. [10]. The values of ω, τ and p, which were used in this work, are reported in Table 1.

2.4 Comparison of different methods

The Advanced Markus chamber was also utilized for the determination of the recombination correction factor according to the TRS-398 dosimetry protocol. ($(k_s)_{th}^{TVA}$).

To compare the different methods described above, the ratios $(k_s)'_{th}/(k_s)_w^{ref}$ were determined, where the $(k_s)'_{th}$

Table 1
Chamber characteristics for the Advanced Markus parallel-plate ionization chamber and estimate of free-electron fraction p, according to Eq. (11). V refers to the chamber's operating voltage.

V_1 (V)	V_2 (V)	λ_1	λ_2	p_1	p_2	$\tau_1(\times 10^{-8})$ (s)	$\tau_2(\times 10^{-8})$ (s)	$w_1(\times 10^4)$ ($m\ s^{-1}$)	$w_2(\times 10^4)$ ($m\ s^{-1}$)
300	100	0.443	0.147	0.690	0.273	5.34	2.11	2.40	1.33
400	100	0.519	0.147	0.769	0.273	6.57	2.11	2.80	1.33

factor represents the ion recombination correction factors obtained from the different methods ($(k_s)_{th}^{B'}$, $(k_s)_{th}^{B''}$, $(k_s)_{th}^{B'''}$ and $(k_s)_{th}^{TVA}$). Additionally, the average deviation between $(k_s)'_{th}$ and $(k_s)_w^{ref}$ was calculated as the mean value of the quantities $((k_s)'_{th}/(k_s)_w^{ref} - 1)$.

3 Results

3.1 Dose rate versus applicator diameter

Figure 2 shows the measured dose-rate values as a function of the applicator diameter for the four different electron energies of the Novac7 system. As can be seen, for 7 MeV and 9 MeV electrons the dose-per-pulse value measured at z_{ref} increased almost linearly (with a gradient of about 0.2 mGy/pulse mm) as the applicator diameter decreased, which is consistent with results obtained in previous studies [14,19]. However, for 3 MeV and 5 MeV electron beams the dose-per-pulse values measured at z_{ref} were almost independent of the applicator diameter (5.1 and 12 mGy/pulse for 3 MeV and 5 MeV, respectively). This is also in good agreement with results given in the literature [15].

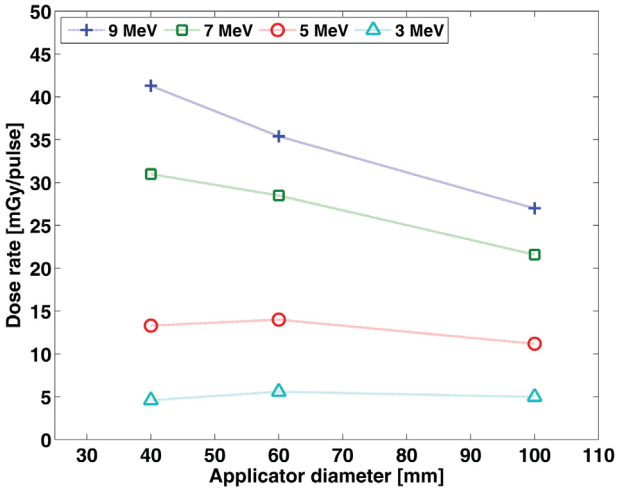

Figure 2. Dose-rate values (mGy per pulse) as a function of applicator diameter (mm) for different energies.

3.2 Comparison of ion recombination correction factors

Data obtained in previous studies [10,14] using different chambers within a specific dose-per-pulse range indicated that the acceptability of k_s values resulting from Boag's expressions and based on Laitano's approach are model-dependent. Furthermore, according to Laitano et al., k_s values resulting from the TRS-398 method deviate about 8% from reference values for the Markus chamber at 40 mGy/pulse [10]. In our study, ion recombination correction factors obtained from equations (7), (8), (9) and from the TRS-398 method were compared against the recombination correction factor determined by a reference dosimeter ($(k_s)_w^{ref}$).

Figures 3(a) - 3(d) illustrate the $(k_s)'_{th}/(k_s)_w^{ref}$ values for different dose-per-pulse values. The absolute values of k_s obtained applying the above-mentioned approaches at different dose-per-pulse values are summarized in Table 2. According to Figures 3(a)-3(d), the average deviation between k_s values calculated from different methods and the reference k_s values is within the tolerance level (3%). However, at a higher dose-rate value of about 42 mGy/pulse $(k_s)_{th}^{TVA}$ deviates from $(k_s)_w^{ref}$ by 4.2%, which is higher than our tolerance level. Although the deviation of k_s values obtained from Laitano's approach from $(k_s)_w^{ref}$ values increases with increasing dose-per-pulse values, it does not exceed the tolerance limit as shown in Table 2 and Figures 3(a)-3(d). These results indicate that the TRS-398 method is appropriate up to 35 mGy/pulse. Furthermore it could be inferred that Laitano's approach is appropriate for a k_s determination in the whole dose-per-pulse range investigated here.

3.3 k_s comparison for different chamber voltages

Table 3 shows the ratio $(k_s)'_{th}/(k_s)_w^{ref}$ obtained for different voltages (300 V and 400 V) at the lowest dose rate of 4.6 mGy/pulse and the highest dose rate of 41.3 mGy/pulse. The data denoted by $(k_s)_{th}^{TVA}/(k_s)_w^{ref}$ are relevant for the conventional two-voltage-analysis method not including the impact of free electrons. The results show that both at a low dose rate (4.6 mGy per pulse) and in a high dose rate (41.3 mGy per pulse), for a chamber with a small spacing such as the Advanced Markus chamber ($d = 1$ mm) the different expressions for k_s ($(k_s)_{th}^{TVA}$, $(k_s)_{th}^{B'}$, $(k_s)_{th}^{B''}$ and $(k_s)_{th}^{B'''}$) tended

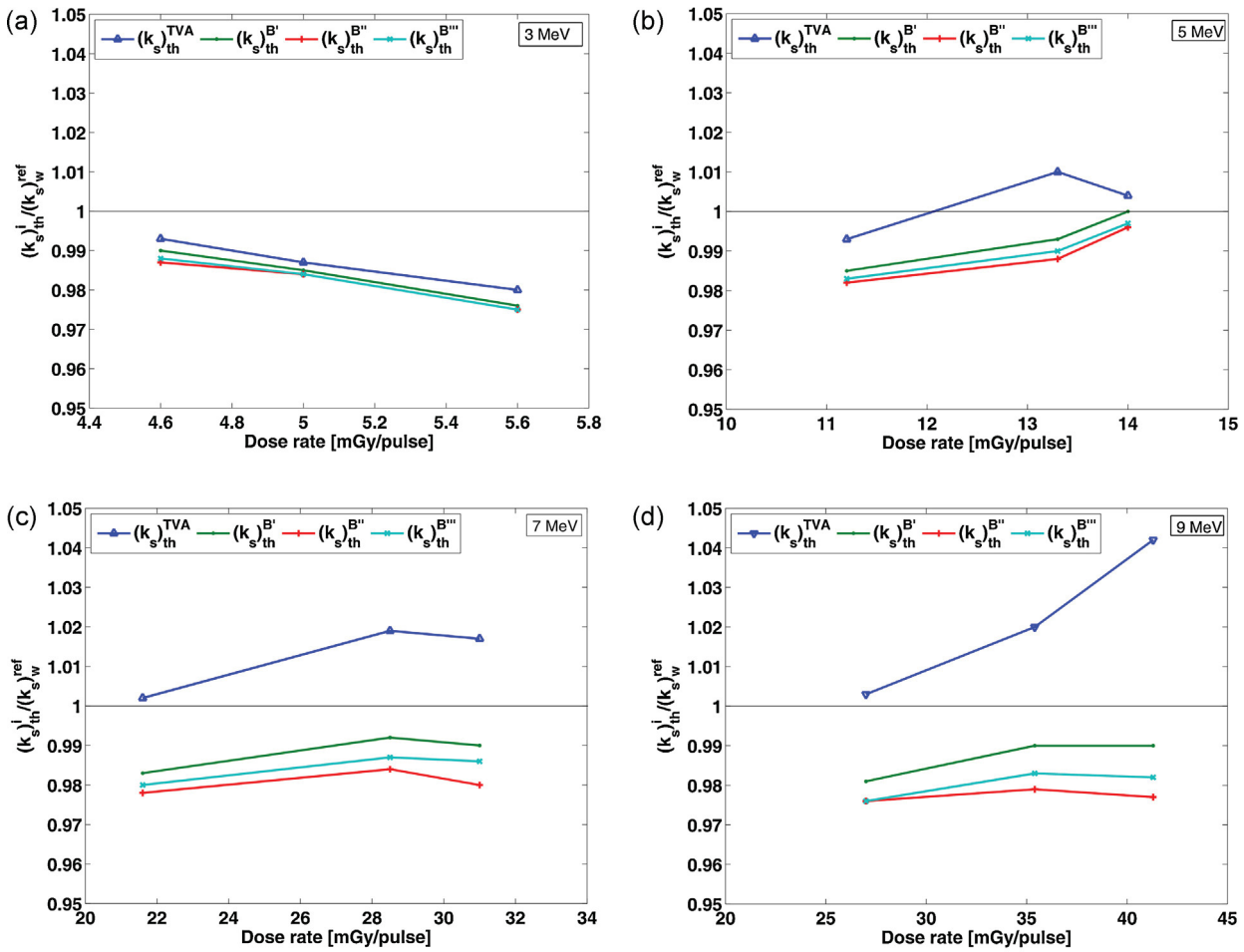

Figure 3. The $(k_s)'_{th}/(k_s)^{ref}_{w}$ ratios, (a-d), as a function of dose rate (mGy per pulse) for the Advanced Markus chamber for Top-Left (3 MeV), Top-Right (5 MeV), Down-Left (7 MeV) and Down-Right (9 MeV) electron beams, respectively. $(k_s)'_{th}$ values refer to the ion recombination correction factors related to Boag's theoretical models. The data denoted by triangles are the $(k_s)^{TVA}_{th}/(k_s)^{ref}_{w}$ ratios relevant to the conventional two-voltage-analysis method not including the impact of free electrons. The operating voltage was $V_1 = 300$ V. The uncertainty on the $(k_s)'_{th}/(k_s)^{ref}_{w}$ values is 3%.

Table 2
The values of ion recombination correction factors obtained applying different methods at different dose-per-pulse values using Gafchromic films and Advanced Markus parallel-plate ionization chamber.

Applicator (mm)	Energy (MeV)	Dose rate (mGy/pulse)	$(k_s)^{ref}_{w}$	$(k_s)^{TVA}_{th}$	$(k_s)^{B'}_{th}$	$(k_s)^{B''}_{th}$	$(k_s)^{B'''}_{th}$
40	3	4.6	1.014	1.007	1.003	1.001	1.002
100	3	5	1.017	1.004	1.002	1.001	1.001
60	3	5.6	1.027	1.007	1.002	1.001	1.001
100	5	11.2	1.020	1.013	1.005	1.002	1.003
40	5	13.3	1.015	1.025	1.008	1.003	1.005
60	5	14	1.006	1.010	1.006	1.002	1.003
100	7	21.6	1.027	1.029	1.010	1.004	1.006
100	9	27	1.032	1.035	1.012	1.007	1.007
60	7	28.5	1.021	1.040	1.013	1.005	1.008
40	7	31	1.023	1.040	1.014	1.005	1.009
60	9	35.4	1.027	1.048	1.015	1.006	1.010
40	9	41.3	1.034	1.078	1.024	1.010	1.015

Table 3
The ratios $(k_s)'_{th}/(k_s)^{ref}_w$ as a function of applied chamber voltage (300 V and 400 V) at the lowest dose rate of 4.6 mGy per pulse and the highest dose rate of 41.3 mGy per pulse, for the Advanced Markus chamber. $(k_s)'_{th}$ values refer to the ion recombination correction factor related to Boag's theoretical models ($(k_s)^{B'}_{th}$, $(k_s)^{B''}_{th}$ and $(k_s)^{B'''}_{th}$. The uncertainty on the $(k_s)'_{th}/(k_s)^{ref}_w$ values is 3%.

	4.6 mGy/pulse		41.3 mGy/pulse	
$(k_s)'_{th}/(k_s)^{ref}_w$	300V	400V	300V	400V
$(k_s)^{TVA}_{th}/(k_s)^{ref}_w$	0.993	0.994	1.042	1.024
$(k_s)^{B'}_{th}/(k_s)^{ref}_w$	0.989	0.993	0.990	1.011
$(k_s)^{B''}_{th}/(k_s)^{ref}_w$	0.987	0.991	0.980	0.988
$(k_s)^{B'''}_{th}/(k_s)^{ref}_w$	0.988	0.992	0.982	0.996

to give similar results as the chamber voltage is increased. A similar trend was reported in [10] for the Exradin A11 chamber.

3.4 Jaffé diagram

Finally, the applicability of the Jaffé diagram for k_s determination at the 27 mGy/pulse rate was investigated. This dose-per-pulse value was produced by 9 MeV electrons and a 100 mm applicator which was considered as the reference condition in our investigation. Figure 4 illustrates the relation between normalized measured values, M_0/M_v and normalized chamber's operating voltages V_0/V where M_0 is the chamber reading at the calibration voltage (V_0) and M_v is the chamber reading at the given voltage (V). The data are corrected for polarity effect (k_{pol}), temperature, and air pressure ($k_{T,P}$). As can be seen, there is an almost linear relationship in the range from 50 V up to 300 V. The resulting $(k_s)^{jaff}_{th}$ value deviates from the reference value ($(k_s)^{ref}_w$) by only 0.3%. This small deviation proves that Jaffé diagram is an appropriate method for k_s determination at reference conditions. However, future work should include a detailed analysis of this approach at higher dose-per-pulse values for the Advanced Markus chamber.

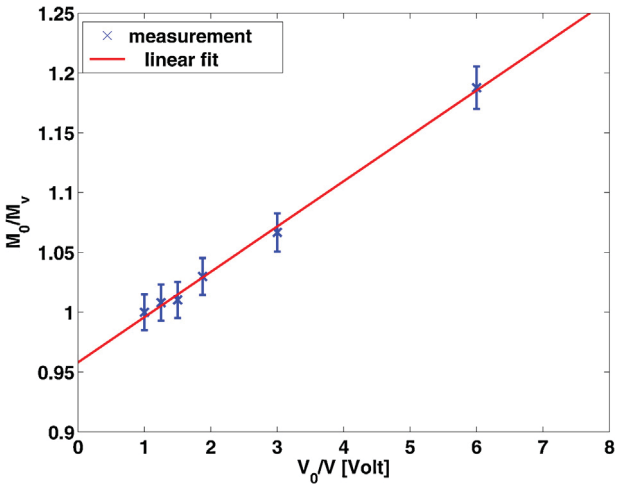

Figure 4. Jaffé plot for the Advanced Markus chamber. The normalized measured values, M_0/M_v, are plotted against the normalized chamber's operating voltages V_0/V. M_0 is the chamber reading at the calibration voltage (V_0) and M_v is the chamber reading at the given voltage (V). The data are corrected for polarity effect (k_{pol}), temperature, and air pressure ($k_{T,P}$). The solid line is a linear fit of the data. This curve is obtained for the 27 mGy/pulse produced by 9 MeV electrons and a 100 mm applicator.

4 Uncertainty analysis

According to Laitano et al. the combined uncertainty of the $(k_s)_{th}$ values at 70 mGy/pulse is 2%. Sources of uncertainty were the factors ω, τ and the chamber spacing d. As a result of the combined uncertainty of optical density (Δ=1%), polarity effect (Δ=0.6%) and calibration (Δ=1%), the uncertainty of the $D_{w,Gaf}$ values was calculated as 1.5%. The optical density (OD) uncertainty of 1.0% at 1 Gy was considered based on the analysis performed by Martisikova et al., the calibration uncertainty of 1.0% was accounted for by the determination of the beam quality correction factor based on the TRS-398 dosimetry protocol [20]. The uncertainty of D'_w was 1.5%. This is the square product of $\Delta = \pm 0.6\%$ on the calibration factor, $N_{D,w}$, based on the TRS-398 protocol, $\Delta = \pm 1.1\%$ on the beam quality correction factor, $k_{Q,Q'}$ based on the manufacturer's calibration sheet (Co-60 as the calibration quality), and Δ=0.8% for the polarity effect. Resulting from Eq. (5), the combined uncertainty for $(k_s)^{ref}_w$ was estimated as 2.1%. Combining the Δ=2.0% on $(k_s)'_{th}$ with the uncertainty of $(k_s)^{ref}_w$ led to an overall uncertainty of almost 3% for the $(k_s)'_{th}/(k_s)^{ref}_w$ ratio.

5 Discussion

During the past few years some efforts have been expended to determine the ion recombination correction factor k_s for different types of ion chambers using high dose-per-pulse electron beams of dedicated IORT accelerators. These studies have been carried out using both standard methods such as the TVA method reported in the TRS-398 protocol and the Jaffé method, or recently suggested models called Boag's modified expressions. However, not much attention has been paid to determine whether the standard methods deliver acceptable results using an Advanced Markus chamber. Furthermore, they have not focused on medium dose-per-pulse ranges. The results of the current study contain the comparison of values of ion recombination correction factors $(k_s)^{ref}_w$, $(k_s)^{B'}_{th}$, $(k_s)^{B''}_{th}$, $(k_s)^{B'''}_{th}$ $(k_s)^{jaff}_{th}$ and $(k_s)^{TVA}_{th}$ obtained by different methods reported in the literature [10,12] and performed under defined conditions.

The results shown in Figure (2) extend those of Cella et al. [14], confirming that for 9 MeV and 7 MeV electrons the dose-rate value increases almost linearly when the applicator diameter decreases. Furthermore, Monte Carlo calculations performed by Pimpinella et al. [19] at the highest NOVAC7 energies showed that with decreasing applicator diameter the contribution of scattered electrons to the calculated dose at z_{ref} increased, which consequently led to an increase of the dose-per-pulse value. This trend was not observed for 3 MeV and 5 MeV electrons. However, Fantini et al. [15] have reported analogous findings. The constancy of the dose-per-pulse value with decreasing applicator diameter may be due to the absorption of low-energy scattered electrons before they reach the z_{ref}.

Figure 3 demonstrates the deviation of different theoretical models ($(k_s)_{th}^{B'}$, $(k_s)_{th}^{B''}$, $(k_s)_{th}^{B'''}$ and $(k_s)_{th}^{TVA}$) from the reference value ($(k_s)_{w}^{ref}$). The average deviation between $(k_s)_{th}^{B'}$ and $(k_s)_{w}^{ref}$ was about -1.2% and the analogous average deviations for $(k_s)_{th}^{B''}$ and $(k_s)_{th}^{B'''}$ were slightly larger, at -1.7% and -1.6%, respectively. Considering the large uncertainty of the $(k_s)_{th}/(k_s)_{w}^{ref}$ values (3%), the results from the three Boag's expressions are all within the tolerance limit of 3%. These results are not directly comparable with the findings of previous authors because they were performed for different chambers and different dose-per-pulse ranges, but they are similar to the results published by Cella et al. [14]. Based on their study, the average deviations of $(k_s)_{th}^{B'}$, $(k_s)_{th}^{B''}$ and $(k_s)_{th}^{B'''}$ from $(k_s)_{w}^{ref}$ obtained by applying Laitano's method at dose-per-pulse values from 31 to 70 mGy/pulse for the Advanced Markus chamber were -1.1%, -1.8%, and -1.4%, respectively. The corresponding deviation of calculated k_s values from reference values using Di Martino's method was -0.9% [13]. Even when the absolute deviation of each model at each dose-per-pulse level is considered, most of them are within the tolerance level (see Table 2). This tendency was also observed in the work of Cella et al. In their study considering the large uncertainty (combined uncertainty of about 6%) at dose ranges of 31 to 70 mGy/pulse most of the calculated k_s values derived from Laitano's and Di Martino's method for the Advanced Markus and the Markus chamber are within the given uncertainty range [10,13]. Therefore within this dose-per-pulse range all three methods can be used for the calculation of the k_s factor.

All three Boag's models show an underestimation of the k_s values (see Table 2 and Figures 3(a)-3(d)). The reason for this may be the influence of the values of u (Eq. (10)) at every dose-per-pulse value. As can be seen from Eq. (10), this parameter will change at different dose-per-pulse values and is also dependent on charge-density distribution and chamber characteristics. The chamber difference or the change in the chamber's operating voltage alone cannot describe this behavior, because as shown by Laitano et al. [10], for different chamber designs, chamber electrode distance and the chamber's operating voltage the range of k_s values resulting from each model does not change dramatically and retains its tendency of overestimation or underestimation. Moreover, as reported by Cella et al. [14], under the same conditions, using the Markus chamber or the Advanced Markus chamber (average underestimation of -2.3% and -1.3%, respectively), the application of Di Martino's method or Laitano's method (average underestimation of 1.3% and 2%, respectively) does not influence this tendency directly. Future work should focus on the determination of the u value and its effect on k_s for the Advanced Markus chamber at higher dose-per-pulse values.

The results in Figures 3(a)-3(d) and Table 2 also show the absolute deviation between $(k_s)_{th}^{TVA}$ and $(k_s)_{w}^{ref}$ values. The deviation increases with increasing dose-per-pulse value and reaches a deviation of +2% at 35 mGy/pulse, which is also within the tolerance level. Increasing the dose-per-pulse rate to 42 mGy/pulse, the deviation increases up to +4.2% which is beyond the tolerance level considered in this study (3%). This high deviation at higher dose-rate values was expected because of avoiding the influence of free electron fraction for determination of $(k_s)_{th}^{TVA}$. Although there are not sufficient experimental data concerning $(k_s)_{th}^{TVA}$ in the dose-per-pulse range investigated in the current study for the Advanced Markus chamber, Laitano at al. have reported data for some other chambers (Capintec PS-033, Exradin A11, PTW Roos, NACP02, PTW Markus, and Wellhöfer PPC 05) at the 40 mGy/pulse rate [10]. They showed that $(k_s)_{th}^{TVA}$ value could deviate from the reference value by up to +8% and +11% (in their case $(k_s)_{Frick}^{ref}$ obtained by Fricke dosimeter) for the Markus and Exardin A11 chamber, respectively. The relative lower absolute deviation obtained for $(k_s)_{th}^{TVA}$ in the current study may be due to the fact that the electrode separation in the Advanced Markus chamber is half that of the Markus and Exradin A11 chambers investigated by Laitano et al. and consequently the effect of recombination in the sensitive volume of the Advanced Markus chamber is significantly reduced. As reported by Laitano et al. [10], decreasing the chamber electrode distance from 2.4 mm to 0.6 mm would lead up to an 11% improvement of the results obtained by the TVA method. Regarding the minor deviation of the $(k_s)_{th}^{TVA}$ values, the TVA method proposed by the TRS-398 protocol could be used for the determination of the ion recombination correction factor up to a dose-per-pulse value of 35 mGy/pulse.

The absolute deviation between the $(k_s)_{th}^{TVA}$ and k_s values resulting using Laitano's approach in Eqs. (7),(8) and (9) is negligible at lower dose-rate values (about 0.3%) and increases up to around 7% at a dose rate of 42 mGy/pulse (see Table 3). Although there are no data to compare our results against directly, this tendency has also been seen by Laitano et al. [10]. They observed a maximum deviation of 0.1% (between $(k_s)_{th}^{B''}$ and $(k_s)_{th}^{TVA}$) at 0.1 mGy/pulse and a maximum deviation of 30% at 70 mGy/pulse for the Exradin A11 chamber with an electrode distance of 2 mm at an operating voltage of 300 V.

Table 3 shows the deviation of different ion recombination models from the reference value for the prediction of k_s as a function of the operating voltage of the chamber. These results are consistent with those of Laitano et al. [10]. As the chamber's operating voltage increases, the difference between the values of the four recombination models ($(k_s)_{th}^{B'}$, $(k_s)_{th}^{B''}$, $(k_s)_{th}^{B'''}$ and $(k_s)_{th}^{TVA}$) decreases. This is also consistent with theory considering that this difference depends on the change of the u value when the voltage varies [10]. As expected, decreasing u in all four expressions (see (7), (8) and (9)) led to the same results. On the other hand, the quantity u is proportional to $1/V$ (see (10)). Hence, it is obvious that as the value of V increases these four expressions tend to coincide with each other.

Following the data presented in Figure (4), a +0.3% deviation from the reference value was concluded for $(k_s)_{th}^{jaff}$ at 27 mGy/pulse. A maximum deviation of 2.8% was observed between the $(k_s)_{th}^{jaff}$ and k_s values resulting from Boag's expressions, particularly between the $(k_s)_{th}^{jaff}$ and $(k_s)_{th}^{B'''}$ values. Laitano et al. obtained deviations of up to 6% between the $(k_s)_{th}^{jaff}$ and $(k_s)_{th}^{B'''}$ values at 70 mGy per pulse for the Exradin 11 chamber with a 2 mm electrode distance. Unfortunately, these values could not be compared with our results. On the other hand, different absolute values of $(k_s)_{th}^{jaff}$ could be the result of different measurement conditions, especially the electrode distance of the applied chamber and the dose-per-pulse value investigated [21]. As reported by Burns and McEwen, a difference in the parallel-plate separation of 0.16 mm causes changes in the ion recombination factor of up to 8% [4]. Furthermore, a dose-rate difference of 10 mGy/pulse results in a difference of up to 5% in the value of the ion recombination correction factor [10]. The use of the Jaffé plot has produced good results. However, further research investigating the feasibility of this method for k_s determination at higher dose-per-pulse values would be beneficial.

6 Conclusion

The main rationale of the present work was to investigate the accuracy of the ion recombination correction factor (k_s) determined using different methods currently available in the literature. Furthermore, the results reported by Cella et al. and Laitano et al. were evaluated. This study was specifically carried out for the Advanced Markus chamber in medium dose-per-pulse levels. It should be noted that, in determining the k_s value using Boag's expressions, there are several parameters that play a remarkable role, e.g. the calculation of the free electron fraction, the chamber's electrode separation, the applied voltage, the type of ionization chamber, and the dose-per-pulse value considered. The results of this study considering the Advanced Markus chamber show that:

1. All three Boag's modified expressions ($(k_s)_{th}^{B'}$, $(k_s)_{th}^{B''}$ and $(k_s)_{th}^{B'''}$) are suitable to determine the k_s factor. Due to the dose-per-pulse range investigated in the present work (4-42 mGy per pulse), the average deviation of k_s values resulting from them lay within the measurement uncertainty (an overall uncertainty of 3% should be considered for $(k_s)\prime_{th}/(k_s)_w^{ref}$ values).
2. The ion recombination correction factor assessed from the TRS-398 protocol ($(k_s)_{th}^{TVA}$) also show reliable results up to a dose-per-pulse value of 35 mGy per pulse. The authors advise against the use of this protocol for k_s determination above this value.
3. The difference between k_s values resulted from the four evaluation models ($(k_s)_{th}^{B'}$, $(k_s)_{th}^{B''}$, $(k_s)_{th}^{B'''}$ and $(k_s)_{th}^{TVA}$) tends to reduce as the chamber's operating voltage increases. This result is consistent within the theoretic prediction.
4. The finding with respect to k_s using the Jaffé plot is promising and should be explored in greater detail.

Acknowledgements

The authors thank Burkhardt Bannach for helpful discussions. We would like to thank Holger Gottschlag for his critical reading of the manuscript and his useful advice. For their help in data acquisition, we would also like to thank Zeliha Eroglu and Philipp Martini. The authors are grateful to their colleagues at the Dept. of Radiotherapy for their permanent motivation and support.

References

[1] Beddar AS, Biggs PJ, Chang S, Ezzell GA, Faddegon BA, Hensley FW, Mills MD. Intraoperative radiation therapy using mobile electron linear accelerators: Report of AAPM Radiation Therapy Committee Task Group No. 72. Med Phys 2006;33:1476–89.
[2] Rosi A, Viti V. Guidelines for quality assurance in intra-operative radiation therapy. Oncol 2004;27:442–75.
[3] Ronsivalle C, Picardi L, Vignati A, Tata A, Benassi M. Accelerators development for intraoperative radiation therapy. Part Accel Conf 2001;4:2494–6.
[4] Burns DT, McEwen MR. Ion recombination corrections for the NACP parallel-plate chamber in a pulsed electron beam. Phys Med Biol 1998;43:2033–45.
[5] Andreo P, Kanai T, Laitano F, Smyth V, Zealand N, Vynckier S. Ansorbed Dose Determination in External Beam Radiotherapy. IAEA TRS-398 2000.
[6] Almond PR, Biggs PJ, Coursey BM, Hanson WF, Huq MS, Nath R, et al. AAPM's TG-51 protocol for clinical reference dosimetry of high-energy photon and electron beams. Med Phys 1999;26:1847–70.
[7] McEwen M, DeWerd L, Ibbott G, Followill D, Rogers DWO, Seltzer S, Seuntjens J. Addendum to the AAPM's TG-51 protocol for clinical reference dosimetry of high-energy photon beams. Med Phys 2014;41, 041501-20.
[8] DIN6800-2, Procedures of dosimetry with probe-type detectors for photon and electron radiation-Part2: Ionization chamber dosimetry of high energy photon and electron radiation (2008).
[9] Piermattei a, Canne SD, Azario L, Russo a, Fidanzio a, Micelit R, et al. The saturation loss for plane parallel ionization chambers at high dose per pulse values. Phys Med Biol 2000;45:1869–83.

[10] Laitano RF, Guerra AS, Pimpinella M, Caporali C, Petrucci A. Charge collection efficiency in ionization chambers exposed to electron beams with high dose per pulse. Phys Med Biol 2006;51:6419–36.
[11] Hochhäuser E, Balk OA. The influence of unattached electrons on the collection efficiency of ionisation chambers for the measurement of radiation pulses of high dose rate. Phys Med Biol 1986;31:223–33.
[12] Boag JW, Hochhäuser E, Balk OA. The effect of free-electron collection on the recombination correction to ionization measurements of pulsed radiation. Phys Med Biol 1996;41:885–97.
[13] Di Martino F, Giannelli M, Traino AC, Lazzeri M. Ion recombination correction for very high dose-per-pulse high-energy electron beams. Med Phys 2005;32:2204–10.
[14] Cella L, Liuzzi R, Salvatore M. The Italian affair: the employment of parallel-plate ionization chambers for dose measurements in high dose-per-pulse IORT electron beams. Med Phys 2010;37:2918–24.
[15] Fantini M, Santoni F, Soriani A, Creton G, Benassi M, Begnozzi L. IORT Novac7: A New Linear Accelerator for Electron Beam Therapy. Front Radiat Ther Oncol 1997;31:54–9.
[16] Karsch L, Beyreuther E, Burris-Mog T, Kraft S, Richter C, Zeil K, et al. Dose rate dependence for different dosimeters and detectors: TLD, OSL, EBT films, and diamond detectors. Med Phys 2012;39:2447.
[17] Blad B, Nilsson P, Knöös T. The influence of air humidity on an unsealed ionization chamber in a linear accelerator. Phys Med Biol 1996;41:2541–8.
[18] Krieger H. Radiation Measurement and Dosimetry Springer Fachmedien Wiesbaden; 2013.
[19] Pimpinella M, Mihailescu D, Guerra AS, Laitano RF. Dosimetric characteristics of electron beams produced by a mobile accelerator for IORT. Phys Med Biol 2007;52:6197–214.
[20] Martisíková M, Ackermann B, Jäkel O. Analysis of uncertainties in Gafchromic EBT film dosimetry of photon beams. Phys Med Biol 2008;53:7013–27.
[21] Bruggmoser G, Saum R, Schmachtenberg A, Schmid F, Schüle E. Determination of the recombination correction factor k_S for some specific plane-parallel and cylindrical ionization chambers in pulsed photon and electron beams. Phys Med Biol 2007;52:35–50.